博　士　論　文

Emergency-Aware Path Planning for Non-connected and Connected Autonomous Vehicles

(自律型と協調型自動運転のための緊急事態を考慮した経路計画)



東京大学大学院
情報理工学系研究科
創造情報学専攻

48-217612　林　鵬飛

指導教員　塚田 学　准教授

令和 5 年　12 月

© Copyright by Pengfei Lin 2023.
All rights reserved.

Abstract

Automotive safety is a paramount concern in the ever-evolving world of transportation. With millions of vehicles on the road, ensuring the well-being of drivers, passengers, and pedestrians is a critical priority. Specifically, traffic injuries remain a significant and ongoing threat to human properties, resulting in a substantial number of casualties every year. Therefore, autonomous vehicles, also known as self-driving cars, are revolutionizing transportation by offering the potential to enhance road safety, reduce congestion, and increase mobility, while reshaping the future of urban and personal mobility.

An autonomous vehicle is equipped with advanced sensors and algorithms to navigate and operate without human intervention. However, despite years of research and development, autonomous vehicles continue to face safety challenges, with a series of traffic accidents still occurring during road tests. Three main challenges are summarized behind those tragedies: sensor failure that false detection or malfunctions lead to incorrect perception; software glitches that incorrect decision or planning paralysis leads to a fatal trajectory; communication Issues that fail to communicate with other road users.

Planning paralysis refers to a situation where the autonomous vehicle struggles to make decisions or take action due to complex, ambiguous, or unforeseen scenarios on the road. This can occur when the vehicle's algorithms and sensors are overwhelmed by a multitude of factors, such as traffic emergencies, adverse weather conditions, or unfamiliar environments. Addressing planning paralysis is a significant challenge, as it requires sophisticated decision-making capabilities and robust planning algorithms to ensure safe and efficient navigation in real-world conditions.

In this thesis, I present emergency-aware path planning for autonomous vehicles by incorporating optimization-based planning with two categories: non-connected and connected vehicles. The proposed planning module can stably generate a collision-free path under different traffic emergencies and can adapt to the collaboration intention of surrounding vehicles. This thesis work is composed of three steps that address the planning malfunctions in facing emergencies: (i) construct the risk map from the current traffic by

potential field (PF); (ii) plan a collision-free path based on the collaboration intention of surrounding vehicles; (iii) monitor the PF and prepare for emergency navigation in the control layer based on the model predictive control (MPC).

Besides, a significant problem for PF-based path planning is that there are four inherent limitations to stop the planner from generating a safe path. In specific traffic scenarios, those limitations can be triggered, leading to planning paralysis. Therefore, monitoring and foreseeing the possible appearance of those limitations is necessary for ensuring driving safety. At the same time, if the planning paralysis becomes irreversible, it is imperative to implant an emergency navigation function in the control module. The experiments also show that our proposed path planning performs better in collision avoidance (stable path generation, curvature, safety, etc.) than previous methods.

Acknowledgements

In the past 1095 (P)retty (h)$_{appy}^{ard}$ (D)ays, I have finally completed my thesis. Writing this acknowledgment, I reflect on the journey, expecting overwhelming joy but instead finding a serene calmness. It seems the countless small steps and experiences have subtly molded me, leaving me stronger and more composed than I ever imagined.

Back to three years ago, I was a bit naive yet passionate about research. I composed an email and sent it without hesitation to my current supervisor, Prof. Manabu Tsukada, seeking a position as a Ph.D. candidate. I still vividly recall the mixed feelings of excitement and astonishment when I received his positive response. With a mix of nervousness and anticipation, I had my first interview with Prof. Manabu Tsukada, which marked the beginning of my doctoral journey. At that time, amidst the pandemic, Japan had closed its borders to foreigners, so I spent the first year of my Ph.D. in China. Initially, I was concerned that my research might stall due to a lack of equipment and the inability to run necessary simulations. But when Prof. Manabu Tsukada heard about my situation, he immediately sent me a high-end Alienware laptop and an iPad Pro by post to ensure I could continue making progress in my research. Meanwhile, I faced difficulties securing a scholarship, and Prof. Manabu Tsukada kindly provided me with a monthly stipend even though I was still stranded in China. Such instances of his support are numerous. Deep down in my heart, Prof. Manabu Tsukada is more than a mentor; he's more like a close friend. Without his guidance and unwavering support, the completion of this dissertation would have been unattainable. I am deeply grateful to Prof. Manabu Tsukada, not only for his academic guidance but also for the significant influence and help he has provided in my attitude towards life and interpersonal interactions.

I am sincerely grateful to Prof. Hiroshi Esaki. Participating in the Elab camp each year has profoundly impacted me. There, I not only delved into the research projects of other students but also received research advice from Prof. Hiroshi Esaki and other instructors, while enjoying the scenic views and local cuisine. Additionally, I wish to express my gratitude to Prof. Kei Okada

and Prof. Kazuya Takeda for their valuable advice during the thesis defense, which significantly enhanced the quality of my thesis. Also, I am particularly thankful for the guidance and assistance provided by Prof. Shinpei Kato. As a student researcher at Tier IV Inc., I have the opportunity to engage with cutting-edge autonomous driving solutions in the industry. Four years ago, while pursuing my Master's degree in South Korea, I had the chance to learn about Autoware, the first open-source autonomous driving platform, developed by Prof. Shinpei Kato and his team. I am honored to have received guidance from Prof. Shinpei Kato throughout my doctoral studies. I am also grateful to Prof. Masaki Ito for his mentorship and advice regarding my thesis, particularly for dedicating valuable time before the preliminary defense to know about my research, and for his high commendation, which I sincerely appreciate.

My gratitude extends to Prof. Ehsan Javanmardi for joining our lab and providing substantial support in discussing research ideas. Particularly during the conference in Singapore, Prof. Ehsan Javanmardi shared numerous valuable experiences with me, covering research and various aspects of life. I am equally thankful to later-joined Dr. Muhammad Asad, Prof. Jin Nakazato, and Dr. Naren Bao for their great assistance and support. A special thank goes to all the student members of Tsukada Lab; your companionship made my research journey far less lonely and filled it with laughter and support along the way.

As this thesis approaches completion, I particularly want to express my deepest gratitude to my parents. I thank them for their unconditional love, patience, and support, which have been my stronghold throughout the years. Their encouragement and understanding in my academic journey have given me endless strength. Their trust in me and the freedom they have given me allowed exploration of my interests and passions, shaping the person I am today. This achievement is the best tribute to their selfless dedication and sacrifices. I am eternally grateful for their belief in me and their companionship, which I will always treasure.

Dec 2023

Contents

Abstract **ii**

Acknowledgements **v**

List of Figures **xv**

List of Tables **xvi**

1 Introduction and Challenges **1**
1.1 Self-driving cars 1
1.2 Autonomous driving system architecture 4
1.3 Path-planning algorithms 5
1.4 Artificial potential field 7
1.5 Thesis organization 10

2 Research background and contributions **11**
2.1 Potential field in self-driving cars 11
2.1.1 Research Development 11
2.1.2 Main branches 12
2.2 Potential functions for collision avoidance 13
2.2.1 Road potential function 13
2.2.2 Obstacle potential function 16
2.2.3 Attractive potential function 22
2.2.4 Universal potential field 23
2.3 Motivation 24
2.3.1 Motivation of potential field-based path planning . . . 24
2.3.2 Motivation of hazardous scenario-based simulation . . . 25
2.4 Current challenges 26
2.5 Main contributions 27

3 Potential Field-based Path Planning for Emergency Avoidance 29
3.1 Introduction . . . 29
3.2 Overview . . . 31
3.3 Planning in non-connected vehicles . . . 33
3.3.1 Time-to-collision-aware lane change . . . 33
3.3.2 Occlusion-aware collision avoidance . . . 42
3.3.3 Clothoid Curve-based emergency stopping . . . 52
3.4 Planning in connected vehicles . . . 69
3.4.1 Risk assessment index . . . 69
3.4.2 Event-based hybrid planning . . . 74
3.4.3 Interactive speed optimization . . . 82
3.5 Summary . . . 87

4 Safety Tunnel-based Model Predictive Controller for Emergency Navigation 89
4.1 Introduction . . . 89
4.2 Overview . . . 91
4.3 Vehicle motion modeling . . . 91
4.4 Model predictive controller . . . 93
4.4.1 Future prediction of model outputs . . . 93
4.4.2 Constraints design . . . 95
4.4.3 Objective function design . . . 95
4.5 Emergency triggering estimation . . . 96
4.6 Safety tunnel for emergency navigation . . . 101
4.7 Simulation and results . . . 103
4.7.1 Settings . . . 104
4.7.2 Emergency scenarios . . . 105
4.7.3 Results and analysis . . . 105
4.8 Summary . . . 110

5 Conclusions 111
5.1 Summary and discussion . . . 111
5.2 Limitation . . . 112
5.3 Ethical issues . . . 114
5.4 Future perspective . . . 115

Bibliography 118

Publications 133

List of Figures

1.1 Autonomous driving system framework [Mil22]. 4
1.2 Mobile robot in an electric field. 8
1.3 Four inherent limitations when using the APF for path planning. 9

2.1 Driving safety field [WWL15] and Universal potential field [JKMH17] 13
2.2 Potential field of the road [WB08]. 14
2.3 Potential field of the curve road. 15
2.4 Triangular potential field of obstacle vehicle [WB08]. 17
2.5 Noncrossable and crossable obstacle potential fields. 18
2.6 Ellipse-like potential field for path planning. 19

3.1 Non-connected autonomous vehicles with sensing, decision-making, and control capabilities [Dav15]. 30
3.2 Connected autonomous vehicles combining connectivity and automated technologies to assist or replace humans in the task of driving [Edm22]. 31
3.3 Overview of potential field-based path planning for emergency avoidance. 32
3.4 Proposed TTCA-LC strategy: Curve fitting computes the optimized cubic polynomial by considering the waypoints and yaw angle from the planning module as well as the TTC from the sensing module. 33
3.5 3D view of road potential field. 34
3.6 Conventional potential field-based lane-change strategy for different driving cases on the highway. 37
3.7 Waypoint tracking methods [JKLC15]: (a) point-wise, (b) curve-fitting. 38
3.8 Two vehicles driving in the same direction: red vehicle (rear) drives at (v_1, a_1); orange vehicle (front) drives at (v_2, a_2). . . 39

3.9 Proposed time-to-collision-aware lane-change strategy with the potential field: using the TTC for constraint design that allows the ego vehicle to complete the LC in advance, reserving sufficient space for deceleration if the obstacle suddenly steers. 39
3.10 Trajectories of the conventional and optimized potential field planners under speeds of 108 km/h. 40
3.11 Motion states of the vehicle. 41
3.12 Curvature of the trajectories 42
3.13 Proposed PF-OAPP framework consists of sensing & perception, planning, control and actuators: Planning layer has the PF that can differentiate the visible and occluded obstacles, and then conduct the RSS violation check to adjust the virtual forces and generate the speed reference 44
3.14 Occlusion problem: the brown vehicle is occluded by the orange vehicle from the view of the green vehicle, which the brown vehicle does not have a PF; the next moment movements of the autonomous vehicles indicate the invisible driving maneuvers of the brown vehicle can impact the green vehicle's local path 46
3.15 Synthesis and decomposition of virtual forces when seeing the occluded obstacle 2 from two approaches 47
3.16 Trajectories of the CPF-based and OPF-based planners under the speed of 108 km/h 50
3.17 Motion states of the obstacle vehicle based on PF-CS, PF-SP, and PF-OAPP, respectively 50
3.18 Virtual forces from PF-CS, PF-SP, and PF-OAPP, respectively 51
3.19 Analysis of α_1, α_2 and Occlusion flag in PF-OAPP. 52
3.20 Overall autonomous driving system framework with the embedded ESPP method: Sensing data gathers the information collected by sensors; Planning layer monitors the emergency and triggers the ESPP computation if the emergency is sensed; Control system outputs the direct signals to Vehicle Actuators for longitudinal and lateral maneuvers 53
3.21 Emergency merging behavior of the adjacent vehicle (black) owing to the unexpected animal (brown): From the oblique view, the obstacle PF intersects with lower road PF, leading to a blind alley (local minima) 55

3.22 Explanation of the emergency triggering estimation: With ψ_{ref} given by APF, making an extension line from the current position of ego-vehicle (green) to intersect with the lower road boundary P_{int}; D_{E2R} is the distance between the green vehicle and P_{int} 56
3.23 System flow chart of the proposed emergency triggering estimation 56
3.24 Emergency-Stopping Path Planning on the expressway: Regionalization within the brown dashed box (S_1, S_2, S_3, S_4); three star-shape points are then obtained (red, blue, purple); interpolation points (circle) are used for computing the clothoid curve (light blue). 57
3.25 Detailed system architecture of the proposed ESPP method . 63
3.26 Vehicle trajectories of different path planners: the gray area represents the typical freeway, and the orange area denotes the emergency stopping lane or open space. 66
3.27 3D potential field modeling of the ESPP: Opening a breach for the ego-vehicle to avoid collision 67
3.28 Front wheel steering angles of the ego vehicle. 67
3.29 Heading angles of the ego vehicle. 67
3.30 (Linear) Longitudinal speeds of four wheels of APF without LR: L1 is the left front wheel; R1 is the right front wheel; L2 is the left rear wheel; R2 is the right rear wheel 68
3.31 (Linear) Longitudinal speeds of four wheels of ESPP-based APF: L1 is the left front wheel; R1 is the right front wheel; L2 is the left rear wheel; R2 is the right rear wheel 68
3.32 Lateral accelerations of the ego vehicle. 68
3.33 Longitudinal and lateral coordinates of the stop point (SP). . 68
3.34 Rolling resist moment of four tires from the APF without LR-based planner: L1 is the left front tire; R1 is the right front tire; L2 is the left rear tire; R2 is the right rear tire 69
3.35 Rolling resist moment of four tires from the ESPP-based planner: L1 is the left front tire; R1 is the right front tire; L2 is the left rear tire; R2 is the right rear tire 69
3.36 Roll rate of four wheels from the APF without LR-based planner 69
3.37 Roll rate of four wheels from the ESPP-based planner 69
3.38 Computational time of the planners. 70
3.39 Differences between the typical PF-MPC framework and proposed APF-MPC framework (zoom in to see the details). . . . 71
3.40 Trajectories of the obstacle vehicle, PF-MPC, and APF-MPC 72

3.41 Longitudinal motion states, RAI, tracking error, and computation time of the comparative simulation results 73
3.42 RSS-based potential field and sigmoid curve. 75
3.43 The slope at the centrosymmetric point of the sigmoid curve. . 76
3.44 Scene description of a required proper deceleration in overtaking multi-obstacles. 76
3.45 Cooperative planning for the adjacent dynamic vehicle if it is willing to cooperate. 77
3.46 Vehicle trajectories in static scenario. 78
3.47 Yaw and front tire steering angles of the ego-vehicle in the static scenario. 79
3.48 Longitudinal speed and computation time in the static scenario. 79
3.49 Vehicle trajectories of HPP and PF-only. 80
3.50 Vehicle trajectories of proposed CHPP. 81
3.51 Desired coordinated speed and yaw angles in the dynamic scenario. 81
3.52 Front tire steering angles and computation time in the dynamic scenario. 82
3.53 Overall system framework (Sensing & Perception, Communication, Planning, Control, and Actuators): Planning layer extracts the shared local path from V2V communication and then formulates a constrained objective function with proper analysis 83
3.54 Merging scenario where the obstacle (blue) vehicle and the ego (green) vehicle apply the PF independently (Colormap: Hot for the blue vehicle and Colormap: Jet for the green vehicle). The paths depicted on the colormap are generated by the PF-only planner, while the paths denoted in the middle part are produced by the PF-ISO planner; the distance between the waypoints varies with speed 85
3.55 Paths of the obstacle and ego vehicles based on PF-CS, PF-SP, and PF-ISO, respectively 86
3.56 Motion states of the obstacle vehicle based on PF-CS, PF-SP, and PF-ISO, respectively 87

4.1 Overview of the safety tunnel-based model predictive controller 90
4.2 Vehicle lateral dynamics model [STJP06, FZM15] 92
4.3 3D figure of the road's potential field in an emergency situation. Dynamic vehicle (bright green) decelerates suddenly (denoted as the red arrow) due to the unexpected falling stone when the ego-vehicle (blue) is in lane-changing phase 97

4.4 Triggering analysis of the potential fields of the obstacle vehicles to determine whether a narrow passage is produced 98
4.5 Overall framework of model predictive path-planning system with the emergency triggering estimation. 100
4.6 ST design based on emergencies: (a) The longitudinal position of CST is determined by D_h and ρ; (b) The longitudinal position of CST is determined by the obstacles' positions and relative speeds 102
4.7 Co-simulation framework: Path planning and tracking algorithms are conducted in MATLAB/Simulink; Control signals are evaluated in CarSim Simulator 104
4.8 Comparative study of vehicle trajectories: front dynamic obstacle decelerates during the lane-change phase (blue dotted line) due to the falling stones (cyan triangle); PF-STMPC trajectory (solid green line) under safety tunnel boundaries (dotted magenta line) is smoother than that of PF-CMPC (dotted-solid red line) 106
4.9 Variations in the front obstacle's potential field (3D to 2D projection X-Y plane) when the obstacle vehicle decelerates: From 10.00 s to 11.95 s, the PF expands rapidly around 255 m; the higher potential power means the higher collision risk . 106
4.10 Motion states of the vehicle: black dotted line means the empirical bound of the sideslip angle; magenta dotted line denoted the imposed hard constraints 107
4.11 Comparative study of vehicle trajectories: static obstacle (black rectangle) parks at (175,2); dynamic obstacle (blue rectangle) decelerates (dotted blue line) due to the falling stone (cyan triangle); PF-STMPC trajectory (solid green line) safely goes through the closely spaced obstacles while PF-CMPC (dotted-solid red line) fails 107
4.12 Potential power analysis and vehicle trajectories: the potential field was built on T=8 s; from 175 m to 220 m, there has a severe overlapping part in the two obstacles' potential fields that PF-CMPC moves toward the road boundary while PF-STMPC safely avoids the obstacles and stays within the road . 108
4.13 Motion states of the vehicle: black dotted line means the empirical bound of the sideslip angle; magenta dotted line denoted the imposed hard constraints 108

4.14 Comparative study of vehicle trajectories: dynamic obstacle 1 drives constantly at 12 [m/s] (dotted blue line); dynamic obstacle 2 moves at 15 [m/s] and suddenly changes its lane (dotted purple-brown line) due to the falling stone (cyan triangle); PF-CMPC trajectory (dotted-solid red line) collides with dynamic obstacle 2; PF-STMPC trajectory safely avoids the two obstacles under safety tunnel constraints (dotted magenta line) 109
4.15 Motion states of the vehicle: black dotted line means the empirical bound of the sideslip angle; magenta dotted line denoted the imposed hard constraints 110

List of Tables

3.1 Parameters of ESPP-based PF 64
3.2 Performance Evaluations 65

4.1 Parameters of the MPC controller 104

Chapter 1

Introduction and Challenges

1.1 Self-driving cars

Every year, approximately 1.3 million lives are tragically lost in traffic crashes, and another 20 to 50 million individuals endure non-fatal injuries, many of whom grapple with lasting disabilities and/or enduring mental health challenges [Org22, CHM21]. In particular, Japan has witnessed a concerning increase in traffic accidents, with a total of 300,840 reported cases in the past year, tragically resulting in over 2,600 fatalities [Sta22]. Alarmingly, a significant portion of these accidents, accounting for approximately 61%, can be attributed to the neglect or failure of drivers to fulfill their essential responsibilities and obligations. This worrisome trend underscores the pressing need for enhanced road safety measures, awareness campaigns, and, potentially, advanced vehicle technologies to mitigate the human factors contributing to accidents and save lives on Japan's roadways. As a response to this alarming global crisis, a new generation of Intelligent Transportation Systems (ITS) has emerged with the primary mission of significantly reducing casualties over the next decade. These self-driving cars, also called autonomous vehicles, are proposed with a multitude of sensors, such as lidar and cameras, enabling them to autonomously navigate and execute critical functions, ensuring safe arrival at their destinations without human intervention. However, shortly after the advent of autonomous vehicles, manufacturers initiated road tests, leading to an unfortunate series of traffic accidents and tragedies. According to the Department of Motor Vehicles (DMV) in California [oMV21], there have been approximately 640 traffic collision events involving autonomous vehicles. These incidents underscore the critical need for continuous research and development in AV technology and safety measures to realize the full potential of this transformative mode of transportation while mitigating risks.

Self-driving cars are categorized into different levels based on their degree of automation and the extent of human intervention required. These levels are defined by the Society of Automotive Engineers (SAE) in their J3016 standard [Int18]. So far, there are six levels of automation for autonomous vehicles:

Level 0 - No Automation At this level, there is no automation in the vehicle. The human driver is responsible for all aspects of driving, and there may be some basic warning systems, such as collision warnings or lane departure alerts.

Level 1 - Driver Assistance Level 1 vehicles provide limited driver assistance, typically in the form of either steering or acceleration/deceleration assistance. However, the driver must remain engaged and in control of the vehicle at all times.

Level 2 - Partial Automation At this level, the vehicle can control both steering and acceleration/deceleration simultaneously. However, the driver must remain attentive and be ready to take over if needed. Features like adaptive cruise control and lane-keeping assistance are examples of Level 2 automation.

Level 3 - Conditional Automation Level 3 vehicles are capable of autonomous driving in specific conditions, such as highway driving, but still require human intervention when the system encounters situations it can't handle. The driver can disengage from driving tasks but must be prepared to take control when alerted by the vehicle.

Level 4 - High Automation Level 4 vehicles are capable of fully autonomous driving in most situations without human intervention. However, they may still require a human driver to take over in certain scenarios, such as severe weather conditions or specific geofenced areas.

Level 5 - Full Automation Level 5 vehicles are fully autonomous and do not require a human driver at any time. These vehicles can operate in all conditions and environments where a human-driven vehicle can operate.

It's essential to note that the development of autonomous vehicle technology is ongoing, and regulations and standards may continue to evolve. Furthermore, the practical deployment of Level 5 autonomous vehicles may require time and entail various technical and regulatory challenges. Several

world's top companies were actively involved in the development and research of Level 4 and Level 5 autonomous vehicles. Here are a few notable ones: **Waymo**, **Tesla**, **Tier IV**, **Cruise Automation**, **Uber ATG**, **Mobileye**, **NVIDIA**, etc. However, a series of traffic accidents caused by autonomous vehicles has also raised public doubts about driving safety. A few notable incidents related to autonomous vehicle collisions in road tests that occurred prior to that date: Uber's Fatal Accident in 2018, Tesla Autopilot Crashes in 2020, Cruise Automation's Collision in 2023, etc. Some of the main factors contributing to these incidents include:

Sensor failure refers to the malfunction or inaccurate performance of the sensors critical for perceiving the vehicle's environment. These failures can result from various factors like adverse weather, damage, interference, or software errors, and they can impact the vehicle's safety.

Software glitches refer to unexpected errors, bugs, or malfunctions in the computer programs and algorithms that control and coordinate various aspects of the vehicle's autonomous operation. These glitches can lead to incorrect sensor data interpretation, decision-making errors, planning paralysis, or system instability.

Communication issues refer to problems with data exchange and information flow between different components and with external systems. These issues can affect vehicle-to-vehicle (V2V) and vehicle-to-infrastructure (V2I) communication, as well as communication within the vehicle's own systems. They can impact the vehicle's ability to receive critical information, such as traffic updates or data from other vehicles.

Urgent traffic conditions refer to critical situations on the road that require immediate and precise responses. These conditions can include sudden lane changes, emergency braking, avoiding obstacles, and responding to unexpected road events. This involves real-time sensor data analysis, decision-making and planning algorithms, and the ability to execute evasive maneuvers to prevent accidents or collisions.

Therefore, effectively addressing these factors is the primary technical challenge for the entire autonomous driving industry to achieve commercial viability.

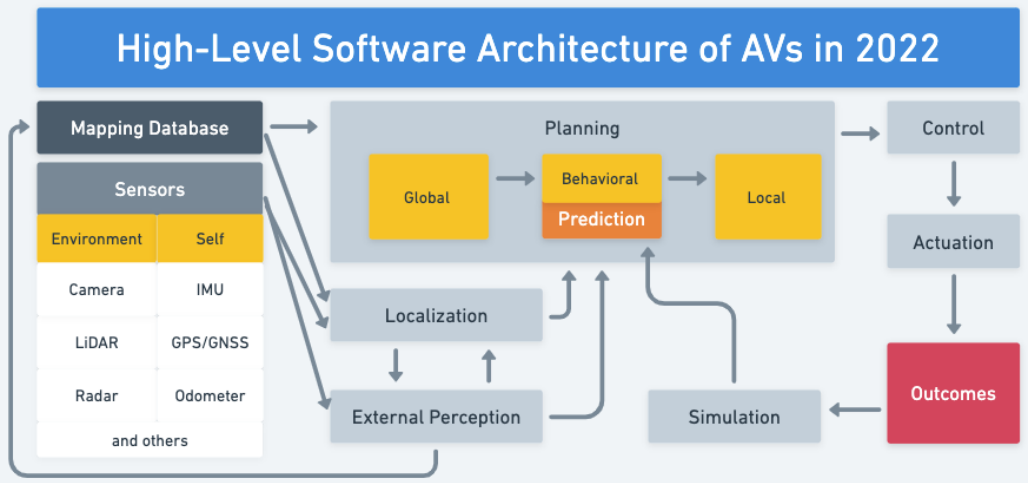


Figure 1.1: Autonomous driving system framework [Mil22].

1.2 Autonomous driving system architecture

This section will have an overview of the autonomous driving system. As shown in Fig. 1.1, here are the following modules to compose this vase and complex system:

Mapping Database is a critical component that provides high-definition, geospatial information about the road network. It includes detailed maps of lane boundaries, road signs, traffic signals, and other static infrastructure elements. The mapping database can be updated in real-time to reflect changes in road conditions, ensuring the vehicle always has the most accurate information available.

Sensors are a set of devices that capture data about the vehicle's surroundings. These sensors include camera, LiDAR, radar, ultrasonic sensors for the environment, and inertial measurement unit (IMU), global positioning system (GPS), odometer for self-states. They play a crucial role in perceiving the environment by collecting information about other vehicles, pedestrians, road conditions, and traffic signals.

Perception refers to the system's ability to interpret and understand the vehicle's surroundings. This is achieved through the analysis of data collected by sensors. Perception algorithms process this sensor data to identify objects,

detect obstacles, interpret road signs and traffic signals, and determine the vehicle's position within its environment.

Localization refers to the system's capability to precisely determine the vehicle's position within its environment. It typically involves the use of GPS data and high-definition maps. This information is essential for safe and accurate navigation, as it allows the vehicle to understand its position on the road and plan its path accordingly.

Planning is the process of generating a path or route for the vehicle to follow. This involves making driving decisions, such as steering, accelerating, braking, and changing lanes while considering factors like safety, traffic rules, and road conditions. The planning module is generally subdivided into the following sub-modules:

- **Global (route) planning** finds the global route with a given starting point and target point combined with map information.
- **Behavioral planning** plans the set of high-level driving decisions or actions to safely achieve the driving mission under various driving situations.
- **Local (path) planning** finds the local optimal trajectory (path and velocity) to follow a global reference trajectory while avoiding obstacles.

Control involves executing the driving actions necessary to follow the planned path and ensure safe and efficient navigation. This includes steering, accelerating, braking, and adjusting the vehicle's movements in real time based on sensor data and planning algorithms.

Actuation refers to the physical mechanisms that carry out control commands generated by the vehicle's control system. This includes components like the steering system, throttle, and brakes.

These components work in harmony to enable autonomous vehicles to navigate, make driving decisions, and operate safely on the road.

1.3 Path-planning algorithms

In this section, we introduce some primary path-planning algorithms that are broadly used in autonomous driving.

Graph search-based path planning finds an optimal path from a starting point to a target point. It's based on treating the environment as a graph, where nodes represent specific positions or states, and edges represent possible movements or transitions between these positions. The most representative algorithms are as follows: Dijkstra algorithm [Dij72, WYY11], A* algorithm family [HNR68, DBK+14, DTMD08], state lattice [MUDL11, ZS09].

Graph Search-based path planning offers several advantages for the autonomous vehicle. It can find optimal routes, adapt to dynamic changes, and work well in structured environments like roads and intersections. These methods are customizable, operate in real-time, and exhibit predictable behavior, making them valuable for safe and efficient navigation. However, their performance relies on map quality, search algorithm efficiency, and the environment's complexity. In less structured or highly dynamic settings, alternative path-planning methods may be more suitable.

Sampling-based path planning is a fundamental approach used in autonomous vehicles, particularly in complex and unstructured environments. Instead of mapping the entire space, it randomly samples points and builds a probabilistic roadmap or tree connecting them. Popular algorithms like Rapidly-Exploring Random Trees (RRT) [LKDO01] and its variants (RRT* [KWP+11], goal-bias RRT [US03], etc.) and Probabilistic Roadmaps (PRM) [KSLO96, KKL98] fall under this category.

Sampling-based methods are advantageous for their adaptability to diverse environments, handling dynamic changes, and efficient exploration of unknown terrains. However, the resulting path is not continuous and therefore jerky and the optimality of the path strongly depends of the time frame for the RRT* case.

Learning-based path planning leverages machine learning techniques to generate paths and make driving decisions. It uses neural networks and other algorithms, such as deep reinforcement learning (DRL) [Ara22], imitation learning (IL) [Ara22, PCS+20] to learn from data, such as sensor observations, maps, and real-world driving experiences, to plan routes and navigate in complex and dynamic environments.

Learning-based methods can adapt to a wide range of scenarios, making them valuable for real-world applications. However, the complex training is computationally intensive and time-consuming, which, coupled with a reliance on diverse and high-quality data, can lead to robustness concerns in safety-critical applications due to the lack of transparency for interpretability.

Numerical optimization-based path planning formulates the path planning problem as an optimization task. It involves defining an objective function and constraints to find the optimal path. By optimizing parameters or decision variables, this method aims to minimize or maximize a specific criterion, such as travel time, energy consumption, or safety. The representative algorithm is the artificial potential field (APF) [Kha85, VTML00, PJL01].

Numerical optimization-based approaches can handle complex, dynamic environments and adapt to various real-world constraints. However, it can become complex, computationally expensive, sensitive to initial conditions, and may require trade-offs and fine-tuning, potentially leading to sub-optimal solutions in dynamic environments.

In conclusion, path-planning algorithms in autonomous driving have made significant advancements, incorporating a variety of approaches. These algorithms are increasingly capable of handling complex and dynamic environments, making use of advanced sensors and high-definition maps. They continue to evolve with a focus on optimizing safety, efficiency, and adaptability to various scenarios. However, challenges remain in ensuring real-time performance, addressing limitations, and achieving regulatory approval for widespread deployment, particularly at higher automation levels. In this thesis, we will delve deeper into the planning algorithm based on numerical optimization: the APF. Our goal is to enhance the path planning system centered on APF, which is introduced in the next section.

1.4 Artificial potential field

The APF method was first presented by Oussama Khatib [Kha85] in 1986 for real-time avoidance in manipulators and mobile robots, inspired by classical mechanics. This method models the environment as a field with attractive and repulsive forces. For example, in an electric field as shown in Fig. 1.2, we place the negative component at the target point and the positive component at the robot's position. Consequently, the robot will move towards the target point. If the robot encounters two obstacles during its movement, we can also introduce positive components around the obstacles. This allows the obstacles to exert repulsive forces on the robot, pushing it away. Therefore, APF can simulate the process of high potential moving toward low potential while repelling similar charges. In doing so, the robot can reach the target point without colliding with obstacles. Hence, we can introduce the two most important concepts in APF:

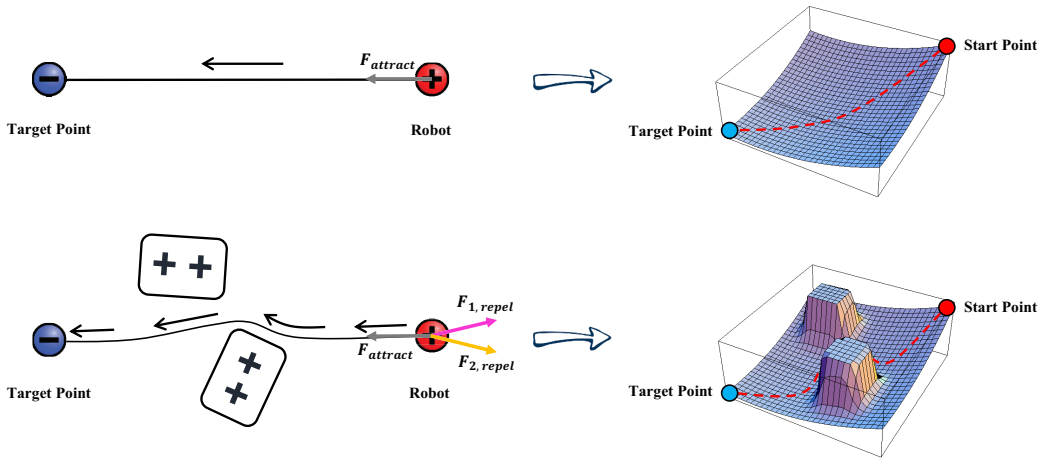


Figure 1.2: Mobile robot in an electric field.

Attractive function generates a force that pulls the robot or vehicle toward the desired goal or target point. The strength of this attractive force is typically inversely proportional to the distance between the robot's current position and the goal. As the robot gets closer to the goal, the attractive force diminishes. The following function is designed for the attraction U_{att}:

$$U_{att}(\mathrm{x}) = \frac{1}{2} k_a |\mathrm{x} - \mathrm{x_d}|^2 \tag{1.1}$$

where k_a represents a constant, x denotes the position vector of the robot, and $\mathrm{x_d}$ signifies the position vector of the goal or target position.

Repulsive function is a crucial component that helps a robot or autonomous vehicle navigate through its environment while avoiding obstacles. The repulsive function calculates the repulsive forces exerted on the robot by obstacles, and its purpose is to push the robot away from these obstacles to prevent collisions. The following piece-wise function is frequently used for calculating U_{rep}:

$$U_{rep} = \begin{cases} \frac{1}{2} k_r (\frac{1}{\rho} - \frac{1}{\rho_0})^2, & \text{if } \rho \leq \rho_0 \\ 0, & \text{if } \rho > \rho_0 \end{cases} \tag{1.2}$$

where k_r is also a constant, ρ_0 defines the maximum distance over which the PF exerts its influence and ρ represents the closest distance to the obstacle. Note that the choice of the distance ρ_0 will be contingent on the robot's speed and its deceleration capabilities.

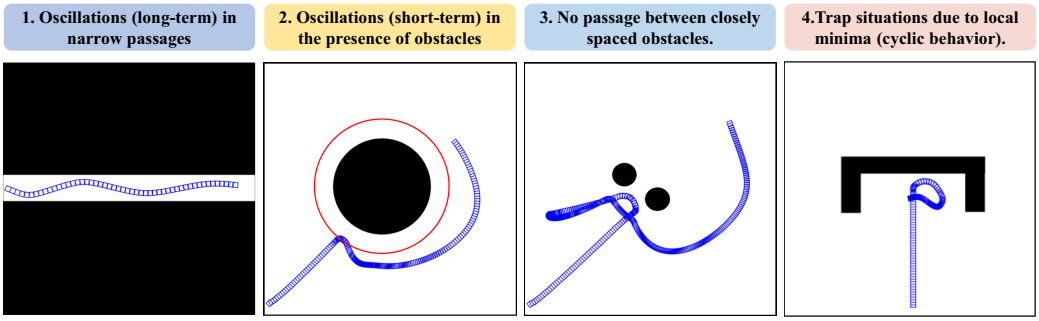


Figure 1.3: Four inherent limitations when using the APF for path planning.

However, despite its outstanding performance in real-time avoidance and simple structure, Yoram Koren [KB91] has identified four inherent limitations when using the APF for path-planning tasks, as drawn in Fig. 1.3.

Long-term oscillation refers to the repetitive back-and-forth movements of a robot when navigating through a constrained or narrow space, such as a corridor or a tight passage between obstacles. It is because the robot experiences repulsive forces simultaneously from opposite sides.

Short-term oscillation refers to the temporarily unstable motion when the robot enters the obstacle's field. It is because the total force violates the stable condition when the robot receives the repulsive force from the obstacle.

No passage between closely spaced obstacles occurs when the robot is surrounded by closely spaced obstacles, and the repulsive forces generated by these obstacles become dominant. The repulsive forces push the robot away from each obstacle, creating a region of high repulsion in the space between them.

Trap situations due to local minima (cyclic behavior) refers to scenarios where a robot becomes stuck in a cyclic or repetitive movement pattern within an obstacle-laden environment. It is usually because the forces generated by the APF are balanced or cyclic.

Therefore, when using the APF to plan the desired path, it is essential to be attentive to the potential occurrence of the above-mentioned issues in order to prevent serious consequences.

1.5 Thesis organization

The structure of this thesis is organized as follows:

Chapter 1 provides an introduction to the background of our research, encompassing the evolution and challenges of self-driving cars, the architecture of autonomous driving systems, primary path-planning algorithms, and the theory and inherent limitations of the APF.

Chapter 2 reviews the related works on PF-based path-planning methods for self-driving cars, summarizing their current relative merits. We are motivated to address the existing limitations of various PF approaches. Additionally, the chapter outlines the specific challenges we encounter when applying planning algorithms in traffic emergencies and then summarizes the primary contributions of this thesis.

Chapter 3 introduces our proposed adaptive PF for path-planning tasks in emergency avoidance. We integrate the PF with time to collision, clothoid curve, responsibility-sensitive safety, and sigmoid curve to address challenging scenarios. Furthermore, the proposed method can adaptively adjust the path generation for non-connected and connected autonomous vehicles.

Chapter 4 introduces foundational knowledge about model predictive control (MPC), encompassing vehicle models, constraints, and the design of the objective function. Additionally, we present an emergency-triggering estimation to anticipate PF malfunctions and then design safety tunnel-based emergency navigation within the control layer in case the planning layer fails to plan a collision-free path.

Chapter 5 concludes the thesis, including the challenges we solved, the main contributions we have, and the key findings of the experimental results.

Chapter 6 discusses the remaining challenges of the proposed method and its substantial impact on future research and applications.

Chapter 2

Research background and contributions

In this chapter, we conduct a thorough analysis of the prevailing challenges pertaining to our research objective and subsequently outline the primary contributions of this thesis.

2.1 Potential field in self-driving cars

This section introduces the research development of the PF method in self-driving cars and its main branches after years of development.

2.1.1 Research Development

While the application of APFs in the field of robotics has matured, its application in autonomous driving still requires significant improvements. This can be attributed to inherent differences between mobile robots and autonomous vehicles, such as variations in their application domains, sizes, structures, etc. Therefore, in the field of autonomous driving, the following aspects must be emphasized and considered:

Vehicle kinematics is a branch of mechanics that focuses on describing the motion of vehicles without considering the forces that cause this motion. It deals with the relationships between a vehicle's position, velocity, and acceleration as it moves through space.

Vehicle dynamics considers the forces and torques that affect a vehicle's motion. It includes factors like tire-road interaction, suspension characteris-

tics, and the effects of steering and braking. Dynamics is crucial for understanding how a vehicle responds to control inputs and external influences, allowing for accurate control and stability in various driving conditions.

Traffic regulations and rules are a set of legal guidelines and requirements that govern the behavior of drivers, pedestrians, cyclists, and other road users on public roadways. These rules are established to promote road safety, efficient traffic flow, and orderly transportation.

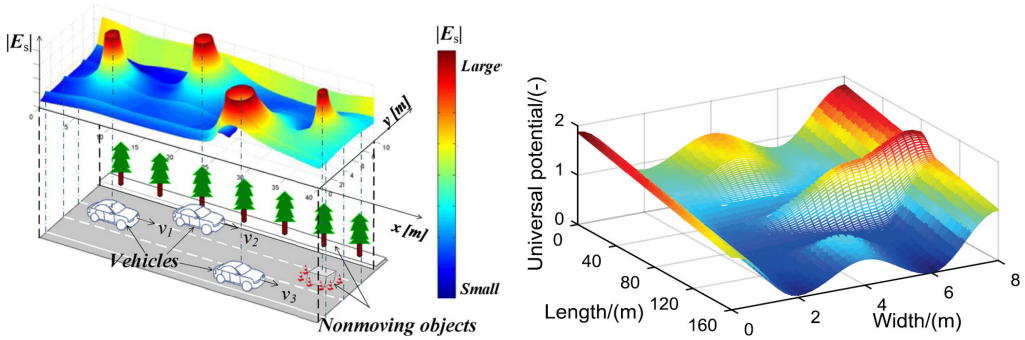
Safety concerns in autonomous vehicles should take top priority. While mobile robots are often used for transporting items, autonomous driving primarily involves people as passengers. Therefore, safety is of utmost importance in autonomous driving.

Riding comfort refers to the quality of the experience for passengers or drivers while traveling in a vehicle. It encompasses various factors that contribute to a smooth, pleasant, and comfortable ride. It is particularly important in autonomous vehicles, where passengers may be more focused on other activities and less engaged in driving.

2.1.2 Main branches

After years of research and development, the PF has evolved into two main branches. The first is used for risk assessment proposed by Wang et al. [WWLL14, WWL15], also referred to as the "driving safety field". Building upon the foundation of traditional PFs, two additional PF models have emerged: the kinetic field and the behavior field. As illustrated in Fig. 2.1(a) below, traditional PFs are employed to analyze static obstacles and road structures. The kinetic field is governed by moving components on the roads, including vehicles and pedestrians. Furthermore, the behavior field is shaped by the unique attributes of individual drivers. Additionally, the text outlines potential applications for this model and demonstrates its utilization in a typical car-following scenario to assess the risks arising from multiple traffic factors. The driving safety field serves as a tool to unveil interactions among drivers, vehicles, and road conditions, shedding light on their impacts on driving safety and predicting safety trends in response to dynamic changes. This branch does not directly generate paths but influences path generation by providing risk analysis.

The second branch uses the PF for direct path generation. In contrast, this branch does not include a behavior field but introduces various types of



(a) Risk assessment (b) Path planning

Figure 2.1: Driving safety field [WWL15] and Universal potential field [JKMH17]

potential functions to model different shapes of fields for obstacle vehicles. Furthermore, this branch retains the attractive PF from traditional PFs to guide autonomous vehicles forward. Therefore, there are three important components that are almost similar to the APF used in robotics, including the road PF, obstacle PF, and attractive PF. After that, we can get a universal PF for the current traffic situation, as shown in Fig. 2.1(b) from Ji et al. [JKMH17]'s work. Finally, we can use gradient descent to derive a local path on the current universal PF.

2.2 Potential functions for collision avoidance

In this section, we will introduce the potential functions used for modeling the corresponding PF in detail, focusing on their application in collision avoidance. Concomitantly, We will also review related works on path-planning methods based on various PFs in autonomous driving.

2.2.1 Road potential function

The road structure usually consists of road boundaries, lane dividers, and lanes. Road boundaries are the outer edges or limits of the roadway. They define the area within which vehicles must stay while traveling on the road. Road boundaries are typically marked by features such as curbs, sidewalks, guardrails, and road shoulders. They help separate the road from adjacent properties, pedestrian areas, or other roads. These boundaries are essential for maintaining order and safety on the road. Therefore, Wolf et al. [WB08]

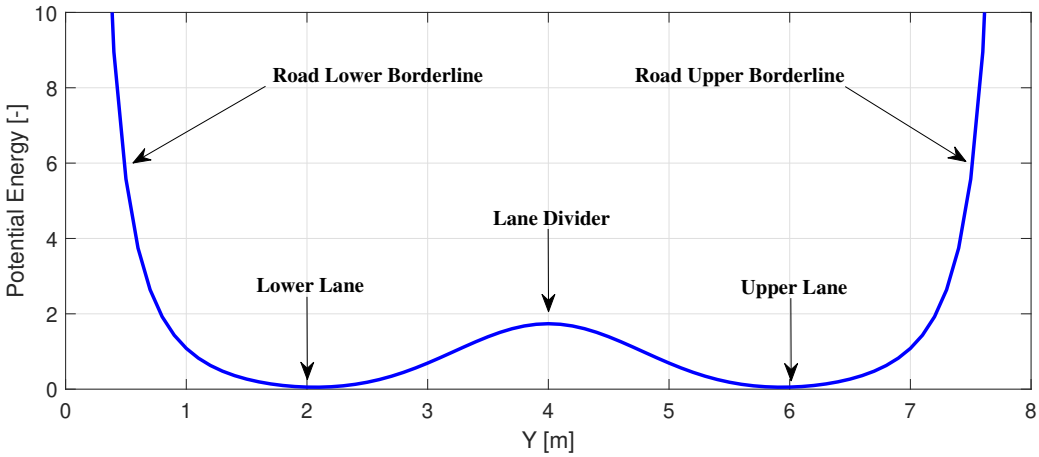


Figure 2.2: Potential field of the road [WB08].

presented the following potential function that is used for modeling the PF of road boundaries:

$$U_{road,j} = \frac{1}{2}\eta \left(\frac{1}{y - y_{0,j}} \right)^2 \tag{2.1}$$

where η is a scaling factor, and $y_{0,j}$ represents the coordinate of the j^{th} road edge, where $j \in 1, 2$. On the other hand, the role of a lane divider, typically in the form of lane markings or lane stripes on the road, is to provide a visual separation between different lanes on a multi-lane road. Therefore, the potential function $U_{lane,i}$ of lane dividers should exert a certain degree of repulsion on vehicles to keep them driving in the center of the lane. However, it also needs to be small enough to allow vehicles to change lanes relatively easily, as designed below:

$$U_{lane,i} = A_{lane} \exp\left(-\frac{(y - y_{c,i})^2}{2\sigma^2} \right) \tag{2.2}$$

where A_{lane} defines the maximum amplitude of the lane divider potential, $y_{c,i}$ represents the y-position of the i^{th} lane division and σ controls the rate at which the potential increases or decreases, proportional to the lane width. Combining Eqs. (2.1) and (2.2), we can get the PF for straight roads, as depicted in Fig. 2.2. However, the above PF only works for straight roads in Cartesian coordinates [KS80]. Hence, Snapper et al. [Sna18] introduced an improved road PF for curve roads that consider the curvature and lane

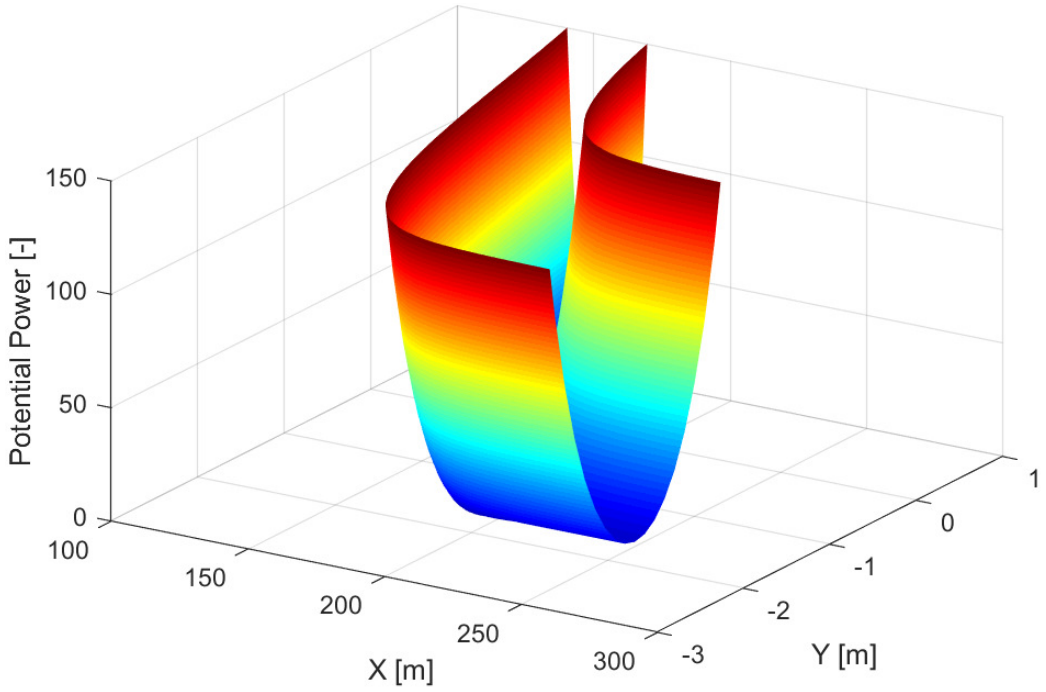


Figure 2.3: Potential field of the curve road.

centerline into the potential function $U_{rl/ll,cr}$ as the following equation:

$$U_{rl/ll,cr} = A_r \left(1 - e^{-b_w sign(Y - Y_{rlc/llc,cr}) \sqrt{\left(\frac{Y-b_y}{m_y} - X\right)^2 + (Y_{rlc/llc,cr} - Y)^2}} \right)^2 \tag{2.3}$$

where A_r is the maximum amplitude of the curved road potential, m_y represents the slope of the line perpendicular to the lane center, which is equal to the y-axis of the future local road frame, while b_y denotes the y-intercept of the line perpendicular to the lane center, $(X,\ Y)$ is the position pair of the ego vehicle in vehicle coordinate, b_w denotes the parameter controlling the width of the curved road potential, $Y_{rlc/llc,cr}$ are the right and left center lines of the curve road. The PF modeling of a curve road is shown in Fig. 2.3.

In conclusion, the road potential function constructs the PF based on the role of each road component, assigning impassable potential energy values to road boundaries/edges while lowering potential energy values to lane dividers.

2.2.2 Obstacle potential function

The obstacle potential function models the PF for surrounding static and/or dynamic obstacles on the road, including vehicles, pedestrians, motorcycles, etc. For second-branch algorithms described before (also the current mainstream), the obstacle PF not only establishes a safe field around obstacles but also serves as a guide for the ego vehicle's obstacle avoidance path generation. Since these algorithms rely on gradient descent, the shape of the obstacle PF is crucial. Its functions include guiding the ego vehicle through lane changes, overtaking, and more. In this thesis, we summarize several of the most popular obstacle potential functions currently in use.

Triangular potential function is first proposed at Wolf et al. [WB08] for collision avoidance. The following equation is designed to shape the PF in the forward/side and behind the obstacle:

$$U_{car,m}(K) = A_{car}\frac{e^{-\alpha K}}{K} \tag{2.4}$$

where A_{car} and α are the Yukawa [VK90] amplitude and scale of the obstacle potential. K is a distance measurement to the m^{th} obstacle vehicle, which forms a triangular field behind the obstacle. Huang et al. [HCWH19] proposed a novel hybrid system for multi-vehicle cooperative control in cooperative driving systems. This system combines discrete cooperative maneuvering modes (such as vehicle merging and platoon splitting) with continuous vehicle dynamics. Specifically, the front of the triangular PF is strengthened by introducing the concept of influence points. Yi et al. [YLQ+20] proposed a cooperative control model for connected and autonomous vehicles (CAVs) using the triangular PF. Unlike previous studies that focused on single-vehicle movement, this model considers the collective behavior of vehicles, ensuring not only travel safety but also enhanced driving comfort and improved traffic efficiency. Dixit, et al. [DMD+20] introduced a novel framework for autonomous overtaking in high-speed structured environments. The framework also combines a triangular PF-like function with reachability sets to identify safe zones on the road. Notably, the triangular PF is transformed into a diamond shape, distinguishing it from conventional approaches. Li et al. [LWC+21] developed a combined trajectory planning and tracking algorithm for autonomous vehicles. This algorithm incorporates human driving characteristics using the same triangular PF, enhancing user acceptance and trust in autonomous driving. The integration with MPC optimizes trajectories and control outputs, allowing the vehicle to adapt to traffic conditions and human driving styles. Yang et al. [YHZ22] presented an adaptive-grid

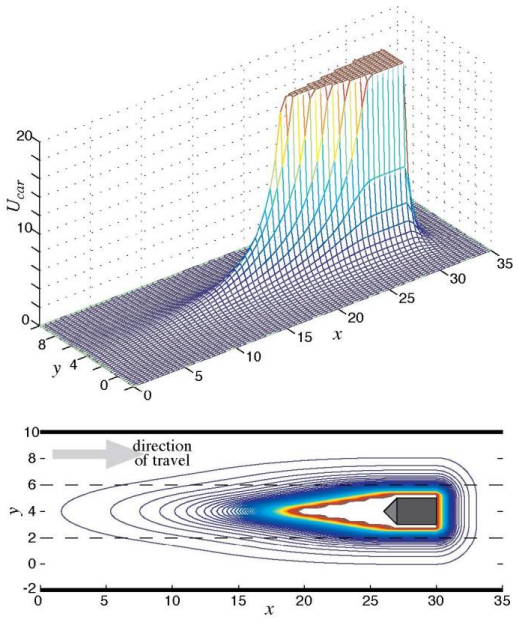


Figure 2.4: Triangular potential field of obstacle vehicle [WB08].

risk-field model for autonomous vehicles in structured road traffic environments, which utilizes a quadtree grid-dividing strategy, enhancing the accuracy of risk assessment in path planning. Lin et al. [LCLC20, LYQC22] later proposed a model predictive path planning algorithm for high-speed lane changes in autonomous vehicles. They addressed the practical limitations of the triangular PF in self-driving cars by introducing a novel curve-fitting method that considers lateral vehicle dynamics. The typical triangular shape of the obstacle PF is illustrated in Fig. 2.4.

While the triangular PF can guide the ego vehicle through the lane-change maneuver gently and has a low modeling cost, it does have several disadvantages. The first issue is that the triangular PF cannot address the problem of local minima. Additionally, it does not support continuous lane changes. Once the ego vehicle changes lanes by following the gradient of the rear triangular PF, it cannot return to the original lane unless it encounters the next obstacle vehicle.

Rectangular potential field was proposed in Rasekhipour et al.'s work (shown in Fig. 2.5) in 2017 [RKCL17], introducing a model predictive path-planning controller that combines the advantages of both APFs and optimal controllers for autonomous vehicles. The proposed controller incorporates vehicle dynamics in the path-planning process, ensuring optimal and stable

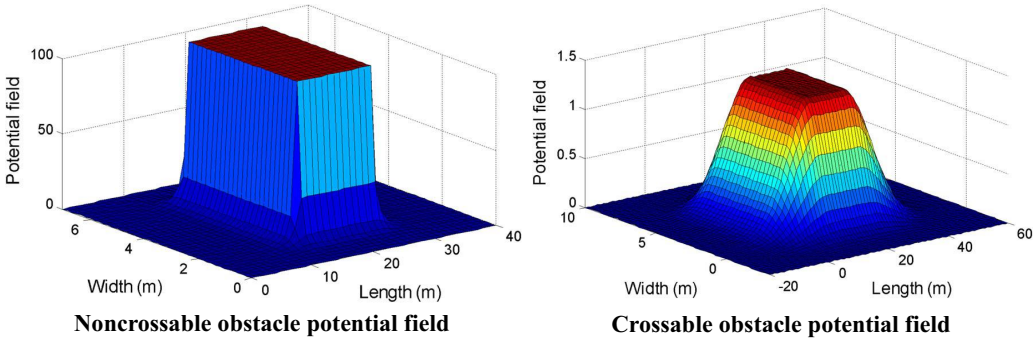


Figure 2.5: Noncrossable and crossable obstacle potential fields.

paths. Besides, they have designed specific PFs for both noncrossable U_{NC_i} and crossable obstacles U_{C_j} on the highway, as follows:

$$U_{NC_i}(X,Y) = \frac{a_i}{s_i\left(\frac{X}{X_{s_i}},\frac{Y}{Y_{s_i}}\right)^{b_i}} \tag{2.5}$$

$$U_{C_j}(X,Y) = a_j e^{-b_j s_j\left(\frac{X}{X_{s_j}},\frac{Y}{Y_{s_j}}\right)} \tag{2.6}$$

where $a_{i,j}$ and $b_{i,j}$ are intensity and shape parameters of the PF of i,j^{th} noncrossable and crossable obstacles, respectively. $X_{s_{i,j}}$ and $Y_{s_{i,j}}$ are the safe longitudinal and lateral distances from the obstacle that are calculated according to signed distance [Eri04]. Unlike the triangular PF, the rectangular PF is incorporated into the optimization function of the control layer. As a result, it does not generate waypoints for path planning; instead, it directly computes control signals, including the steering angle and either the pedal or the brake. Wang et al. [WHK+18, WHK+19] presented a path planning approach for autonomous vehicles to mitigate the effects of an inevitable crash. The adoption of a MPC algorithm incorporates APFs describing obstacles and crash severity into the control objectives, ensuring both obstacle avoidance and the reduction of crash impact. Lee et al. [LK19] came up with a Collision Avoidance/Mitigation System (CAMS) designed to address the challenge of collisions and driver interventions in autonomous vehicles. The proposed system employs a Predictive Occupancy Map (POM) for rapid risk assessment of surrounding vehicles, enabling the selection of the safest trajectory among local options to avoid critical situations. Li et al. [LLY+22] brought up a dynamic enhanced firework algorithm (dynEFWA)-APF, addressing challenges associated with traditional PF methods. The proposed approach enhances safety and smoothness by considering vehicle dynamics

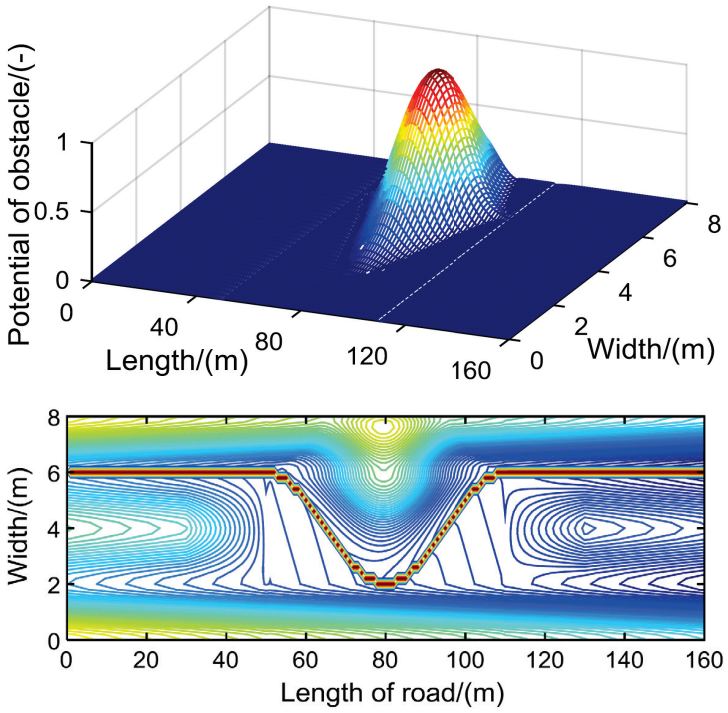


Figure 2.6: Ellipse-like potential field for path planning.

and various obstacle types. Tan et al. [TLL22] developed a novel method for uniformly modeling driving behavior across various scenarios. By integrating risk homeostasis theory and preview-follower theory within a field theory framework, the paper constructs a new risk field model, providing a cohesive approach to driving behavior modeling. Subsequently, Shang et al. [SE23] proposed a safe controller for emergency collision avoidance in diverse road environments, addressing a gap in existing research that often focuses on specific scenarios. The controller, employing the MPC and an artificial potential function inspired by a line charge, introduces a novel cost function. Unlike conventional algorithms, this approach considers collision mitigation, acknowledging scenarios with no feasible solution. Wang et al. [WG22] proffered a risk map-based path planning algorithm for autonomous vehicles. Utilizing Multivariate B-splines, a risk map is generated to assess collision risks with different objects. The algorithm involves a two-level optimal control problem, first identifying the overall lowest risk trajectory and then selecting the path with the minimum steering effort from those with the lowest risk values.

The rectangular PF is capable of handling more types of obstacle vehicles and provides full coverage of obstacle vehicles; however, it is unexpectedly

time-consuming and, at times, unable to find a solution. Additionally, it is also unable to generate waypoints directly, making it difficult to analyze whether the PFs are modeled accurately.

Ellipse-like potential field was first presented in Pozna et al. [PTP+09]'s work, which suggested a new mathematical construction for PFs in designing obstacle-avoiding trajectories. The work outlines an ellipse-like PF definition, introducing a design method for obstacle-avoiding trajectories through an algorithm with quick minimum computation. Later, Ji et al. [JKMH17] developed a 3-D virtual dangerous PF, depicted in Fig. 2.6, which is constructed based on Pozna's work, combining trigonometric functions of the road and the exponential function of obstacles to generate a collision-avoidance trajectory. The path-tracking controller formulates the tracking task as a multi-constrained MPC (MMPC) problem, calculating the front steering angle to prevent collisions with moving obstacles. The general potential function for constructing the ellipse-like PF is formulated as below:

$$U_{obs}(X,Y) = \frac{\left| e^{-c_1(X-X_o)^2 - c_2(Y-Y_o)^2} - P_t \right|}{1 - P_t} \tag{2.7}$$

where X_o represents the position of the obstacle in the X-direction of the fixed earth axis system. The parameters c_1, c_2, and P_t play crucial roles in determining the value and shape of the PF associated with the relative speed and distance between the vehicle and the obstacle. Specifically, P_t serves as the threshold dictating the extent of the repulsive PF, c_1 influences the weight on the lateral distance between the vehicle and the obstacle, and c_2 corresponds to the distance between the obstacle and the point where the collision avoidance maneuver commenced. Simultaneously, Raksincharoensak et al. [RHo16] introduced a motion planning and control system rooted in the collision risk potential prediction characteristics observed in experienced drivers, utilizing the optimization of the ellipse-like PF function within the framework of optimal control theory. Hamid et al. [HZZ+17, AHZY+18] proposed a Nonlinear MPC (NMPC)-based path tracking strategy integrated with the ellipse-like PF for motion planning. The architecture is designed to ensure optimal trajectory re-planning, considering vehicle dynamics, and accommodates move blocking strategies to mitigate computational burdens. Wang et al. [WGL+19] proposed a path-planning method by constructing a safety model based on human driver behavior, improving the ellipse-like PF method, and rebuilding the repulsive field range of obstacle vehicles. And then, Huang et al. [HDZ+20, HWK+20] introduced an innovative motion

planning and tracking framework for automated vehicles, utilizing the elliptical PF presented in Ji's work with an elaborated resistance approach. A local current comparison method identifies a collision-free path, while the spatiotemporal planning process is divided into virtual and actual spaces. The virtual space predicts and executes the vehicle trajectory, evaluating it before sending the information to the actual space. Lu et al. [LLY+20, LHY+20] came up with an adaptive PF designed to accommodate the acceleration/deceleration and mass of obstacles, established within a transformed road coordinate system to enhance feasibility and robustness. Additionally, their works also introduced a hybrid path planning method, combining the PF with the sigmoid curve to obtain an optimized trajectory considering vehicle dynamics constraints. After that, Lin et al. [LCC20b, LCYC20, LCC20a] addressed a novel waypoint tracking scheme integrating the ellipse-shaped PF with a clothoid curve. The method seamlessly connects the local path predicted by APF for obstacle avoidance with irregular waypoints, reducing severe yawing. The introduced speed planning effectively prevents excessive tire slip angles at high speeds. Hang et al. [HLH+20, HHH+21] proposed an integrated approach for autonomous vehicles' lane-change maneuvers, incorporating the social behaviors of surrounding vehicles. It combines Stackelberg Game theory for decision-making. The motion planning utilizes a PF model with different potential functions describing diverse behaviors of surrounding vehicles, and MPC for the path tracking task.

Recently, Wang et al. [WYZ+22] and Yan et al. [YWZ+22] address the critical aspect of path planning for enhancing driving safety and driver comfort in autonomous vehicles (autonomous vehicles), particularly in scenarios with large road curvatures. A Driver-Vehicle-Road (DVR) system is introduced, combining the kinematic vehicle model with the two-point visual preview driver model, accommodating individual driver characteristics. The banana-shaped PF, modified from the elliptical one, addresses environmental constraints by forming a 3-D dangerous imaginary mountain and a lane boundary cliff. Xie et al. [XHB+22] presented a distributed motion planning algorithm for ensuring the safe overtaking of autonomous vehicles in a dynamic environment using the elliptical PF. The key contributions include formulating the overtaking problem as a multi-target tracking problem, and introducing velocity and acceleration difference PFs for modeling a multi-vehicle system. Similarly, Wu et al. [WGL22] introduced a novel lane-changing algorithm for autonomous vehicles, aiming to enhance human-like behavior while considering environmental risks, driver speed requirements, and focus-shifting processes. The algorithm utilizes the PF and analyzes the coupling relationship between longitudinal and lateral forces, incorporating a conversion mechanism to mimic the driver's speed preferences. Ji et

al. [JNZ+23] proposed a novel three-dimensional potential field (TriPField) model for autonomous vehicles, addressing challenges in scenarios with dense and dynamic obstacles. Integrating an ellipsoid PF with a Gaussian velocity field, the TriPField considers the geometric shape of surrounding vehicles, overcoming local minima issues and demonstrating improved path efficiency in various traffic scenarios. Chu et al. [CLZZ22] a trajectory planning and tracking framework that utilizes the elliptical PF for target trajectory generation and combines it with MPC featuring PID feedback for accurate trajectory tracking. Shang et al. [SE23] addressed the lack of a general method for emergency collision avoidance across various road environments. It introduces a safe controller employing MPC and a novel potential function inspired by line charge, capable of accommodating road structures and achieving collision mitigation in specific areas. Du et al. [DZZ+23] presented an efficient hierarchical framework encompassing motion planning and tracking control for autonomous vehicles. The framework introduced a global heuristic planning-based PF method for real-time optimal motion sequencing and a prioritized Q-learning-based forward predictive control method to enhance tracking control effectiveness.

In summary, the ellipse-like PF is currently the mainstream algorithm for establishing the obstacle PF compared to the other two shapes. It supports continuous lane changes and can produce a smoother path during collision avoidance. Besides, it also offers adjustability for both the longitudinal and lateral directions of the PF. However, the increased number of parameters requires more tuning efforts, and it might encounter local minima in specific scenarios.

2.2.3 Attractive potential function

The attractive potential function is designed to create an attraction field that generates a force pulling the vehicle toward the goal location. The strength of this force decreases as the vehicle gets closer to the goal, ensuring a smooth and controlled approach. In Wolf et al. [WB08], the so-called velocity potential U_{vel} is designed to generate a propelling force when the vehicle is below its desired speed and a retarding force when the vehicle exceeds its desired speed, as shown below:

$$U_{vel} = \gamma(v - v_{des})X \tag{2.8}$$

where v is the longitudinal speed of the ego vehicle while v_{des} marks the desired longitudinal speed. γ is a constant factor. However, Eq. (2.8) can only produce a forward force without other orientations, which only makes the

ego vehicle move aimlessly. Therefore, Ji et al. [JKMH17] samples the target point from the desired lane center with the following attractive function $U_{attr}(X, Y)$ to compute the force:

$$U_{attr}(X, Y) = \frac{|X - (X_o + 0.5D_s)| + |Y - Y_{lc}|}{100} \tag{2.9}$$

where D_s signifies the extent of the universal PF utilized for collision avoidance along the X-direction of the fixed Earth axis system, while Y_{lc} indicates the desired lane center along the Y-axis direction of the fixed Earth axis system.

The design of the attractive potential function should be simplified, given its role in creating attraction. Essentially, the attractive PF contributes to effective path planning, promoting the safe and efficient navigation of autonomous vehicles toward their intended destinations. In general, the attractive potential function is usually velocity-oriented or lane center-oriented, but there also exist point-oriented approaches on unstructured roads that are similar to the field of mobile robots.

2.2.4 Universal potential field

When the modeling of required PFs is completed as described above, we can superimpose them to obtain the universal PF U_{univ} for the current road situation:

$$U_{univ} = U_{road} + U_{lane} + U_{obs} + U_{attr} \tag{2.10}$$

Then, we can apply gradient descent to calculate the total forces F_t:

$$F_t = -\nabla U_{univ} = -\begin{bmatrix} \frac{\partial U_{univ}}{\partial X} \\ \frac{\partial U_{univ}}{\partial Y} \end{bmatrix} \tag{2.11}$$

Once we obtain the total forces, we can use them to calculate the reference signal for the heading angle ψ_{ref} of the ego vehicle:

$$\psi_{ref} = \arctan\left(\frac{F_t(Y)}{F_t(X)}\right) \tag{2.12}$$

Finally, the planned path waypoints X_{ref} and Y_{ref} can be determined using a predefined discrete step length L_s:

$$\begin{cases} X_{ref} = X + L_s cos(\psi_{ref}) \\ Y_{ref} = Y + L_s sin(\psi_{ref}). \end{cases} \tag{2.13}$$

It should be noted that Eq. (2.13) can be iterated within a control loop, following the predefined number of required waypoints. Therefore, we can obtain a local path consisting of waypoints at each time step by calculating the universal PF.

2.3 Motivation

2.3.1 Motivation of potential field-based path planning

Potential field-based path planning lies in its ability to offer a simple yet effective approach for autonomous vehicles to navigate through their driving environment. By modeling the interaction between the ego vehicle and surrounding obstacles as PFs, with attractive forces guiding the ego vehicle toward the goal and repulsive forces preventing collisions, this method provides a computationally efficient way to generate collision-free trajectories. As mentioned, collision avoidance and driving safety are the major concerns and challenges of discouraging the commercialization of autonomous vehicle, in which the public still harbors doubts about the handling capabilities of autonomous vehicles in emergency scenarios. The PF-based path planning can collect information about vehicles and obstacles from the surrounding environment to establish a 3D dangerous PF, which can be used to analyze the current driving state and collision risks. Crucially, its exceptional real-time obstacle avoidance efficiency makes it well-suited for the path planning of autonomous vehicles with highly demanding safety and real-time performance requirements.

In previous studies, PF-based path planning methods rely heavily on the pre-designed rules and the PF models [WGL22, LYQC22, WG22, LLY+22, XHB+22, JNZ+23, DZZ+23, SE23]. These works concentrate on refining the PF models to improve path quality and integrating them with MPC for more accurate path tracking in common driving scenarios. Furthermore, these works predominantly concentrate on stand-alone (non-connected) autonomous vehicles, heavily relying on sensor information to plan collision-free paths for the ego vehicle. Cooperative planning based on vehicle-to-vehicle (V2V) communication is rarely discussed in PF-related works, particularly within emergency situations. Thereby, in this thesis, we primarily address the following research questions, which serve as our motivations for PF-based path planning:

How can a collision-free path be ensured or minimize crash severity in non-cooperative emergencies when the PF faces inherent limita-

tions? This research question arises from cases where the performances of the PF-based path planning methods are less satisfactory in handling challenging scenarios, such as occlusions, sudden lane-change obstacles, etc.

How can effective emergency cooperative planning be conducted via V2V communication to ensure driving safety? In cooperative scenarios where autonomous vehicles can share information through V2V communication, it still remains unclear how to effectively utilize this information for PF modeling and cooperative planning, such as determining who should compromise, whether to decelerate or change lanes, and so on.

What should be done if the PF-based path planning malfunctions completely? PF-based path planning approaches implicitly assume that the PF can plan a local path at all times. However, some emergency situations can trigger the inherent limitations of the PF during collision avoidance, leading to planning paralysis.

2.3.2 Motivation of hazardous scenario-based simulation

Common driving scenarios are everyday situations that most drivers encounter regularly, such as driving on a clear, well-maintained road, obeying traffic rules, and following standard driving practices. These scenarios typically involve lower levels of risk and are considered routine and safe when drivers follow traffic laws and exercise caution, such as obeying speed limits, using turn signals, and maintaining safe following distances. Emergency responses are generally not required in common driving scenarios. In previous works [JKMH17, HDZ+20, WGL+19, HWK+20, LCC20b, LCLC20, WYZ+22], they only consider one obstacle vehicle ahead with a predefined single motion, for example, driving straightly with constant speed or acceleration. Although Wang et al. [WHK+19, WGL+19] have simulated their methods in emergency scenarios, they are committed to mitigating the crash severity by assuming the collision is inevitable. Some emergency cases, such as emergency braking and dangerous lane-change behaviors, have been addressed and analyzed in Lu et al. [LHY+20] and Shang et al. [SE23]. However, certain emergency scenarios that could challenge the utmost or inherent limitations of the PF have not been discussed or considered. In this thesis, our motivation to engage the hazardous scenario-based simulation lies in the following points:

Exploring the utmost or inherent limitations of PF-based path planning We are dedicated to studying hazardous driving scenarios to explore the vulnerabilities of PF-based path planning approaches in specific situations. Furthermore, by simulating these driving scenarios, we can investigate the potential causes of PF malfunctions and their corresponding solutions.

Emergency Response Preparedness To customize the design of emergency response algorithms, targeted safety evaluation and testing are conducted in hazardous scenarios. Additionally, a 3D PF is established to analyze the states of obstacle vehicles. Fail-safe mechanisms are introduced to bring the ego vehicle to a safe stop or safely maneuver to the side of the road in order to mitigate additional risks, such as secondary accidents.

2.4 Current challenges

As mentioned, the challenges in autonomous vehicles encompass the following aspects: sensor failure, software glitches, communication issues, and urgent traffic conditions. In this thesis, we delve deeper into planning paralysis caused by software glitches and hazardous scenarios occurring during urgent traffic conditions.

Challenges of lane-change strategies Lane-change methods based on conventional PFs typically depend on the geometry of the obstacle PF. In such cases, the resulting path often becomes excessively long and closely follows or runs parallel to the position of the obstacle vehicle. Moreover, the curvature of conventional PF-based lane change paths can be significant, potentially causing discomfort for passengers. Furthermore, these conventional methods may pose an increased risk of collision if the obstacle vehicle makes a sudden and unexpected steering maneuver toward the ego vehicle without prior warning, particularly in emergency situations.

Challenges of occlusion problem The occlusion problem in autonomous driving refers to the challenge of handling objects or obstacles that are partially or completely hidden from the sensors' view due to the presence of other objects, vehicles, or environmental conditions. The PF-based methods require a full knowledge of the surrounding environment, which faces the challenges in solving the occlusion problem. The PF-based methods require a complete knowledge of the surrounding environment, posing challenges in addressing the occlusion problem.

Challenges of the PF modelings Contemporary PF models incorporate inviolable road potential functions, establishing constraints preventing vehicles from deviating off the road. These models operate under the implicit assumption that all collision avoidance maneuvers can be effectively executed within the confines of the roadway. Furthermore, the potential energy assigned to the Z-axis of the obstacle PF remains consistently set at a substantial value, which makes it difficult to analyze the driving intention of obstacle vehicles.

Challenges of cooperative planning Cooperative planning must also navigate the complexities of a heterogeneous traffic environment, accounting for the diverse behaviors of human drivers, pedestrians, and cyclists. The dynamic and uncertain nature of road conditions, coupled with mixed autonomy levels, adds complexity to planning algorithms. Additionally, legal frameworks and regulations must be established to address liability, responsibility, and compliance standards.

Challenges of emergency response Coordinating swift and effective reactions to unforeseen events demands seamless communication and collaboration between autonomous vehicles. When planning algorithms malfunction, the logical response must prioritize safety and efficient resolution. Rapid communication between the malfunctioning vehicle and other autonomous and non-autonomous entities becomes crucial to avoid potential hazards.

2.5 Main contributions

Our primary contributions to this thesis can be delineated into the following three parts:

In the first part, we propose a time-to-collision (TTC)-aware lane-change strategy based on the cubic polynomial in which the TTC is imposed as a constraint for the optimized curve fitting. Then, we refine the PF with responsibility-sensitive safety (RSS) models for the occlusion problem. In the construction step, we first categorize the detected and occluded obstacles and then proceed to the RSS violation check. Finally, we can generate different virtual forces from the PF for occluded and non-occluded obstacles. Besides, we design an emergency triggering estimation to identify the 'blind alley' problem by analyzing the PF distribution. We then introduce Emergency-Stopping Path Planning (ESPP), which utilizes an optimized clothoid curve to generate a smooth emergency avoidance path. Compared with the conventional approaches, our path planner performs much better in lane-change

path generation, solving occlusion problems, and conducting a safe emergency stop.

In the second part, we leverage V2V communication to enhance the PF with additional valuable information. This augmentation allows for adaptive variations in potential energy on the Z-axis, enabling a better understanding of the driving intentions of surrounding objects. Afterward, we enhance the adaptive PF by incorporating the RSS-enhanced sigmoid curve for connected autonomous vehicles. In addition, we design an interactive speed optimization (ISO) for longitudinal planning, enabling connected vehicles to share their local paths by solving a constrained objective function. In the evaluation stage, our proposed V2V-based path planner demonstrates superior performance in terms of computational complexity, overcoming local minima, and exhibiting highly efficient merging behaviors.

The emergency response is a vital challenge in the path planning part, in the last part of this thesis, we address an emergency triggering analysis algorithm on monitoring traffic emergencies and planning malfunctions. In the context of perceived emergencies, we introduce a novel Safety Tunnel (ST)-based Model Predictive Controller (STMPC). The ST, composed of a sigmoid curve, is integrated into the MPC-based tracking controller as a safety constraint sensitive to surrounding environments for emergency navigation, such as road structure and obstacles. In the performance evaluation, our proposed STMPC method demonstrates the ability to anticipate potential PF malfunctions and navigate the vehicle for emergency collision avoidance, while other approaches fail to plan a collision-free path.

In summary, the critical contributions of our thesis are to a novel PF-based path-planning method that can respond promptly and plan paths in emergency driving scenarios. Compared with other baselines, our proposed approaches have addressed the computation complexity, communication application, emergency response, rule-based responsibilities, and the inherent limitations of the PF.

Chapter 3

Potential Field-based Path Planning for Emergency Avoidance

3.1 Introduction

Emergency avoidance is critical to autonomous vehicle navigation, requiring swift and effective responses to unforeseen hazards. PF-based path planning emerges as a crucial strategy in this context, leveraging the concept of PFs to guide vehicles through dynamically changing environments. In this approach, the vehicle perceives its surroundings as a field of forces, where attractive forces pull it toward the destination, and repulsive forces repel it from obstacles. This introduction explores the significance of PF-based path planning in the realm of emergency avoidance, delving into its principles, advantages, and applications. By dynamically adapting to the surrounding environment, this chapter provides a promising framework for crafting paths that prioritize safety and efficiency, establishing it as a crucial element in the development of robust autonomous navigation systems.

This chapter aims to implement a descent path planning strategy for both non-connected and connected autonomous vehicles. A non-connected autonomous vehicle (NAV), as shown in Fig. 3.1, refers to a conventional vehicle lacking the advanced communication capabilities associated with connected vehicles. Unlike their connected counterparts, NAVs typically do not have the ability to exchange real-time data with other vehicles, infrastructure, or external networks. These vehicles operate independently and rely solely on onboard sensors, cameras, and systems for navigation and decision-making. In contrast to connected vehicles that can communicate with each other and

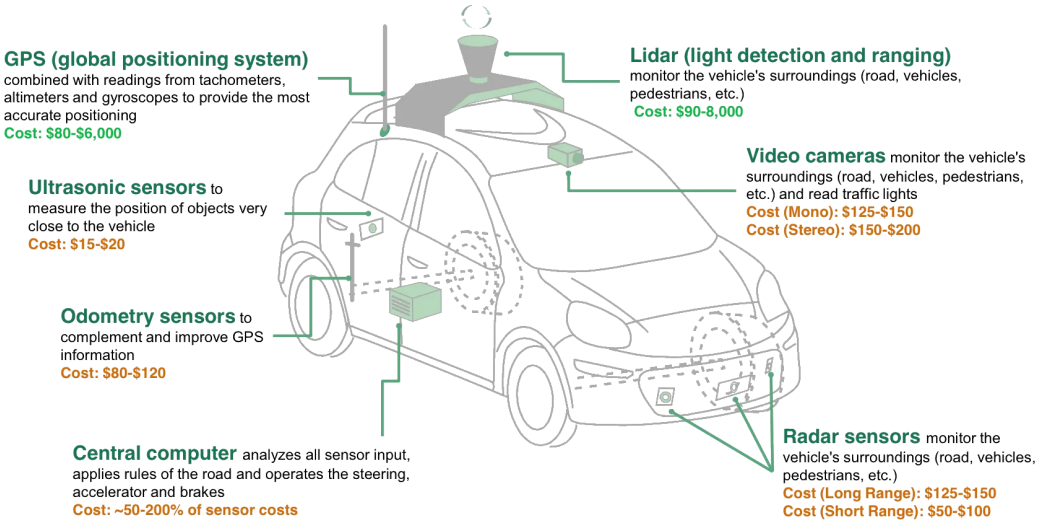


Figure 3.1: Non-connected autonomous vehicles with sensing, decision-making, and control capabilities [Dav15].

with intelligent infrastructure to enhance safety and efficiency, NAVs rely primarily on the awareness and reactions of human drivers for navigation and response to traffic conditions. As the automotive industry progresses towards greater connectivity, the term 'non-connected vehicle' distinguishes these conventional vehicles from those integrated into emerging connected and autonomous transportation ecosystems. NAVs suffer from limited perception due to the absence of V2X communication, which impedes their ability to interact with other vehicles and infrastructure. This isolation can lead to economic burdens, as the full potential of networked traffic management and cost-saving through fleet optimization still needs to be explored. Without the collaborative benefits of a connected ecosystem, these vehicles face challenges in dynamic decision-making and efficiency.

Connected autonomous vehicles (CAVs), depicted in Fig. 3.2, represent a significant advancement in vehicular technology, integrating automation with connectivity. These vehicles are equipped with sensors and communication technologies that allow them to perceive their environment and make informed decisions based on data. Through Vehicle-to-Everything (V2X) communications, CAVs can interact with other vehicles, traffic management systems, pedestrians, and even road infrastructure, enabling them to adapt to traffic conditions, coordinate with other vehicles for safety and efficiency, and receive updates about road hazards or operational changes in real-time. This connectivity extends their situational awareness beyond their immediate

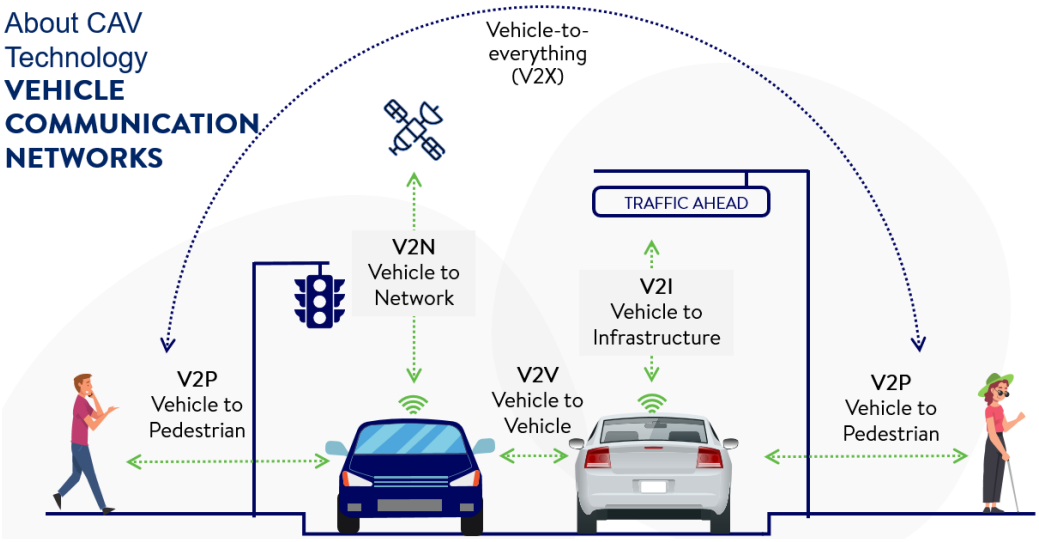


Figure 3.2: Connected autonomous vehicles combining connectivity and automated technologies to assist or replace humans in the task of driving [Edm22].

line of sight, enhancing safety features and driving efficiencies. For example, by communicating with traffic signals (V2I or Vehicle-to-Infrastructure), autonomous vehicles can optimize their speed to move through intersections more smoothly, reducing congestion and emissions. They can also communicate with each other (V2V or Vehicle-to-Vehicle) to synchronize their movements, allowing for tighter platooning and drafting to improve fuel efficiency and increase road capacity. The data exchanged among CAVs and infrastructure can also be leveraged for broader traffic analysis and city planning. Overall, CAVs promise to transform the transportation landscape by improving road safety, reducing traffic congestion, and creating a more sustainable and efficient transportation ecosystem.

3.2 Overview

Fig. 3.3 presents an overview of path planning strategies, categorized into non-cooperative and cooperative approaches for NAVs and CAVs.

Time-to-Collision-Aware Lane Change: This non-cooperative method uses the time-to-collision (TTC) metric to determine safe lane changes by calculating the time remaining before a potential collision occurs if the current

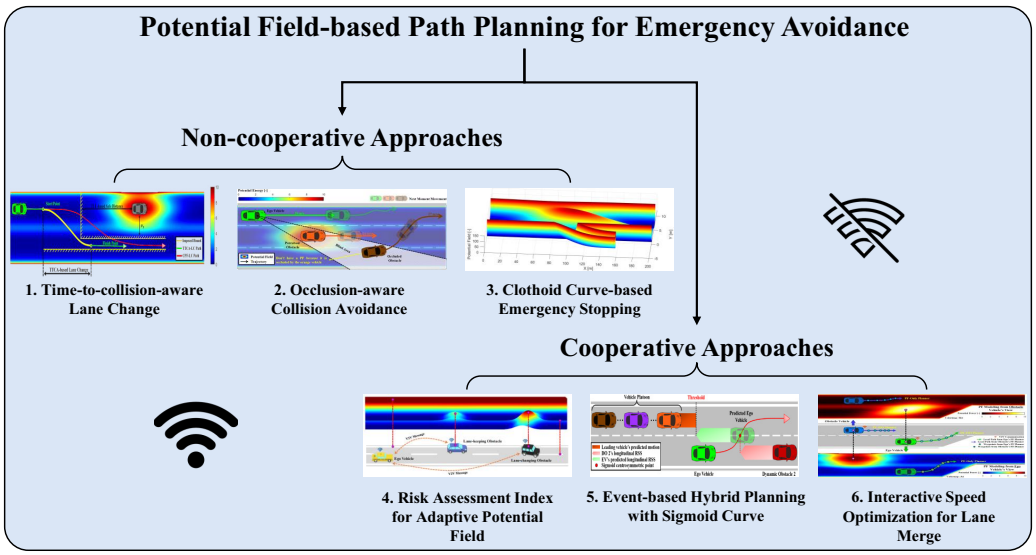


Figure 3.3: Overview of potential field-based path planning for emergency avoidance.

speed and trajectory are maintained.

Occlusion-Aware Collision Avoidance: This study focuses on avoiding collisions with objects that are not directly visible due to occlusions in the environment, relying on the adjustments of the virtual forces of the PF.

Clothoid Curve-Based Emergency Stopping: This approach employs clothoid curves, which are used in road design for gradual turns, to enable smooth and efficient emergency stops when needed.

Risk Assessment Index for Adaptive Potential Field: In the cooperative domain, this method assesses risks in the environment and adjusts the PF accordingly to adapt the path planning dynamically.

Event-Based Hybrid Planning with Sigmoid Curve: This cooperative technique uses events, such as the detection of another vehicle, to trigger hybrid path planning. The use of sigmoid curves likely helps in smoothing the transition between path segments.

Interactive Speed Optimization for Lane Merge: This approach optimizes the vehicle's speed interactively to facilitate a smooth lane merging

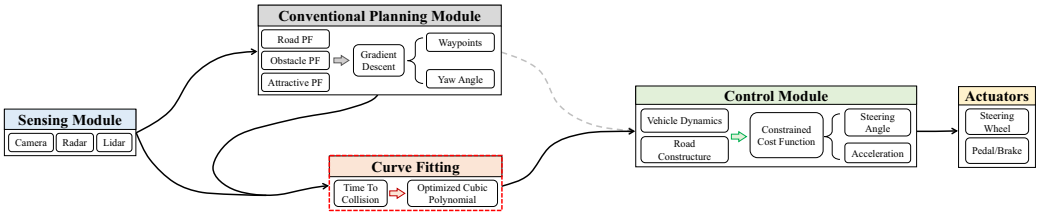


Figure 3.4: Proposed TTCA-LC strategy: Curve fitting computes the optimized cubic polynomial by considering the waypoints and yaw angle from the planning module as well as the TTC from the sensing module.

process, considering the movements of other vehicles to ensure safety and efficiency.

3.3 Planning in non-connected vehicles

3.3.1 Time-to-collision-aware lane change

Enabling secure and successful lane changes (LCs) is among the crucial functions that autonomous vehicles must perform to ensure safe travel on highways. Recently, there has been a growing interest in utilizing the PF method for designing decision and planning modules in NAV due to its real-time performance and simplicity. However, the LC trajectories generated by the PF method often result in longer paths that bring the ego vehicle very close to obstacle vehicles, posing a safety risk if the obstacle vehicle suddenly changes its course. To address this safety concern, we introduce a Time-to-Collision-Aware Lane Change (TTCA-LC) strategy that incorporates the TTC constraint into the optimized curve fitting process. This strategy enhances the safety of lane changes while still leveraging the advantages of the PF method and cubic polynomial curves. The results described in this subsection have been published in [6].

The PF method has been recently applied to the LC task, a critical metric for evaluating autonomous driving systems. Conventionally, the LC path is constructed by defining the obstacle PF's geometry, such as a triangle [WB08] or an ellipse [JKMH17]. This path is produced along the obstacle PF's boundary through the gradient descent (GD) method, meeting the real-time performance needs of autonomous vehicles' lower control systems. However, in high-speed driving scenarios, the PF-based LC strategy often results in an extended path to ensure safety. Moreover, the endpoint of the PF-based LC tends to be laterally parallel or near the obstacle, as the obstacle PF's

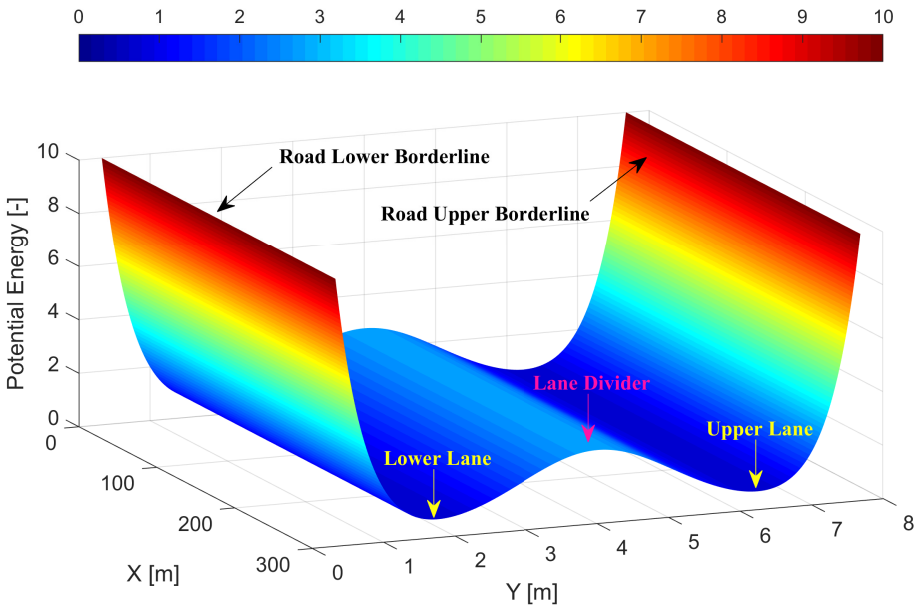


Figure 3.5: 3D view of road potential field.

geometry design is centered around the obstacle vehicle's center of gravity (c.g.). This can lead to potential collision risks if adjacent obstacles make sudden, unanticipated maneuvers. To enhance the LC path's quality, this study introduces a time-to-collision-aware LC strategy that refines the PF-determined path using an optimized cubic polynomial, illustrated in Fig. 3.4. The key contributions of this paper are summarized as follows:

- We propose using an optimized cubic polynomial to process waypoints derived from the PF, creating a trajectory that is simpler and more intuitive to follow.
- The TTC is employed in the constraint design for optimization, enabling autonomous vehicles to complete the LC ahead of time and maintain ample space to avert emergencies.

PF-based lane change strategy

This subsection presents the potential functions used to establish the PF, along with the proposed cubic polynomials for waypoint processing.

Lane-change potential functions Within the context of road structures, the potential functions are comprised of three components: attractive, road, and obstacle potentials. The purpose of the attractive potential is to propel a vehicle forward, and the associated potential function, P_a, is employed to generate an attractive force:

$$P_a = \frac{1}{2}\lambda \left(X - X_{tar}\right)^2, \tag{3.1}$$

where λ represents the slope scale, while X and X_{tar} indicate the longitudinal positions of the vehicle and the target point, respectively. Considering that a road typically includes visible edges, lanes, and lane dividers, the road potential function, P_r, is defined as follows:

$$P_r = \frac{1}{2}\xi(\frac{1}{Y - Y_{l,u} - \frac{l_w}{2}})^2 + A_{lane}\exp\left(-\frac{(Y - Y^i_{lane})^2}{2\sigma^2}\right), \tag{3.2}$$

where ξ symbolizes the scaling coefficient, and Y represents the lateral position of the ego vehicle. $Y_{l,u}$ refers to the lateral positions of both road edges, while l_w denotes the width of the vehicle. A_{lane} is the amplitude of the lane divider's potential field (PF), and Y^i_{lane} is the lateral position of the i^{th} lane divider. σ indicates the rising/falling slope of the lane potential. The road potential is illustrated in Fig. 3.5. As previously discussed, an obstacle's PF is utilized to demarcate a boundary region that maintains a safe distance from the ego vehicle, assigning graduated risk values. The obstacle's PF is crucial in shaping the LC trajectory, which generally aligns with the edge of the PF boundary region. Consequently, the obstacle potential function, P_o, is employed as detailed in [LCLC20]:

$$P_o = A_{obs}\exp\left[-\frac{C_1}{2}\left(\frac{(X - X_o)^2}{\sigma_x} + \frac{(Y - Y_o)^2}{\sigma_y} - C_2\right)\right], \tag{3.3}$$

where

$$\begin{aligned}
&C_1 = 1 - \psi_o^2, \quad C_2 = \frac{2\psi_o(X - X_o)(Y - Y_o)}{\sigma_x\sigma_y}, \\
&\sigma_x = D_{min}\sqrt{-\frac{1}{\ln U}}, \quad \sigma_y = \sqrt{-\frac{(Y - Y_o)^2}{2\ln\frac{U}{A_{obs}}}}, \\
&D_{min} = \frac{Mv^2}{2a_b} - \frac{M_o v_o^2}{2a_{b,o}} + \frac{l_{fr} + l_{fr,o}}{2}.
\end{aligned}$$

X_o and Y_o represent the longitudinal and lateral positions of the obstacle vehicle, respectively. The term ψ_o refers to its heading angle, while U is

the minimum positive factor. The weights of the ego and obstacle vehicles are denoted by M and M_o, respectively. The longitudinal speeds of the ego and obstacle vehicles are indicated by v and v_o. The maximum deceleration achievable through braking for the ego and obstacle vehicles are a_b and $a_{b,o}$, respectively. The terms l_{fr} and $l_{fr,o}$ represent the wheelbases of the host and obstacle vehicles, respectively. By summing Eqs. (3.1)-(3.3) and implementing the gradient descent method as cited in [Rud16], the universal PF is derived, resulting in the virtual net force $\overrightarrow{F_N}$.

$$\overrightarrow{F_N} = -\nabla P_u = \overrightarrow{F_a} + \overrightarrow{F_r} + \overrightarrow{F_o^i}, \tag{3.4}$$

where

$$P_u = P_a + P_r + \sum_{i=1}^{i} P_o,$$

with $\overrightarrow{F_a}$ is the virtual attractive force from Eq. (3.1). $\overrightarrow{F_r}$ is the virtual repulsive forces from Eq. (3.2). $\overrightarrow{F_o^i}$ means the i^{th} virtual repulsive force from Eq. (3.3). Therefore, the ego vehicle can drive toward the target point while avoiding the obstacle under the interaction of these virtual forces. Then, with the obtained net force $\overrightarrow{F_N}$, we can calculate the desired heading angle θ_{des} by the following equation.

$$\theta_{des} = \arctan \frac{\overrightarrow{F_N^y}}{\overrightarrow{F_N^x}}, \tag{3.5}$$

with

$$\overrightarrow{F_N^y} = -\frac{\partial P_u}{\partial Y}, \quad \overrightarrow{F_N^x} = -\frac{\partial P_u}{\partial X}.$$

The LC trajectory is then obtained, as shown in Fig. 3.6.

Clothoid curve To produce a smooth and easy-to-follow trajectory, the cubic polynomial is frequently used for processing discrete waypoints, resulting in a smaller control effort for car-like robots [NK01]. Similarly, the cubic polynomial is utilized for autonomous vehicles when tracking Global Positioning System waypoints [JKLC15], as shown in Fig. 3.7. In this study, we propose including the TTC in the constraint design while solving the optimization. First, the standard cubic polynomial is formulated as

$$f(x) = a_0 + a_1 x + a_2 x^2 + a_3 x^3, \tag{3.6}$$

where a_0, a_1, a_2, a_3 are the parameters of the cubic polynomial, and x

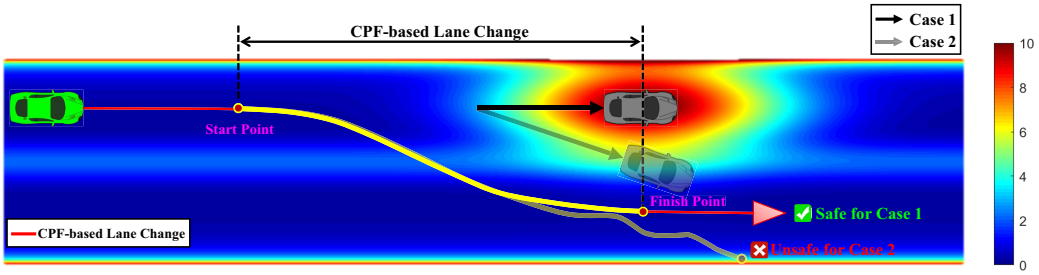


Figure 3.6: Conventional potential field-based lane-change strategy for different driving cases on the highway.

represents the waypoints. Next, we reshape Eq. (3.6) into a quadratic programming form for optimization:

$$\mathbf{f} = \min_{\mathbf{a}} \frac{1}{2} \left(\mathbf{Xa} - \mathbf{Y}\right)^T W \left(\mathbf{Xa} - \mathbf{Y}\right), \tag{3.7}$$

where

$$\mathbf{X} = \begin{bmatrix} 1 & x_1 & {x_1}^2 & {x_1}^3 \\ 1 & x_2 & {x_2}^2 & {x_2}^3 \\ \vdots & \vdots & \vdots & \vdots \\ 1 & x_N & {x_N}^2 & {x_N}^3 \end{bmatrix}, W = \begin{bmatrix} w_1 & 0 & \cdots & 0 \\ 0 & w_2 & \cdots & 0 \\ \vdots & \vdots & \ddots & \vdots \\ 0 & 0 & \cdots & w_N \end{bmatrix},$$
$$\mathbf{a} = \begin{bmatrix} a_0 & a_1 & a_2 & a_3 \end{bmatrix}^T, \ \mathbf{Y} = \begin{bmatrix} y_1 & y_2 & \cdots & y_N \end{bmatrix}^T.$$

$\mathbf{a}$ denotes the optimal cubic coefficient, and $(x_N,\ y_N)$ represents the N^{th} waypoint from the PF. w_N is the weight. Note that at least four waypoints are required to calculate $\mathbf{a}$. Next, we introduce the TTC, which represents the time required for the two vehicles to collide if they maintain the same speed driving along the same path [Lee76]. As depicted in Fig. 3.8, we denote D_{rela} as the relative distance between the vehicles, and D_{stop} is the minimum safe stopping distance for the rear vehicle. We generally consider two collision cases when calculating TTC. The first is when the minimum D_{rela} occurs after the front vehicle makes a complete stop, and the second is when the minimum D_{rela} occurs before the front vehicle completes its stop. In the first case, we use the following formula:

$$TTC = \begin{cases} \frac{D_{rela} - D_{stop} + \frac{v_2^2}{2|a_2|}}{v_1}, & a_1 = 0 \\ \frac{-v_1 + \sqrt{v_1^2 + 2a_1(D_{rela} - D_{stop} + \frac{v_2^2}{2|a_2|})}}{|a_1|}, & a_1 \neq 0, \end{cases} \tag{3.8}$$

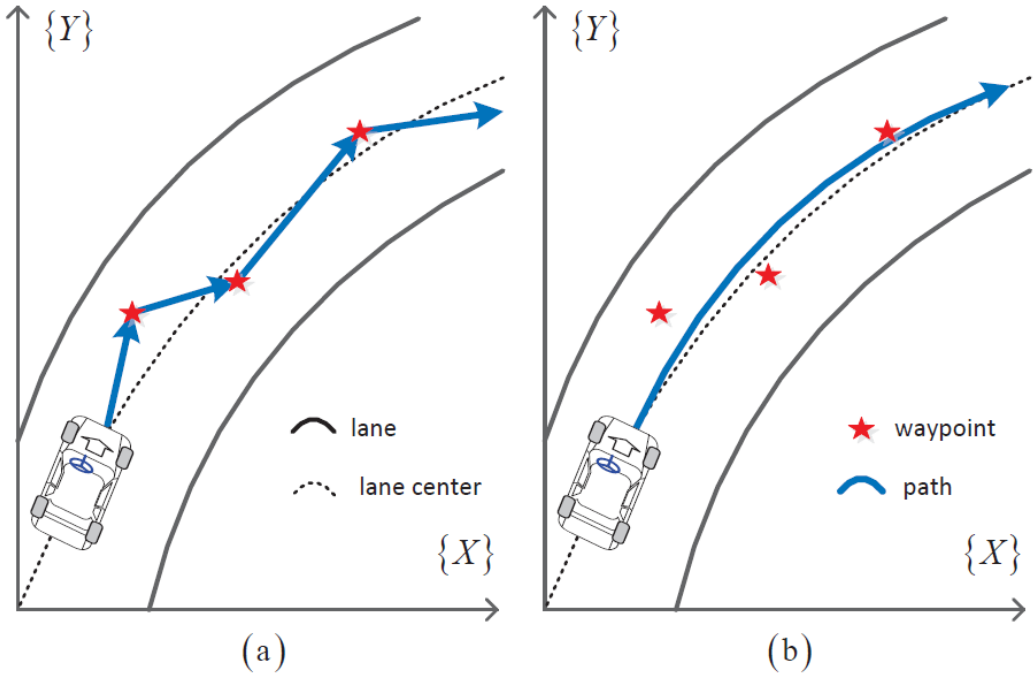


Figure 3.7: Waypoint tracking methods [JKLC15]: (a) point-wise, (b) curve-fitting.

where v_1 and a_1 denote the speed and acceleration of the rear vehicle, respectively. v_2 and a_2 are the speed and acceleration of the vehicle in front, respectively. In the second case, the TTC is obtained as follows:

$$TTC = \begin{cases} \frac{D_{rela}-D_{stop}}{v_{rela}}, & a_{rela} = 0 \\ \frac{-v_{rela}+\sqrt{v_{rela}^2+2a_{rela}(D_{rela}-D_{stop})}}{a_{rela}}, & a_{rela} \neq 0, \end{cases} \tag{3.9}$$

where

$$v_{rela} = |v_1 - v_2|, \quad a_{rela} = |a_1 - a_2|.$$

TTC is also an important indicator in the design of a forward collision warning system. Therefore, the standardization of TTC directly impacts traffic management. For example, an excessive TTC can lead to aggressive driving maneuvers, and an undersized TTC cannot ensure safety. The Mobileye Incorporation [Mob22] sets a 2.7-s TTC alert. Moreover, [APH21] found that approximately 93% of observed drivers complete LC maneuvers in less than 5 s. More than half completed LCs around 3.5 s. Thus, we set the constraint based on the critical TTC value and the appropriate LC duration. As shown

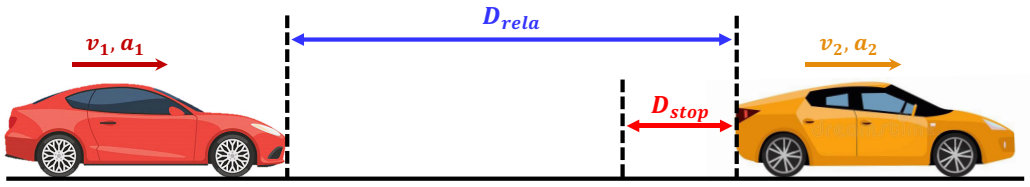


Figure 3.8: Two vehicles driving in the same direction: red vehicle (rear) drives at (v_1, a_1); orange vehicle (front) drives at (v_2, a_2).

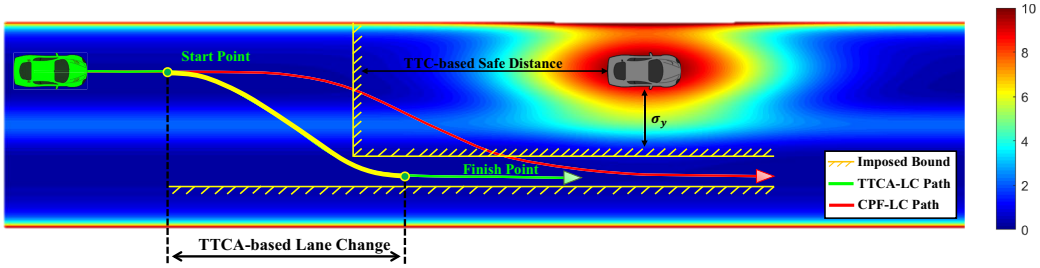


Figure 3.9: Proposed time-to-collision-aware lane-change strategy with the potential field: using the TTC for constraint design that allows the ego vehicle to complete the LC in advance, reserving sufficient space for deceleration if the obstacle suddenly steers.

in Fig. 3.9, we impose the lower and upper bounds to regulate the cubic polynomial while fitting the waypoints from the PF. Hence, we can optimize Eq. (3.7) with bounded constraints as follows:

$$\mathbf{f} = \min_{\mathbf{a}} \frac{1}{2} (\mathbf{Xa} - \mathbf{Y})^T W (\mathbf{Xa} - \mathbf{Y}) \tag{3.10}$$

$$\text{s.t.} \quad \mathbf{Xa} \leq \sigma_y, \quad if\ X_{start} \leq X \leq X_{end} \tag{3.8a}$$

$$\mathbf{Xa} \geq Y_{lb}, \quad if\ X_{start} \leq X \leq X_{end}, \tag{3.8b}$$

where

$$X_{start} = X_{obs} - v(TTC + T_{LC}),$$
$$X_{end} = X_{obs} + \sigma_x,$$

and T_{LC} denotes the optimal LC duration. If the obtained TTC is less than the suggested threshold (2.7 s), the host vehicle must first brake to ensure longitudinal safety.

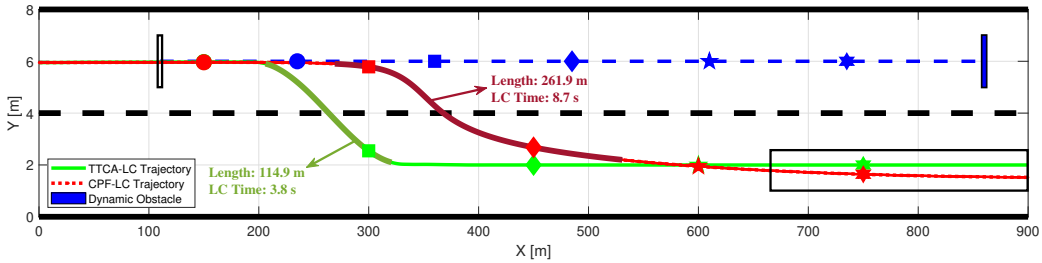


Figure 3.10: Trajectories of the conventional and optimized potential field planners under speeds of 108 km/h.

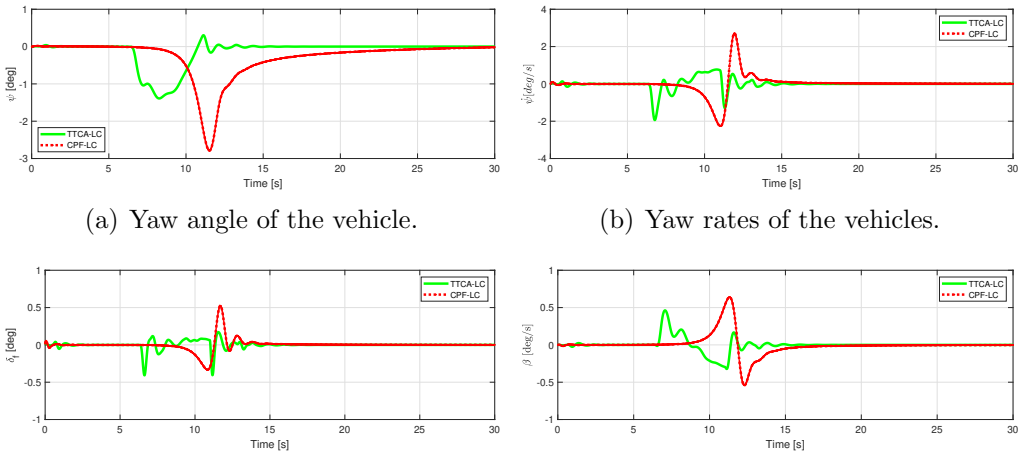
Simulation results and analysis

To compare our proposed TTCA-LC with the conventional PF, we set up a comparative scenario in which we simulated LC behaviors using two AV planning algorithms. The front vehicle was set as a road-bound moving obstacle whose initial parameters were $(120, 6)$ with an initial speed of 90 km/h. The ego vehicle spawned at (0, 6) in the same lane 120 m behind the obstacle vehicle. The initial speed of the ego vehicle was 108 km/h. According to [EHSo11], maintaining vehicle speed during the LC process is suitable for controlling the vehicle dynamics to ensure riding comfort. Therefore, we assumed that the speed of the ego vehicle was fixed during the LC. For comparison, we used the following two planners:

i. Conventional PF-based LC planner (denoted as CPF-LC) [WGL22]

ii. Time-to-collision-aware PF-based LC planner (denoted as TTCA-LC)

As depicted in Fig. 3.10, the blue trajectory shows the position of the dynamic obstacle along the x-y axis. The red and green lines show the trajectories of the ego vehicle using CPF-LC and TTCA-LC methods, respectively. As we can observe, the proposed TTCA-LC method exhibits better performance for different metrics. First, the TTCA-LC path length is reduced from 261.9 m to 114.9 m, which is 147.0 m shorter than that of the CPF-LC. Second, the LC start position of the TTCA-LC method is 63.0 m ahead of the CPF-LC method's position. Third, the LC time of the proposed method is 3.8 s which is closer to human drivers, while the LC time of CPF is 8.7 s. Finally, the trajectory of the CPF-LC deviates from the lane center after the LC, whereas the proposed TTCA-LC method keeps the ego vehicle at the lane center more accurately, as denoted by the black box in the figure.



(a) Yaw angle of the vehicle.

(b) Yaw rates of the vehicles.

(c) Front tire angles of the vehicles.

(d) Sideslip angles of the vehicles.

Figure 3.11: Motion states of the vehicle.

Figs. 3.11(a) and 3.11(b) show the yaw angles and rates of the vehicles. For the yaw angle, the CPF-LC method resulted in a relatively sharp turn of up to 3°, at a rate of 2.7°/s. By contrast, the TTCA-LC method cuts the maximum yaw angle by half, which is less than 1.5° throughout the entire process. Moreover, the yaw rate is also significantly reduced within 2°/s, resulting in the direct flattening of the yaw angle. However, as illustrated in Fig. 3.11(b), the yaw rate of the green solid line forms an oscillation pattern at both the start and end of the LC. Both oscillations were mitigated in under 5 s, and the amplitude is relatively small so that passengers will not feel shaking. Our TTCA-LC method also significantly outperformed the CPF-LC methods in terms of yaw angle.

Fig. 3.11(c) shows the front tire steering angle during the LC maneuver. The CPF-LC and TTCA-LC methods showed relatively similar maximum front tire angles of approximately 0.52 and 0.41°, respectively. According to [LBAT20], this range is within the limits of guaranteeing ride comfort among the LC duration.

Finally, Fig. 3.11(d) shows the statistics for the sideslip angle. In the CPF-LC method, the ego vehicle performed sharp side slips ranging from -0.54° to 0.64°. In contrast, the TTCA-LC method reduced the side slip to a maximum of 0.45° with a slight oscillation. In Fig. 3.12, the curvature of the CPF-LC method reached 0.19° during the LC process. By contrast, the proposed TTCA-LC method reduced the curvature to 0.04°, indicating that the path generated by the TTCA-LC method is smoother than that of the CPF-LC method. From our microscopic analysis, the oscillations were

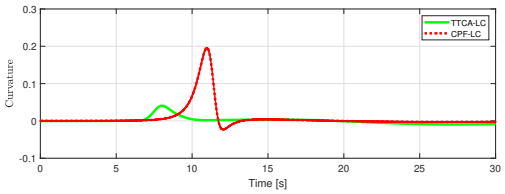


Figure 3.12: Curvature of the trajectories

mainly caused by the constraint imposed by Eq. (8); however, the duration amplitude of the oscillation was relatively short and small. Note that in all four angle charts, the TTCA-LC method produced slight oscillations at the beginning of the maneuvers because the initialization of the steady states of the cubic polynomial was not yet stabilized. Thus, they can be reduced by manually tuning the cubic parameters.

Conclusions

In this subsection, we have introduced a time-to-collision-aware lane-change (TTCA-LC) strategy that uses the PF with an optimized cubic polynomial. Furthermore, we detailed the formulation of the optimization function with reasonable constraints, in which the TTC was utilized to design the constraint for the safety considerations during the LC maneuver. The TTCA-LC method was validated in a comparative driving scenario via MATLAB/Simulink. The simulation results have indicated that the proposed method produces a safer, shorter (27.1% shorten in length), and smoother (56.1% lower in curvature) LC path compared to the CPF-LC strategy, which reserves sufficient space for the braking maneuver if the adjacent obstacle drives abnormally.

3.3.2 Occlusion-aware collision avoidance

Collision avoidance (CA) has always been the foremost task for autonomous vehicles under safety criteria. And path planning is directly responsible for generating a safe path to accomplish CA while satisfying other commands. Due to the real-time computation and simple structure, the PF has emerged as one of the mainstream path-planning algorithms. However, the current PF is primarily simulated in ideal CA scenarios, assuming complete obstacle information while disregarding occlusion issues where obstacles can be partially or entirely hidden from the AV's sensors. During the occlusion period, the occluded obstacles do not possess a PF. Once the occlusion is over, these obstacles can generate an instantaneous virtual force that im-

pacts the ego vehicle. Therefore, we propose an occlusion-aware CA with the responsibility-sensitive safety (RSS)-based PF to tackle the occlusion problem for non-connected autonomous vehicles. We first categorize the detected and occluded obstacles, and then we proceed to the RSS violation check. Finally, we can generate different virtual forces from the PF for occluded and non-occluded obstacles.

Thornton et al. [TLZ+18] presented a modified value-sensitive design method for the AV's speed control to safely navigate an occluded pedestrian crosswalk. The research focused on a low-speed scenario around zebra crossings with a single longitudinal control strategy. Şahin et al. [TS18] proposed a specified motion planning given an uncertain environment model with occlusions. The simulation also concentrated on a T-junction with low-speed consumption and targeted only speed planning. Later, Naumann et al. [NKLS19, NS22] provided safe but not overcautious and continuous-probabilistic motion planning strategies for intersections by considering the occlusion and limited sensor range. Still, the studies only sank into the low-speed scenario with speed generation while ignoring the path. Poncelet et al. [PVBN20], Wang et al. [WGW21], and Hang et al. [HHHL22] all dug into the unsignalized intersections with occlusion concerns and used different planning algorithms to resolve CA, including geometric method, hierarchical framework, and differential game approach. However, they all centered on an extremely low-speed driving scene where the vehicle drives under 10 m/s and discussed less on the path. Recently, Wang et al. [WFZS23] presented an occlusion-aware motion planning scheme that computed a static game tree considering the potential risk probability of the occluded area. However, the research only validated the effectiveness of the proposed method within the vehicle kinematic under low-speed conditions. In the broader context of our study, our research aims to delve deeper into the implications of the occlusion problem on vehicle dynamics within high-speed driving scenarios, explicitly focusing on the utilization of the PF. Therefore, this study introduces a novel occlusion-aware path planning (OAPP) framework (shown in Fig. 3.13) that combines the RSS-based PF to effectively address the challenges posed by the occlusion problem on expressway driving. The contributions of this study are briefly outlined below, as published in [7].

- We differentiate between obstacles perceived in visible and blind (occluded) areas and then utilize the RSS framework to conduct the violation check.
- We regulate the generation of the PF's virtual forces that are also used to produce the speed reference according to the violation check result.

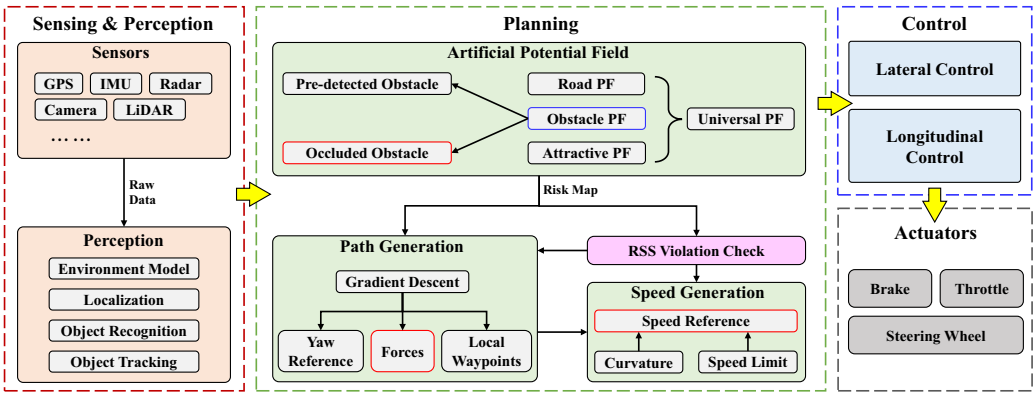


Figure 3.13: Proposed PF-OAPP framework consists of sensing & perception, planning, control and actuators: Planning layer has the PF that can differentiate the visible and occluded obstacles, and then conduct the RSS violation check to adjust the virtual forces and generate the speed reference

Responsibility-sensitive safety

Despite safety assurance being the most crucial task in the research of automatic driving, the ethical issues of autonomous driving also postpone the commercialization of CAVs, e.g., accident liability. In 2017, Mobileye, a subsidiary of Intel, introduced the RSS rules to regulate the driving behaviors of CAVs by defining a set of rigorous mathematical models, interpreting the Duty of Care law [SSSS17]. The RSS is constructed by following the five inductive principles: i. Do not hit someone from behind; ii. Do not cut in recklessly; iii. Right-of-way is given, not taken; iv. Be careful of areas with limited visibility; v. If you can avoid an accident without causing another one, you must do it. Furthermore, NHTSA published a white paper to implement the RSS model into pre-crash scenarios for light vehicles, prompting the safety standardization of autonomous vehicles [SSSS18]. Multiple research institutes have joined and investigated the worldwide standardization of RSS, including the Institute of Electrical and Electronics Engineers (IEEE): Standard 2846 [Soc22], China ITS Industry Alliance, etc.

Since [SSSS17] has clearly described the definitions, we make a supplementary about the minimum safe distances for CAVs by considering the communication delay and the sizes of different vehicles.

Lemma 1 (**Safe Longitudinal Distance**). *Let c_e be the ego vehicle that is behind the front j^{th} obstacle vehicle c_f^j on the X-axis. Let v_e, v_f^j be the longitudinal velocities of the vehicles. Then, the minimum safe distance for*

X-axis between c_e *and* c_f^j *is:*

$$\begin{aligned} D_{rss}^{long,j} =&[v_e(\rho_{rt}+\rho_{cd})+\frac{1}{2}a_{accel}^{max}(\rho_{rt}+\rho_{cd})^2+\frac{l_e+l_f^j}{2}+ \\ &\frac{(v_e+a_{accel}^{max}(\rho_{rt}+\rho_{cd}))^2}{2a_{brake}^{min}}-\frac{v_f^{j\,2}}{2a_{brake}^{max,j}}]_+, \end{aligned} \tag{3.11}$$

where $[h]_+ : \max\{h, 0\}$

with ρ_{rt} is the reaction time of the ego vehicle in sensing the emergency and ρ_{cd} is the communication delay between CAVs; a_{accel}^{max} and a_{brake}^{min} denote the maximum acceleration and the minimum braking of the ego vehicle; $a_{brake}^{max,j}$ is the maximum braking of the j^{th} obstacle vehicle; l_e denotes the length of the ego vehicle and l_f^j is the length of the j^{th} obstacle vehicle. Regarding the reaction time for autonomous vehicles, [DCN16] investigated the recent traffic data released from the California trials, which is approximately 0.83 seconds on average. In this study, we assume there has no packet loss during the transmission. The communication delay between CAVs is assumed to be around 0.5 ms that is estimated from the real testing data [CYHZ20]. On the other hand, we have the following proposition for calculating the minimum safe distance for Y-axis.

Lemma 2 (**Safe Lateral Distance**). *Without loss of generality, assume that the ego vehicle* c_e *is to the left of the* j^{th} *obstacle vehicle* c_o^j*. Define* $v_{e,\rho}^{lat} = v_e^{lat} + a_{accel}^{lat,max}(\rho_{rt}+\rho_{cd})$ *and* $v_{o,\rho}^{lat,j} = v_o^{lat,j} - a_{accel}^{lat,max,j}(\rho_{rt}+\rho_{cd})$*. Then, the minimum safe distance for Y-axis is:*

$$\begin{aligned} D_{rss}^{lat,j} =&\mu+\Bigg[\frac{v_e^{lat}+v_{e,\rho}^{lat}}{2}(\rho_{rt}+\rho_{cd})+\frac{v_{e,\rho}^{lat\,2}}{2a_{brake}^{lat,min}}+\frac{l_w+l_w^j}{2} \\ &-\left(\frac{v_o^{lat,j}+v_{o,\rho}^{lat,j}}{2}(\rho_{rt}+\rho_{cd})+\frac{v_{o,\rho}^{lat,j\,2}}{2a_{brake}^{lat,min,j}}\right)\Bigg]_+, \end{aligned} \tag{3.12}$$

where *lat* denotes the vehicle motions in Y-axis and μ determines the fluctuation margin; l_w^j represents the length of the j^{th} obstacle vehicle. Eq. 3.11 and 3.12 indicate that the minimum safe distances of the RSS consider the worst-case collision by assuming the ego vehicle will keep accelerating at a_{accel}^{max} during the time interval $[0, \rho_{rt}+\rho_{cd}]$, and then braking at least a_{brake}^{min} until reaching a full stop. Meanwhile, the front obstacle vehicle will brake at a_{brake}^{max} while the lateral obstacle vehicle will have the same behaviors as the ego vehicle.

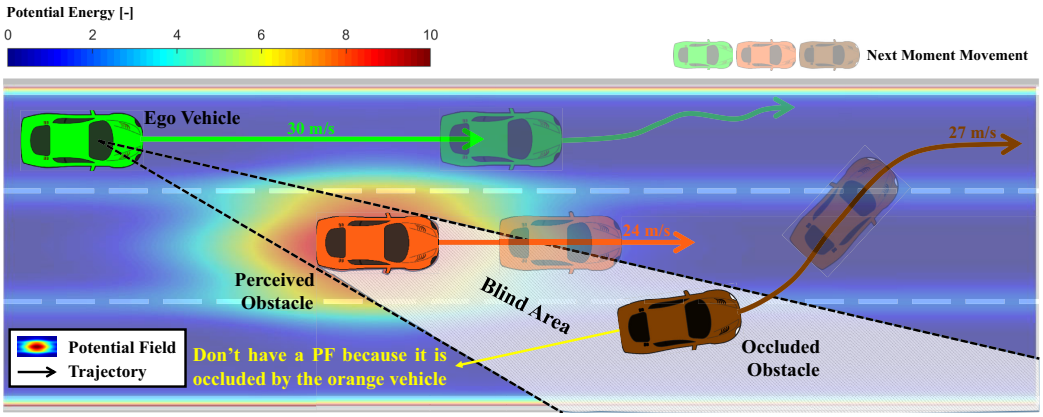
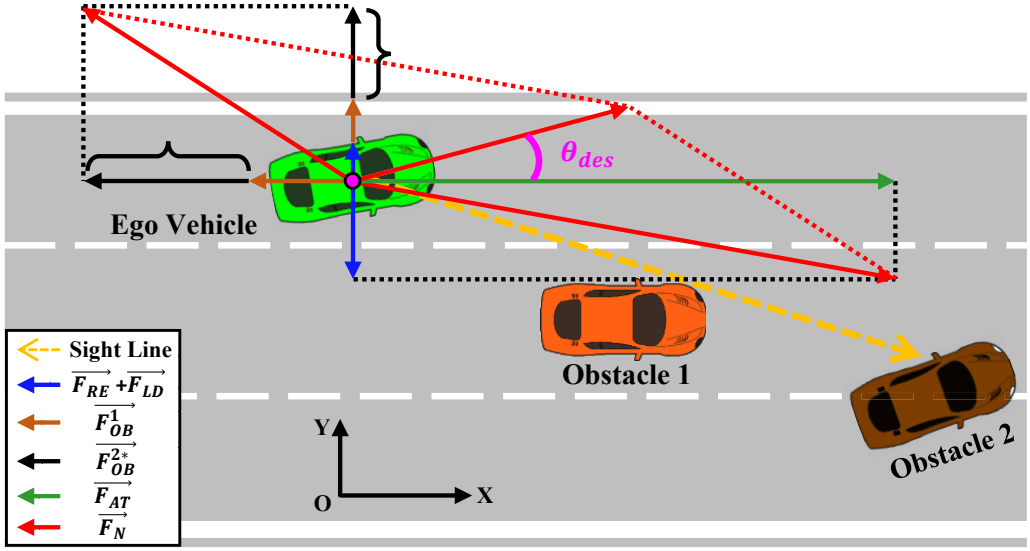


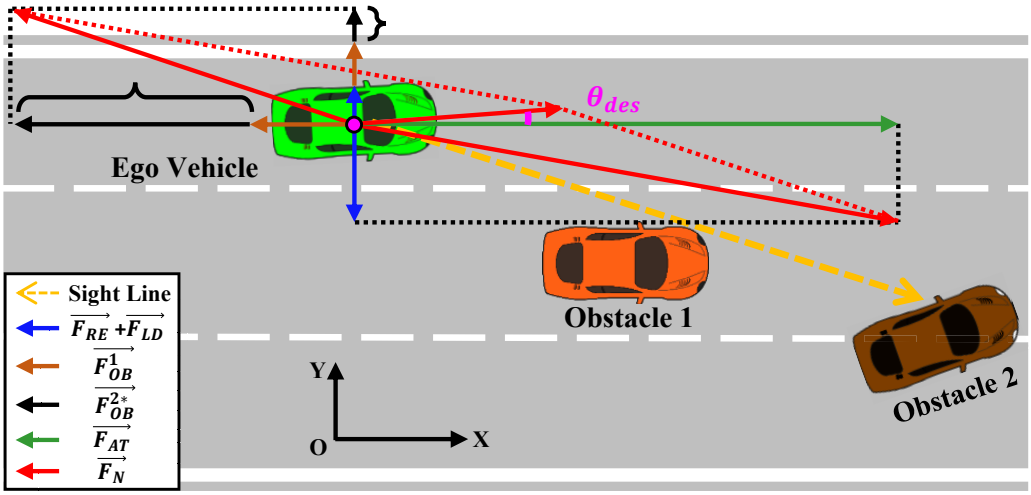
Figure 3.14: Occlusion problem: the brown vehicle is occluded by the orange vehicle from the view of the green vehicle, which the brown vehicle does not have a PF; the next moment movements of the autonomous vehicles indicate the invisible driving maneuvers of the brown vehicle can impact the green vehicle's local path

Occlusion problem

The scenario illustrated in Fig. 3.14 portrays a situation on the expressway involving three vehicles operating independently at varying speeds. Within this visual representation, the ego vehicle (depicted in green) is observed to occupy the first lane. In contrast, the other two vehicles, driven by human drivers (shown in orange and brown), are positioned in the second and third lanes, respectively. It is important to highlight that the occlusion phenomenon occurs when the orange vehicle obstructs the brown vehicle, resulting in the brown vehicle becoming invisible from the viewpoint of the ego vehicle. This occlusion occurs within a designated blind area, distinctly marked as a shaded region in Fig. 3.14. Hence, the driving behaviors of the brown vehicle remain completely undetectable by the sensors of the ego vehicle, resulting in the absence of any established PF between them. Suppose, at the next moment, the brown vehicle initiates an abrupt and continuous two-lane lane change maneuver. In such a scenario, the ego vehicle detects the presence of the brown vehicle and promptly establishes a PF in response. However, as a consequence of the abrupt detection of the obstacle, the PF that arises between the ego vehicle and the brown vehicle can give rise to an excessive virtual repulsive force exerted on the ego vehicle. This force, depicted in Figure 3.15(a), induces an immediate oscillatory impact on the ego vehicle, further amplifying the inherent instability in its motion.



(a) Conventional PF method



(b) Proposed PF-OAPP method

Figure 3.15: Synthesis and decomposition of virtual forces when seeing the occluded obstacle 2 from two approaches

To tackle the aforementioned problem, our proposed solution involves a series of steps. Firstly, we implement a labeling process to differentiate between obstacles originating from visible areas and those from blind areas. Specifically, for occluded obstacles, we utilize the principles of RSS to perform a violation check precisely at the moment they are perceived. In order to quantify the relative distance between the ego vehicle and the occluded vehicles, we introduce the variables D^x_{rela} and D^y_{rela}, representing the longitudinal and lateral distances, respectively. Drawing from the guidelines outlined in the Saskatchewan Driver's Handbook [oC21], recommended maneuvers for emergency driving consist of a two-step approach. The initial step involves applying brakes to ensure longitudinal safety, followed by steering actions to avoid a collision on the expressway effectively. Therefore, to align our calculations with the RSS regulations and the suggested appropriate responses, we introduce the following adjustments to determine the virtual forces accurately.

$$\overrightarrow{F^x_N} = -(\frac{\partial U_{AT}}{\partial X} + \frac{\partial U_{RE}}{\partial X} + \frac{\partial U_{LD}}{\partial X} + \frac{\partial U^j_{OB}}{\partial X} + \alpha_1 \frac{\partial U^h_{OB}}{\partial X}), \tag{3.13}$$

$$\overrightarrow{F^y_N} = -(\frac{\partial U_{AT}}{\partial Y} + \frac{\partial U_{RE}}{\partial Y} + \frac{\partial U_{LD}}{\partial Y} + \frac{\partial U^j_{OB}}{\partial Y} + \alpha_2 \frac{\partial U^h_{OB}}{\partial Y}), \tag{3.14}$$

where

$$\alpha_1 = \begin{cases} 1 - \frac{\pi}{2} \arctan \frac{D^x_{rela} - \sigma^h_x}{\sigma^h_x} & \text{if } D^x_{rela} \geq \sigma^h_x \\ 1 + \frac{\pi}{2} \arctan \frac{\sigma^h_x - D^x_{rela}}{\sigma^h_x} & \text{if } D^x_{rela} < \sigma^h_x \end{cases}$$

$$\alpha_2 = \begin{cases} 1 - \frac{\pi}{2} \arctan \frac{D^y_{rela} - \sigma^h_y}{\sigma^h_y} & \text{if } D^y_{rela} \geq \sigma^h_y \\ \frac{\pi}{2} \arctan \frac{\sigma^h_y - D^y_{rela}}{\sigma^h_y} & \text{if } D^y_{rela} < \sigma^h_y \end{cases}$$

with U^h_{OB} denotes the h^{th} occluded obstacle that we mark from the blind area. $\alpha_{1,2}$ are the proportional coefficients based on the RSS safe distances with the normalization of the arctangent function. Therefore, we can mitigate the instant lateral oscillation or sway by using Eq. (7)-(8) to adjust the virtual forces while conforming to the safety criteria. Consequently, we can decrease the lateral virtual forces while increasing the longitudinal virtual forces when computing the PF for the occluded obstacle, as illustrated in Fig. 3.15(b). Next, we use the adjusted forces to generate the longitudinal speed reference.

$$\overrightarrow{F^x_N} - \overrightarrow{F_C} = M_v a_{des}, \tag{3.15}$$

where $\overrightarrow{F_C}$ is the virtual criterion force that we can get when the ego vehicle drives at a constant speed without obstacles. M_v is the virtual mass, and

a_{des} is the desired acceleration. Besides, we should also consider the speed limit on the expressway and the maximum speed for curved paths with the conformation of vehicle dynamics when calculating the reference speed V^* for the controller.

$$V^* = \min(V_{max}, V_{des}), \tag{3.16}$$

where

$$V_{max} = \min(V_{limit}, \max(0, \sqrt{\frac{\mu g}{\kappa}})),$$
$$V_{des} = V_{cur} + a_{des}T,$$

with V_{limit} represents the limit speed on the expressway and μ is the frictional coefficient. g means the gravitational acceleration and V_{cur} denotes the current longitudinal speed of the ego vehicle. T refers to the sampling time.

Simulation results and analysis

we simulated an occlusion scenario on the expressway to inspect the proposed method via MATLAB/Simulink. Particularly, we have made an occlusion check that can output an occlusion flag, as shown in Fig. 3.19(b). As described in Fig. 3.14, We first make two extended lines from the ego vehicle, and the extended lines will go through the edge corners of the orange vehicle. Then, we can use two linear equations to represent the two extended lines. Therefore, the occlusion check can be simplified to check the relative positions between the brown vehicle and two linear equations.

The basic settings of the occlusion scenario are also illustrated in Fig. 3.14. The ego vehicle is driving from an initial position of (0, 10) on the first lane, maintaining a speed of 30 m/s. Meanwhile, the orange vehicle is moving forward at a speed of 26 m/s, starting from an initial position on the middle lane at (6, 80). Additionally, the brown vehicle is shifting at a speed of 27 m/s on the third lane, located at position (2, 115).

In the simulation study, we have conducted three comparative path planners to illustrate the performance of the proposed method: (i) PF-based path planner with constant speed (PF-CS) [LYQC22]; (ii) PF-based path planner with speed planning (PF-SP) [WGL22]; (iii) Proposed PF-based occlusion-aware path planner (PF-OAPP).

As shown in Fig. 3.16, we can observe that both the paths of PF-CS (denoted as a red solid line) and PF-SP (denoted as a purple dotted line) have obvious lateral deviations, reaching maximum values of 11.46 m and 11.07 m, respectively. Besides, we discover that the PF-CS path planner

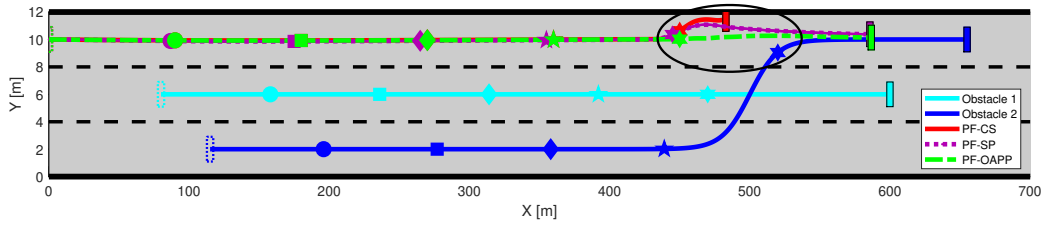
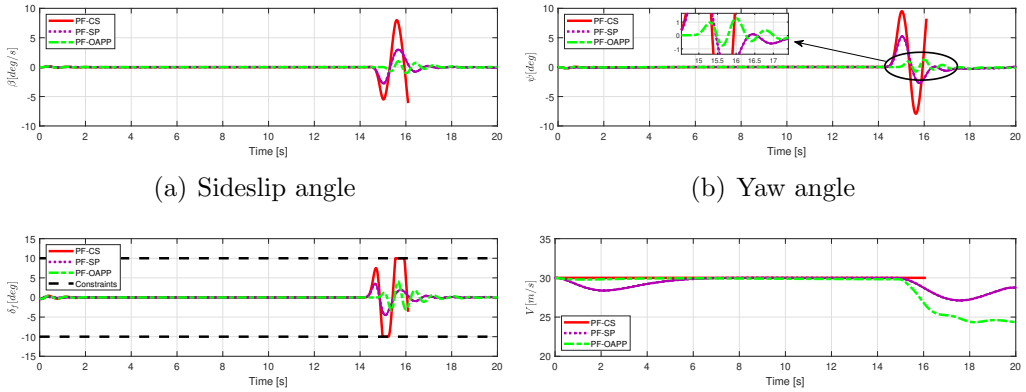


Figure 3.16: Trajectories of the CPF-based and OPF-based planners under the speed of 108 km/h



(a) Sideslip angle

(b) Yaw angle

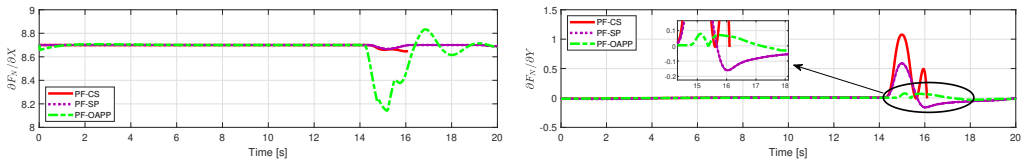
(c) Front tire steering angle

(d) Longitudinal speed

Figure 3.17: Motion states of the obstacle vehicle based on PF-CS, PF-SP, and PF-OAPP, respectively

stops the computation due to the trap to a local minimum. Conversely, the path of PF-OAPP (denoted as a green chain line) has no such lateral deviation, maintaining a stable driving status. But we can see that the path's length of PF-OAPP is shorter than that of PF-SP due to the greater deceleration, as depicted in Fig. 3.17(d). The longitudinal speed of PF-CS decreases to 27.12 m/s while that of PF-OAPP reduces to 23.45 m/s. In addition, it should be noted that all the decelerated reactions appear after the brown vehicle is sensed at the time of $T = 13.96$ s, where the occlusion flag changes from 1 to 0.

On the other hand, the motion states of the vehicles from different path planners are described in Fig. 3.17. In Fig. 3.17(a), we can find that the sideslip angle of PF-CS has a conspicuous oscillation from $T = 14.62$ s with a maximum value of 7.99 °/s. While the sideslip angle of PF-SP is smaller but still reaches a maximum value of 2.98 °/s. On the contrary, the sideslip



(a) Longitudinal virtual force (b) Lateral virtual force

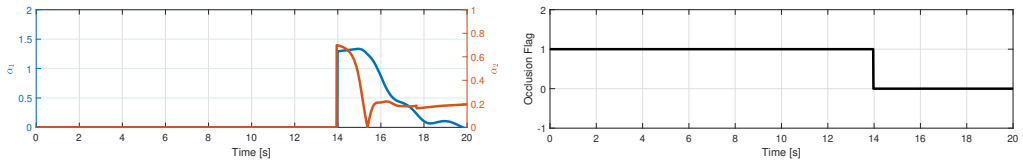
Figure 3.18: Virtual forces from PF-CS, PF-SP, and PF-OAPP, respectively

angle of PF-OAPP varies around zero, which indicates that there has been no significant sideslip occurring on the vehicle body. Similarly, we can observe the same phenomenon in the yaw angle that is depicted in Fig. 3.17(b). The yaw angle of PF-CS exceeds 9° and has a short vibration from $T = 14.28$ s to $T = 16.11$ s while that of the PF-SP reaches 5.23° with less vibration. The yaw angle of PF-OAPP has a minimal change within 0.5°, and no oscillations are found. Next, the front tire steering angle of the vehicle is presented in Fig. 3.17(c) with a hard constraint of ±10°. We can see that the front tire steering angle of PF-CS reaches the constraint and oscillates between the hard bounds, while that of PF-SP has a negative maximum value of -4.51° and an attenuated oscillation from $T = 14.28$ s to $T = 17.50$ s. On the opposite, the front tire steering angle of PF-OAPP has a slight variation between 0.25° and -1.00°.

Finally, the longitudinal and lateral virtual forces calculated from the three path planners are plotted in Fig. 3.18. In Fig. 3.18(a), we can see that the longitudinal virtual force of PF-OAPP starts to fall until reaching 8.14, while those of the other two planners have a slight change from 8.70 to 8.65 after the occlusion flag changes. From Fig. 3.18(b), we can observe that PF-CS produces a more significant lateral virtual force, reaching a maximum of 1.08. At the same time, PF-SP also generates a lateral virtual force of 0.59. However, the lateral virtual force of PF-OAPP varies around zero from 0.05 to -0.02. Furthermore, the proportional coefficients $\alpha_{1,2}$ of the PF-OAPP method are presented in Fig. 3.19(a). We can see that α_1 exceeds 1 (reaches 1.33) and α_2 is below 0.5 (around 0.4) when the occlusion flag changes from 1 to 0, which indicates that the PF-OAPP will produce a greater longitudinal virtual force and a smaller lateral virtual force than the current PF's values.

Conclusions

We have introduced a unique occlusion-aware path planning with the PF, tackling the occlusion problem on the expressway. We have found that the



(a) α_1 and α_2 from PF-OAPP

(b) Occlusion flag: 1 means the occlusion appears; 0 means the occlusion disappears

Figure 3.19: Analysis of α_1, α_2 and Occlusion flag in PF-OAPP.

occluded obstacle from the blind area will impose an unexpected virtual force from the PF modeling that can make the ego vehicle have a lateral sway. Therefore, we labeled the obstacle detected from the blind area and then used responsibility-sensitive safety to check the safety situation. After that, we can recompute the virtual forces based on the violation check. The simulation results have verified the effectiveness of the proposed PF-OAPP method compared to other PF methods in terms of eliminating lateral oscillation and generating a smoother path.

3.3.3 Clothoid Curve-based emergency stopping

While the PF effectively enforces a rigid road boundary to keep the vehicle within the confines of the road, it will lead to the "blind alley" problem caused by local minima in specific high-speed scenarios, making the vehicle indecision or erratic behavior, or even accidents. Therefore, the objective of this research is to foresee and tackle the problem above to avoid a potential collision in advance. We also find that existing methods do not provide a root cause analysis and effective solutions for this problem, which limits the practicality of the PF in handling complicated traffic situations. In this paper, we propose an Emergency-Stopping Path Planning (ESPP), described in [3], that incorporates an adaptive PF with the clothoid curve. First, we design an emergency triggering estimation to detect the "blind alley" problem. Second, we regionalize the driving scene to search the optimal breach point on the road PF and the final stopping point for the vehicle by considering the motion range of the obstacle. Finally, we use the optimized clothoid curve to fit these calculated points under vehicle dynamics constraints to generate a smooth emergency avoidance path. The previous related works generally build the road potential field assigned with an immense potential energy value, making the road boundaries/edges impenetrable or impassable. It implicitly assumes that all the collisions can be avoided within the confine of the road. However, in real-world driving scenes, there must be situations

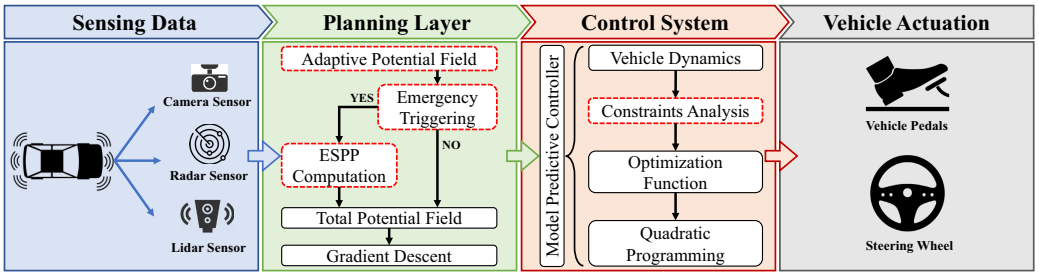


Figure 3.20: Overall autonomous driving system framework with the embedded ESPP method: Sensing data gathers the information collected by sensors; Planning layer monitors the emergency and triggers the ESPP computation if the emergency is sensed; Control system outputs the direct signals to Vehicle Actuators for longitudinal and lateral maneuvers

where the vehicle needs to partially or entirely drive off the road for emergency collision avoidance. Previous works did not address the "blind alley" problem in high-speed scenes where the adjacent vehicle suddenly changes lanes without a pre-warning. Therefore, this paper provides a root cause analysis and a feasible solution for the problem, enabling the PF to handle such hazardous situations effectively. The contributions of this subsection are briefly summarized as follows:

- We introduced a clothoid curve to design the ESPP; the clothoidal coefficients are obtained by solving a constrained quadratic programming (QP) problem.
- We propose to open a breach on the road PF based on the local reference waypoints, which can navigate the vehicle for a safe stopping maneuver on the roadside.
- We computed the terminal side of the ESPP by considering the road structure and the predicted motion range of the obstacle.

The proposed ESPP method is embedded mainly in the planning module, including the APF, emergency triggering, and ESPP computation, as shown in Fig. 3.20 (red dotted frames). The complete autonomous driving system framework includes the Sensing, Planning, Control, and Vehicle Actuation.

Adaptive obstacle potential field

To more accurately describe the steering behavior of the obstacle vehicle, we can use the probability density function (PDF) of the Gaussian distribution

to model the obstacle PF U [LLY+20]:

$$U_{obs} = \frac{A_{obs}}{2\pi\sqrt{|\Sigma|}} e^{\left(-\frac{1}{2}(\ell-\mu)^T\Sigma^{-1}(\ell-\mu)\right)}, \tag{3.17}$$

where A_{obs} is the maximum amplitude of the obstacle PF, $\ell = (s,\ d)^T$ is the position of the ego vehicle in the Frenet frame [WZKT10] that s and d are the tangential and normal directions in the Frenet coordinate, and Σ and μ are the covariance matrix and mean of the PDF, respectively. Therefore, we use Eq. (3.17) to adapt the motion of the obstacle along with the longitudinal and lateral directions U_{Aobs} as follows:

$$U_{Aobs} = \sum_{j=1}^{N_{obs}} w_1 U^1_{obs,j} + w_2 U^2_{obs,j}, \tag{3.18}$$

where

$$\begin{aligned} &w_1 \in [0.5, 1], \qquad w_2 = 1 - w_1, \\ &\mu_1 = (s_1, d_1)^T, \quad \Sigma_1 = \begin{bmatrix} \sigma^2_{s_1} & 0 \\ 0 & \sigma^2_{d_1} \end{bmatrix}, \\ &\mu_2 = (s_2, d_2)^T, \quad \Sigma_2 = \begin{bmatrix} \sigma^2_{s_2} & 0 \\ 0 & \sigma^2_{d_2} \end{bmatrix}, \end{aligned}$$

where N_{obs} denotes the number of obstacle vehicles, $w_{1,2}$ is the weight factor, μ_1 and μ_2 denote the mean of the corresponding PDF that is related to obtaining the safe distance from the position of the obstacle in the Frenet frame, Σ_1 and Σ_2 represent the covariance matrix of the corresponding PDF, and $\sigma_{s,d}$ denotes the variance terms of the corresponding covariance matrix, which is combined with the longitudinal and lateral accelerations of the obstacle. The obstacle PF is shown in Fig. 3.21.

Blind alley problem

Although the PF from Eq. (3.18) can model the collision risk with high accuracy by considering the longitudinal and lateral accelerations of the obstacle, it ignores the local minima problem with the assumption that the motion of the obstacle PF is known. However, traffic emergencies mostly occur because of the unpredictable motions of the surrounding obstacles, such as sudden deceleration and reckless lane changes [PRMS95]. As shown in 3.21, the sudden lane-changing obstacle with a full braking maneuver will lead to a rapidly expanding obstacle PF, which intersects with the road PF.

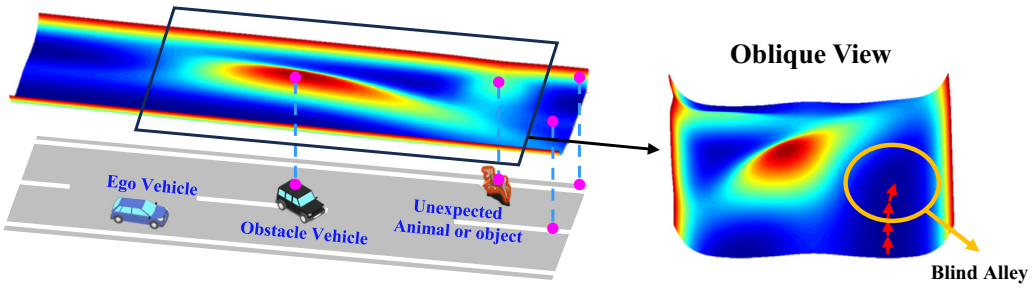


Figure 3.21: Emergency merging behavior of the adjacent vehicle (black) owing to the unexpected animal (brown): From the oblique view, the obstacle PF intersects with lower road PF, leading to a blind alley (local minima)

Subsequently, the "blind alley" phenomenon occurs because there are no feasible paths for the ego vehicle to track. This is a case of local minima. As described by Koren and Borenstein [KB91], the local minima problem causes a trap situation for a mobile robot. However, considering the dynamic characteristics of the ego vehicle, it is difficult to stop at the local minima region owing to the large inertia. Instead, the ego vehicle could have driven into either the obstacle PF or road PF and received an excessive repulsive force, which can cause severe yawing and even vehicle crashes. A simple way is to directly remove the road PF (the side to which the vehicle is heading) so that the ego vehicle can drive out of the road to obtain sufficient space for emergency braking and obstacle avoidance. However, the ego vehicle is prone to wheel slipping during emergency obstacle avoidance after removing the road PF due to the instantaneous disappearance of the road repulsive force. There is an imbalance in the virtual forces, leading to oversized repulsion from the obstacle PF experienced by the vehicle. In severe cases, they could lose control of the vehicle body. Although removing the road PF can eliminate the "blind alley" problem, it will lead to an imbalance of virtual forces because the repulsive force of the road PF disappears instantly, and the excessive repulsive force of the obstacle PF causes slipping. Therefore, we proposed a triggering estimation to detect the "blind alley" problem and then generate an emergency-stopping path based on the clothoid curve for completing a safe stop.

Emergency triggering estimation

As described in Eq. (2.12), the APF can obtain ψ_{ref} at each time step, which we can use to estimate the emergency. Firstly, we use ψ_{ref} to generate the

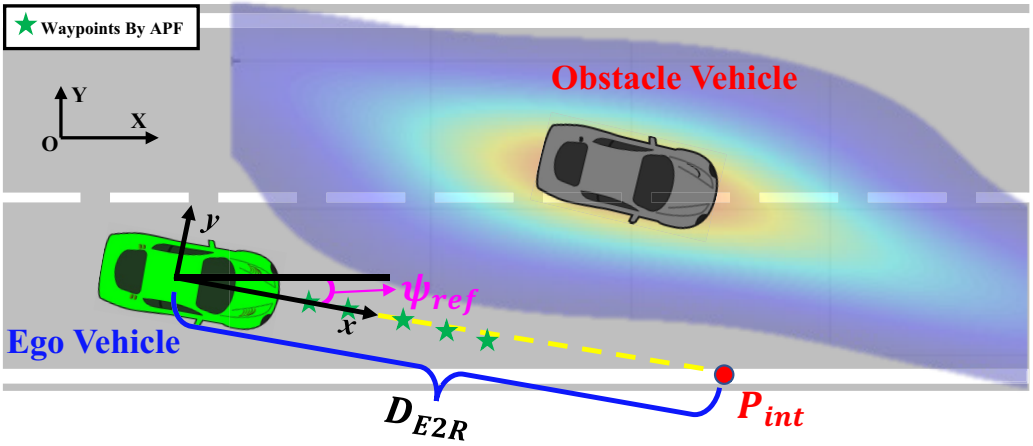


Figure 3.22: Explanation of the emergency triggering estimation: With ψ_{ref} given by APF, making an extension line from the current position of ego-vehicle (green) to intersect with the lower road boundary P_{int}; D_{E2R} is the distance between the green vehicle and P_{int}

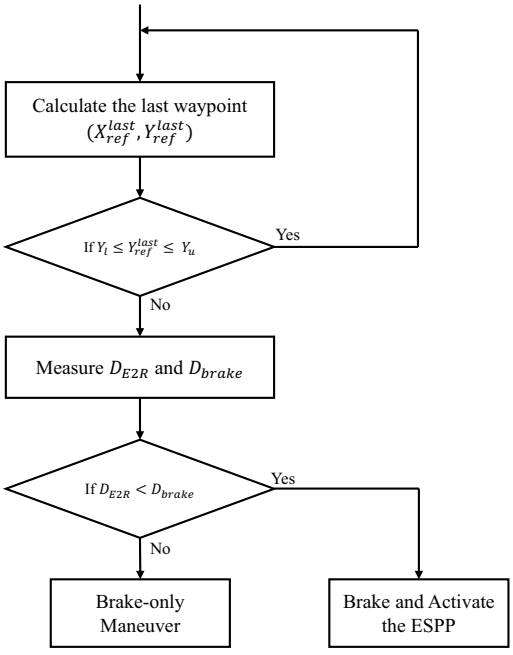


Figure 3.23: System flow chart of the proposed emergency triggering estimation

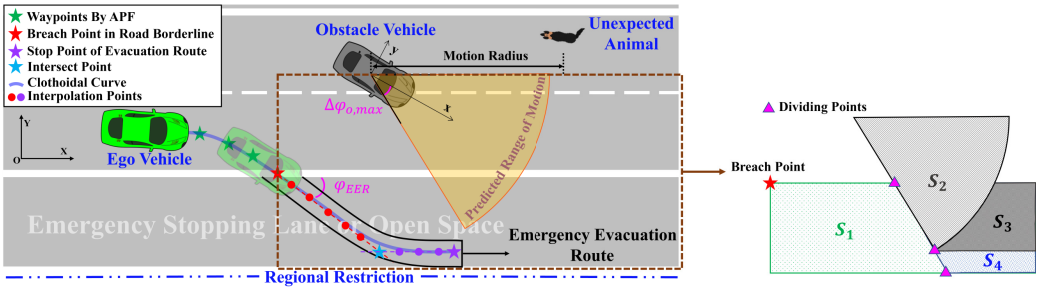


Figure 3.24: Emergency-Stopping Path Planning on the expressway: Regionalization within the brown dashed box (S_1, S_2, S_3, S_4); three star-shape points are then obtained (red, blue, purple); interpolation points (circle) are used for computing the clothoid curve (light blue).

local reference waypoints (X_{ref}, Y_{ref}) for the controller to track, which is computed with a given step length L. Note that Eq. (2.13) is iterated in a control loop according to the number of required waypoints, and L is usually dependent on the current speed and sampling time. Then, as depicted in Fig. 3.22, the green star-shape waypoints are produced by APF, which we can monitor the last waypoint (X_{ref}^{last}, Y_{ref}^{last}), whether it reaches or cross the road edge at each time step. If yes, we can make an extension line along the ψ_{ref} (if $\psi_{ref} \neq 0$) angle from the current position of the ego-vehicle, as stated in Fig. 3.22. And the extension line will have an intersect point (denoted as P_{int}) with the lower road boundary. Second, we can measure the distance D_{E2R} from the current position of the ego-vehicle to the intersect point. We mark the minimum braking distance of the ego-vehicle from the current position as D_{brake}. It should note that D_{brake} depends on multiple factors, including the reaction time, braking deceleration, road conditions, etc. D. Lyubenov [Lyu11] has summarized the empirical formula to compute the minimum braking distance in accident investigation the cases for emergency braking behavior. If D_{E2R} is greater than or equal to D_{brake}, the ego vehicle can promptly stop before reaching the road PF. In this case, the ESPP computation will not be triggered, and the ego vehicle can regain its orientation to follow the obstacle vehicle if the obstacle vehicle returns to regular driving after an emergency lane change. Otherwise, the ESPP computation will be triggered to navigate the ego-vehicle to a safe stop. In general, the overall process of the emergency triggering estimation is summarized in Fig. 3.23.

Emergency stopping maneuver

As depicted in Fig. 3.24, when the adjacent vehicle suddenly merges without a pre-warning, the waypoints produced by the APF from the ego vehicle will lead to the lower road borderline. In this situation, the ego vehicle hits the PF of the lower road boundary, even with complete braking. An excessive repulsive force is imposed on the ego vehicle because the road PF restricts the vehicles from driving out of the road, leading to a severe heading oscillation of the ego vehicle. Herein, opening a breach from the road PF is necessary to navigate the ego vehicle to stop at a non-conflicting position. From the waypoints (green stars) generated by the APF, we can estimate the heading angle of the ego vehicle when it drives toward the road boundary. The estimated heading angle is then used to find the waypoint (red star) intersecting the road boundary as the breach spot. Subsequently, the most crucial step is to determine the stop point (purple star). Thus far, the selection of the stop point should consider the following constraints:

- The stop point should not be within the predicted motion range of the obstacle.
- The stop point should not be in the restricted region (denoted as the blue double-dotted line).
- The total length of the ESPP should consider the distance and time from braking to a safe stop.

Based on these requirements, we can regionalize the selected area (denoted by the brown dashed frame in Fig. 3.24) by two-dimensional geometry. The predicted motion range of the obstacle vehicle is denoted by S_2 as follows:

$$S_2 = \frac{1}{2}\alpha R^2, \tag{3.19}$$

where

$$\alpha = 2\Delta\psi_{o,max}, \quad R = N_p V_{obs} T_s,$$

where α is the central angle and R is the motion radius of the obstacle vehicle. $\Delta\psi_{o,max}$ denotes the maximum heading angle of the obstacle vehicle and V_{obs} is the velocity of the obstacle vehicle. N_p denotes the prediction horizon (consistent with the MPC controller), and T_s denotes the sampling time. In this study, we use approximate estimation to predict the motion range of the obstacle vehicle. At each time step, the ego vehicle measures $\Delta\psi_{o,max}$ and V_{obs} that we can roughly estimate the possible motion range considering the maximum mechanical steering limitation. Then, we can then calculate the coordinates of the three dividing points (denoted as P^1_{dp}, P^2_{dp}, and P^3_{dp}, from top to bottom) using the geometric solution. Therefore, we should assign

Algorithm 1 Selecting Stop Point of the ESPP

Initialization:$P_{bp}, P_{sp}, D_{manha} \leftarrow \mathbf{0}$
Compute $P_{sp} \leftarrow \{x_{sp}, y_{sp}\}$
Compute S_2 based on Eq. (3.19)
for $x_{sp,cand} \in [x_{bp}, x_{bp} + D_{brake}]$ **do**
  for $y_{sp,cand} \in [Y_l, Y_{esl} - l_w/2]$ **do**
    if $\psi_o \leq 0$ **then**
      Obtain $P^i_{dp} \leftarrow \{x^i_{dp}, y^i_{dp}\}$
      Optimize D_{manha} Eq. (3.20) for P^*_{sp}
    else
      Optimize D_{manha} Eq. (3.20), without Eq. (13a) and (13b) for P^*_{sp},
    end if
  end for
end for

Output: selected stop point P^*_{sp}

the stop point (denoted as P_{sp}) outside S_2 and S_3, because the collision risk is higher than S_1 and S_4. Moreover, if P_{sp} is located in S_3, it leads to a tortuous curve. Therefore, we hope that P_{sp} can be selected from S_1, which is the safest area. Nevertheless, if the length of the ESPP is less than the minimum braking distance of the ego vehicle, S_4 should be considered for P_{sp}. Finally, we can arrange it into an optimization problem with the following constraints:

$$\max_{x_{sp}, y_{sp}} |x_{sp} - x_{bp}| + |y_{sp} - y_{bp}| \tag{3.20}$$

$$\text{s.t.} - \psi_{ESPP} < \arctan\left(\frac{y_{sp} - y_{bp}}{x_{sp} - x_{bp}}\right) < 0 \quad , \tag{3.20a}$$

$$\begin{cases} P_{sp} = \{x_{sp}, y_{sp}\} \in S_1, & if \quad L_{ESPP} \geq D_{brake}, \\ P_{sp} = \{x_{sp}, y_{sp}\} \in S_4, & if \quad L_{ESPP} < D_{brake}, \end{cases} \tag{3.20b}$$

where ψ_{ESPP} denotes the heading angle of the ESPP, L_{ESPP} denotes the length of the ESPP, and D_{brake} denotes the minimum braking distance. The objective of Eq. (3.20) is to maximize the Manhattan distance between P_{sp} and the breach point, P_{bp}, because we need to stop as far as possible, considering that the car needs a sufficient distance to brake and also needs to be as far away from dangerous areas as possible. Therefore, we have specified the safe zone (S_1 and S_4) in the constraints (14a) and (14b) with regionalization. By solving the above constrained objective function, we can get the optimal point for P_{sp}. The detailed procedure for selecting P_{sp} is presented in Algorithm 1. Y_{esl} refers to the lower boundary of the emergency stopping lane,

and l_w is the vehicle's width. Provided that if we determine P_{bp} and P_{sp}, we can compute an intersection point, P_{ip}, using two line segments extending from points P_{bp} and P_{sp}. The tilt angle of the line segment extending from P_{bp} is equal to the heading angle of the ego vehicle. By doing this, we can ensure that the ego vehicle will not have serious fluctuations in heading when entering the ESPP. Moreover, the line segment from P_{sp} should be parallel to the road direction, which conforms to traffic rules when using the emergency stopping lane (ESL). Therefore, we can interpolate certain waypoints (red and purple dots) between the two line segments for curve fitting. We subsequently re-formulate Eq. (3.6) through the waypoints belonging to three categories: APF, the first line segment (red dotted line), and the second line segment (purple dotted line).

$$\underbrace{\begin{bmatrix} 1 & x_{1,apf} & x_{1,apf}^2 & x_{1,apf}^3 \\ 1 & x_{2,apf} & x_{2,apf}^2 & x_{2,apf}^3 \\ \vdots & \vdots & \vdots & \vdots \\ 1 & x_{M-1,bp} & x_{M-1,bp}^2 & x_{M-1,bp}^3 \\ 1 & x_{M,bp} & x_{M,bp}^2 & x_{M,bp}^3 \\ \vdots & \vdots & \vdots & \vdots \\ 1 & x_{N-2,ip} & x_{N-2,ip}^2 & x_{N-2,ip}^3 \\ 1 & x_{N-1,ip} & x_{N-1,ip}^2 & x_{N-1,ip}^3 \\ 1 & x_{sp} & x_{sp}^2 & x_{sp}^3 \end{bmatrix}}_{\mathbf{X}} \underbrace{\begin{bmatrix} c_0 \\ c_1 \\ c_2 \\ c_3 \end{bmatrix}}_{\mathbf{C}_v} = \underbrace{\begin{bmatrix} f(x_{1,apf}) \\ f(x_{2,apf}) \\ \vdots \\ f(x_{M-1,sp}) \\ f(x_{M,sp}) \\ \vdots \\ f(x_{N-2,ip}) \\ f(x_{N-1,ip}) \\ fx_{sp}) \end{bmatrix}}_{\mathbf{F}} \tag{3.21}$$

where $P_{apf} = (x_{apf},\ f(x_{apf}))$ is the position pair of the waypoints from the APF, $P_{bp} = (x_{bp},\ f(x_{bp}))$ denotes the position pair of the breach points, $P_{ip} = (x_{ip},\ f(x_{ip}))$ represents the position pair of the intersection points, and $P_{sp} = (x_{sp},\ f(x_{sp}))$ is the position pair of the stop point. Subsequently, we can obtain the clothoidal coefficients through the method of least-squares. Considering that the least square method cannot make the curve pass through all the selected waypoints accurately, it might lead to low accuracy at the end of the curve. Therefore, we introduce a weight matrix W into Eq. (3.21), as follows:

$$W\mathbf{X}\mathbf{C}_v = W\mathbf{F}, \tag{3.22}$$

where

$$W = diag(w_1, w_2,\ \ldots, w_N)_{N\times N}.$$

Thus, the fitting accuracy at the end of the curve can be improved by adjusting the weight matrix to stop the ego vehicle at the desired location.

Subsequently, the clothoidal coefficients are obtained as follows:

$$\mathbf{C}_v = ((W\mathbf{X})^T W\mathbf{X})^{-1}(W\mathbf{X})^T W\mathbf{F}. \tag{3.23}$$

Eq. (3.23) still does not consider vehicle dynamics; thus, it cannot ensure that the path is always trackable for the ego vehicle, particularly with different dynamic characteristics [KLC17]. To overcome this, we reformulate Eq. (3.23) to a standard QP form with the following constraints:

$$\mathbf{c}^* = \arg\min_{\mathbf{c}\in C} \frac{1}{2}\mathbf{c}^T\mathbf{H}\mathbf{c} + \mathbf{f}^T\mathbf{c} \tag{3.24}$$

$$\text{s.t.} \quad \mathbf{c}_{min} \preceq \mathbf{c} \preceq \mathbf{c}_{max}, \tag{3.24a}$$

where

$$H = \mathbf{X}^T W\mathbf{X}, \; f = -\mathbf{X}^T W\mathbf{F},$$
$$\mathbf{c}_{min} = \begin{bmatrix} e_y^{min} & e_\psi^{min} & -\frac{\omega_{max}^2}{2\upsilon g} & -\frac{\dot{\kappa}_{max}}{6} \end{bmatrix}^T,$$
$$\mathbf{c}_{max} = \begin{bmatrix} e_y^{max} & e_\psi^{max} & \frac{\omega_{max}^2}{2\upsilon g} & \frac{\dot{\kappa}_{max}}{6} \end{bmatrix}^T, \; \kappa_{max} = 1/R_{min},$$

where $e_y^{min,max}$ denotes the minimum and maximum lateral position errors, and $e_\psi^{min,max}$ represent the minimum and maximum yaw angle errors, respectively; ω_{max} is the maximum angular velocity of the ego vehicle, υ is the friction coefficient, g is the gravitational acceleration, κ_{max} denotes the maximum curvature, and $\dot{\kappa}_{max}$ determines the maximum curvature rate to empirically indicate that the ego vehicle can only steer the wheel within a limited range under its current speed [SF97], R_{min} is the minimum turning radius that is determined by the vehicle model. The objective of Eq. (3.24) is to compute the optimal clothoidal coefficients under specific constraints. It should be noted that Eq. (17) only considers the fitting accuracy of the waypoints. However, the obtained waypoints are not guaranteed to be trackable. Furthermore, the numerical values of the clothoidal coefficients vary around zero (e.g., c_3), which can easily affect the shape of the curve. Therefore, we solve the Eq. (3.24) with constraints (18a) to consider the fitting errors, angular speed, and curvature rate that ensures the clothoid curve is properly generated and conforms to vehicle dynamics at the current speed.

Further, we can use the obtained clothoid curve to establish the PF for the ESPP through the following formulas, including the lower and upper boundary PFs, (U_{ESPP}^{lb} and U_{ESPP}^{rb}), and the attractive PF, U_{ESPP}^{attr}, as follows:

$$U_{ESPP}^{lb} = A_e \left(1 - e^{-b_w sign(y - f_{cr}(x))\sqrt{\left(\frac{y-b_y}{m_y} - x\right)^2 + (f_{cr}(x)-y)^2}}\right)^2 \tag{3.25}$$

Algorithm 2 Curve Fitting with Hybrid Waypoints

Initialization:$P_{ip}, P_{new} \leftarrow \mathbf{0}$ and $N_{b2i}, N_{i2s}, p_{num}$
Compute $P_{ip} \leftarrow Intersect(P_{bp}, P_{sp})$
Interpolate N_{b2i} Waypoints between P_{bp} and P_{ip}
Interpolate N_{i2s} Waypoints between P_{ip} and P_{sp}
Conduct Curve Fitting based on Eq. (14) and (15), respectively.
Obtain $\mathbf{c}^*$ based on Eq. (16) and (17)
while p_{num} **do**
    Compute U_{ESPP} based on Eq. (18), (19), and (20):
    Obtain P_{new} by Gradient Descent
    $p_{num} \leftarrow p_{num} - 1$
end while

Output: new waypoints P_{new}

$$U_{ESPP}^{rb} = A_e \left(1 - e^{b_w sign(y - f_{cl}(x)) \sqrt{\left(\frac{y-b_y}{m_y} - x\right)^2 + (f_{cl}(x) - y)^2}}\right)^2 \tag{3.26}$$

$$U_{ESPP}^{attr} = \frac{1}{2} \xi D(X_d, Y_d)^2, \tag{3.27}$$

with A_e is the maximum amplitude of the ESPP's PF, $(x,\ y)$ is the position pair of the ego vehicle in vehicle coordinate, b_w denotes the parameter controlling the road PF width [Sna18], $f_c(x)$ is the optimal curve that is obtained from Eq. (3.24), $f_{cr}(x)$ and $f_{cl}(x)$ are the right and left boundaries of the ESPP, respectively, which are acquired by shifting $f_c(x)$, ξ is the influence factor of the attractive PF, U_{ESPP}^{attr}; and $D(X_d, Y_d)$ denotes the Euclidean distance between the ego vehicle and the temporary target point from the clothoid curve. Note that Eqs. (3.25) and (3.26) are used to establish an impenetrable PF that keeps the vehicle tracking around the ESPP trajectory. In addition, we use Eq. (3.27) to produce the attractive force instead of Eq. (3.1) when the "blind alley" problem is detected, considering Eq. (3.27) can generate a more potent force to lead the ego-vehicle to follow the optimized clothoid curve. Finally, we can model the 3D PF of the ESPP and obtain the emergency collision-free path by repeating the process described in Section 3.3.1. We also present the curve-fitting process using hybrid points in Algorithm 2. Therefore, the ESPP can guide the ego vehicle to conduct emergency collision avoidance and safe stop maneuvers. Overall, the proposed system architecture of the ESPP method is depicted in Fig. 3.25, which indicates the workflow of the internal modules.

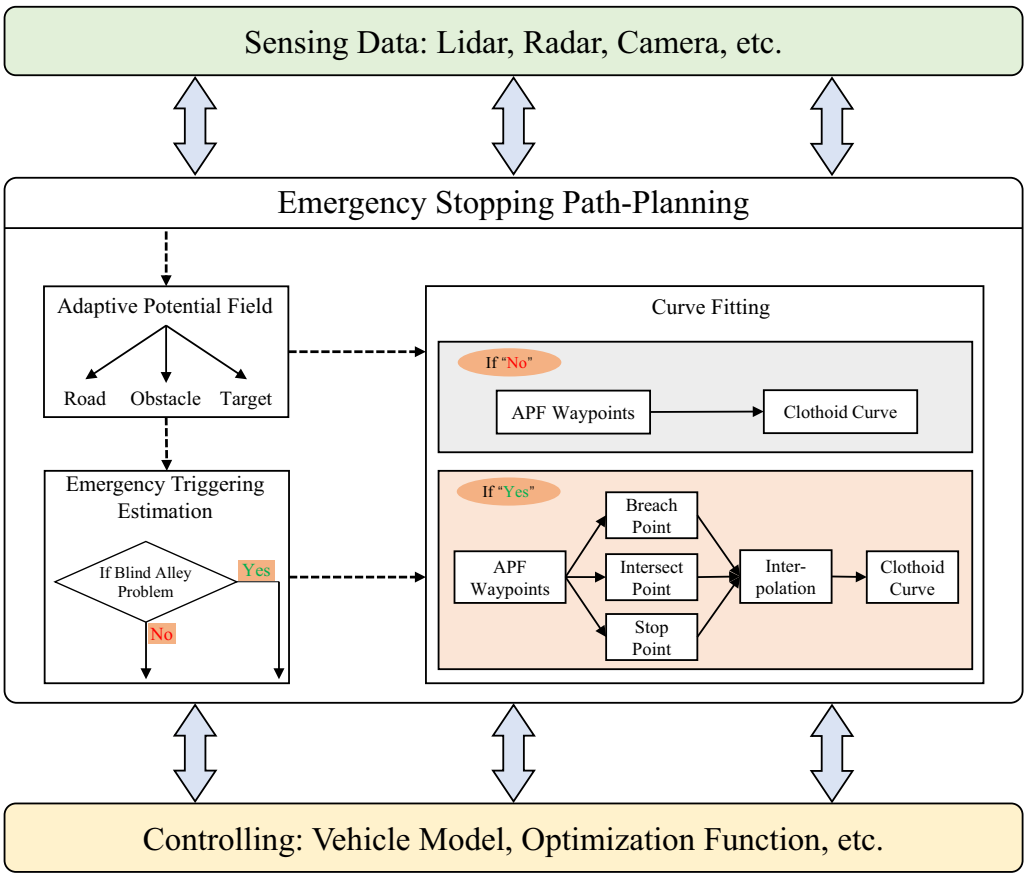


Figure 3.25: Detailed system architecture of the proposed ESPP method

Simulation results and analysis

We conducted a comprehensive co-simulation study using MATLAB/Simulink and CarSim simulator to verify the proposed ESPP-based APF method. To compare the effectiveness of the proposed method, we computed four types of path planners as follows: (i) conventional PF with constant speed (denoted as CPF with CS); (ii) adaptive PF with full braking maneuver (denoted as APF with FB) [LLY+20]; (iii) adaptive PF without the lower road PF when sensing the emergency (denoted as APF without LR); and (iv) ESPP-based adaptive PF (denoted as ESPP-based APF). The overall simulation was conducted on a laboratory laptop with Intel(R) Core(TM) i9-10980HK CPU@2.40GHz and RAM 32GB.

Table 3.1: Parameters of ESPP-based PF

$Parm.$	$Val.$	$Parm.$	$Val.$
A_{lane}	20	A_{obs}	150
l_w	1.6 m	L	0.3
ζ	1	Y_c	4
υ	0.75	ξ	0.2
η	3	$e_y^{min,max}$	$\pm$ 0.7 m
l_f	1.232 m	$e_\psi^{min,max}$	$\pm$ 0.05 rad
$Y_{u,l}$	(8,0)	ω_{max}	4.9
l_r	1.468 m	R_{min}	6.12 m

Environment settings To simulate the high-speed scene, we initialized the longitudinal speed of the adjacent obstacle at 115.2 km/h, and the longitudinal speed of the ego vehicle was initially set at 108 km/h. The adjacent obstacle is suddenly steered without a pre-warning when it is one body position ahead of the ego vehicle to simulate an extreme emergency scene. For longitudinal control, we assume that the ego vehicle conducts a full brake with a maximum deceleration after the reaction time. Therefore, we directly apply the anti-lock brake system (ABS) controller in the CarSim Simulator when the "blind alley" problem is detected. In addition, we applied five different vehicle mechanical models with 27 degrees of freedom (DOF) [YWSH20] provided in CarSim to simulate different vehicle dynamics, including Sedans, full-size SUVs, large Van, full-size pickups, and cargo trucks. The emergent PF restricts the ego vehicle from driving within the planned route and achieves a safe stop. The parameter settings of ESPP-based APF are described in Table. 3.1. It is worth noting that A_{obs} should be set to an immense value, which ensures the obstacle PF is not traversable. Besides, the numerical value of A_{lane} should be small because the vehicle needs to violate the lane PF when a lane-change decision has been made. The numerical values of ω_{max} and R_{min} are determined based on the selected car model in the CarSim simulator; for example, the D-class sedan is chosen in this study. In addition, l_w, l_f, and l_r can also be available from the CarSim simulator.

Simulation results In Table. 3.2, we can observe the overall performance of the four planners under different high speeds. Although both the CPF with CS and APF with FB can produce a smoother path, their response times are relatively shorter than the APF without LR and ESPP-based APF due to the "blind alley" problem. Consequently, they fail to accomplish collision avoidance as well as the safe stop for all scenarios. On the other hand, the APF without LR can achieve collision avoidance and safe stop

Table 3.2: Performance Evaluations

	20 m/s				25 m/s				30 m/s				35 m/s			
Planners	AC (1/m)	RT (s)	CA	SS	AC (1/m)	RT (s)	CA	SS	AC (1/m)	RT (s)	CA	SS	AC (1/m)	RT (s)	CA	SS
CPF w CS	5.2e-3	5.73	✗	✗	6.3e-4	4.07	✗	✗	2.5e-3	4.01	✗	✗	1.2e-3	4.05	✗	✗
APF w FB	2.6e-3	6.18	✗	✗	1.4e-3	5.55	✗	✗	1.1e-3	4.21	✗	✗	7.2e-4	4.11	✗	✗
APF w/o LR	4.3e-2	6.95	✓	✓	3.0e-1	6.64	✓	✓	3.2e-1	7.54	✓	✓	3.7e-3	3.85	✗	✗
ESPP-APF	**3.7e-3**	**6.87**	✓	✓	**4.4e-3**	**6.49**	✓	✓	**1.3e-3**	**7.25**	✓	✓	**2.8e-3**	**8.11**	✓	✓

* AC: Average Curvature RT: Response Time CA: Collision Avoidance SS: Safe Stop

for the scenarios of 20 m/s, 25 m/s, and 30 m/s, but its average curvature is larger than other planners, which means the smoothness of the path and the ride comfort performs worse. Besides, we found the response time of the APF without LR is similar to that of the ESPP-based PF but slightly larger because the planner will stop its response when the vehicle is stopped, which implicitly indicates the PF without LR takes longer to complete the safe stop. In the scenario of 35 m/s, the PF without LR fails to accomplish collision avoidance and has the shortest response time than other planners because it quickly hits the boundary of the emergency stopping lane due to the entire loss of control. On the opposite, the ESPP-based PF can finish all the tasks and produce a smoother path. Next, we will compare and analyze more detailed data. The trajectories of the ego vehicle obtained by applying the 4 different path planners are shown in Fig. 3.26. We can observe that the trajectory of the CPF with CS (denoted by the red dash-dotted line) experiences a side collision with the obstacle (blue vehicle), while that of the APF with FB (denoted by the cyan dashed line) ends up with a rear-end collision with the obstacle. On the other hand, the trajectory of the APF without LR (denoted by the magenta dotted line) successfully avoids the obstacle; however, experiences an apparent tortuous part from 200–160 m. The trajectory of the ESPP-based APF also avoids the obstacle while ensuring a smoother curvature in the stopping maneuver. In addition, the total length of the ESPP-based PF trajectory was shorter than that of the PF without LR, resulting in a faster stopping maneuver.

As depicted in Fig. 3.28, the front wheel steering angles of the CPF with CS and the APF with FB end up at the time 3.96 s and 4.2 s, respectively, owing to the collision. When the front wheel steering angle of the APF without LR reaches the maximum at 0.13 rad and the minimum at -0.12 rad, during the emergency collision avoidance from 2.67–6.18 s. On the contrary, the front wheel steering angle of the ESPP-based APF varies between 0.03 rad and -0.02 rad, which is smaller than that of the APF without LR. Correspondingly, the heading angle of the APF without LR reaches -0.28 and 0.22 rad, which are more extensive than that of the ESPP-based APF (with the minimum value at -0.18 rad), as depicted in Fig. 3.29. The longitudi-

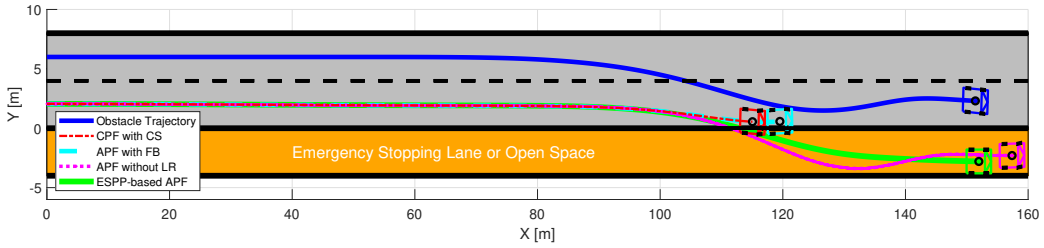


Figure 3.26: Vehicle trajectories of different path planners: the gray area represents the typical freeway, and the orange area denotes the emergency stopping lane or open space.

nal speeds of the four wheels of the ego vehicle are shown in Fig. 3.30 and 3.31. We observed that the four wheels of the APF without LR exhibited severe oscillations from 3–5.2 s, which is caused by the excessive wheel slip, requiring a longer time to complete the entire braking maneuver. In contrast, the four wheels of the ESPP-based APF exhibited a marginal vibration from 3.2–3.8 [s] that enabled the ego vehicle to complete the braking procedure earlier than the APF without LR. The lateral accelerations of the ego vehicle are shown in Fig. 3.32; the APF without LR exhibited a larger lateral acceleration (up to 0.9 m/s^2) than the ESPP-based APF (up to -0.48 m/s^2) during the emergency collision avoidance. Fig. 3.33 shows the variation of the stop point that is calculated from Algorithm 1. The stop point's X- and Y-axes can jump first at 3.56 s when the emergency situation occurs, and the X-axis varies two times at 4.33 and 6.28 s, respectively, because of the preset constraint conditions. The coordinates of the stop point are finally initialized to $(0, 0)$ when the ego vehicle stops. In addition, Figs. 3.28, 3.29, and 3.32 show smoother and smaller responses and control inputs of the system with the proposed ESPP method compared to other methods.

From Fig. 3.34 to Fig. 3.37, the rotational dynamics can be observed, including the rolling resist moment (RRM) of four tires and the roll rate (RR) of four wheels. In Fig. 3.34, we can see that the RRMs of Tire L1 and Tire R1 are over 100 N-m in APF without LR-based path planner, while that of ESPP-based path planner maintains between 53 N-m to 102 N-m from 3.2 s to 7.2 s, as depicted in Fig. 3.35. Besides, the RRM of Tire L1 of the APF without LR-based path planner drops dramatically from 104.3 N-m to 13.21 N-m at $T = 3.8$ s, possibly due to the tire slip. In addition, the RRMs of the rear tires from both planners vary around 0 N-m. On the other hand, the roll rates of four wheels from the APF without LR-based path planner have obvious oscillations during the braking period (from 3.2 s to 6.7 s) that

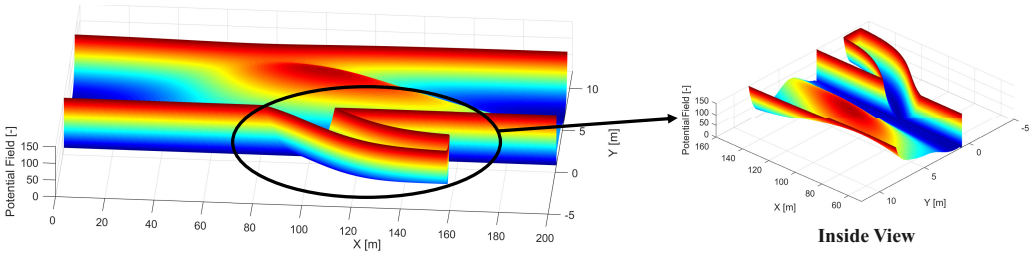


Figure 3.27: 3D potential field modeling of the ESPP: Opening a breach for the ego-vehicle to avoid collision

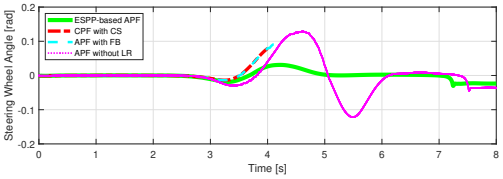


Figure 3.28: Front wheel steering angles of the ego vehicle.

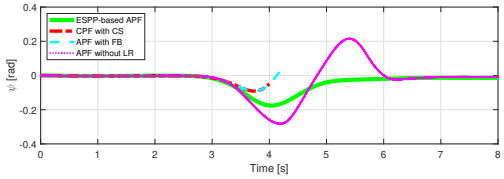


Figure 3.29: Heading angles of the ego vehicle.

reach 10.1 deg/s at $T = 4.5$ s and -11.6 deg/s at $T = 5.8$ s, as shown in Fig. 3.36. Conversely, as stated in Fig. 3.37, the roll rates of four wheels from the ESPP-based path planner vary under ± 3.8 deg/s with a shorter oscillation period.

The computational time is depicted in Fig. 3.38, we can observe that the initial computational time of ESPP-based APF is higher than other planners because it has more parameters to be initialized. From $T = 3.2$ s to $T = 4.5$ s, we can see that the computational time of ESPP-based APF is also increasing more rapidly than other planners due to the activation of the ESPP. In addition, more peaks exist in the green solid line than in other lines after $T = 3$ s because the emergency triggering estimation detects the "blind alley" problem and activates the ESPP to reach a safe stop, involving solving several constrained optimizations at those peaks. Although the average computational time of the proposed method is higher than other methods, the overall performance is still under 0.04 s, which has conformed to the real-time requirement (within 100 ms) in autonomous driving [Ren23].

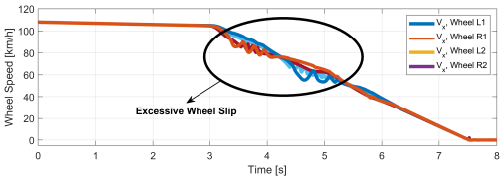


Figure 3.30: (Linear) Longitudinal speeds of four wheels of APF without LR: L1 is the left front wheel; R1 is the right front wheel; L2 is the left rear wheel; R2 is the right rear wheel

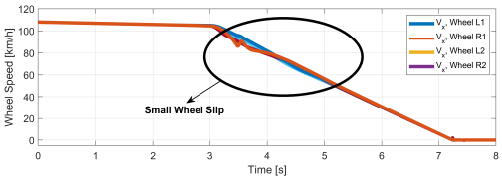


Figure 3.31: (Linear) Longitudinal speeds of four wheels of ESPP-based APF: L1 is the left front wheel; R1 is the right front wheel; L2 is the left rear wheel; R2 is the right rear wheel

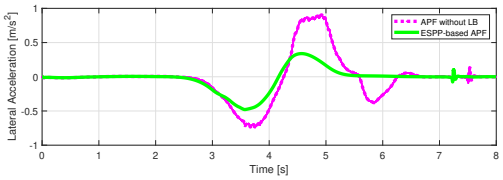


Figure 3.32: Lateral accelerations of the ego vehicle.

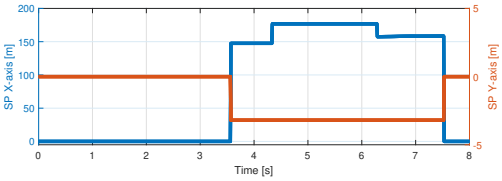


Figure 3.33: Longitudinal and lateral coordinates of the stop point (SP).

Conclusions

In this subsection, we proposed an emergency-stopping path planning combined with the adaptive potential field and optimized clothoid curve to overcome an extreme emergency situation in which the obstacle steers recklessly without a pre-warning. We compared our proposed method with three other path planners in a co-simulation study using Simulink and the CarSim simulator to verify its performance. The simulation results revealed that the proposed method demonstrates effective emergency collision avoidance capabilities, enabling the vehicle to come to a safer stop compared to conventional methods. Moreover, the proposed approach exhibits the advantage of generating a smoother trajectory, contributing to improved ride comfort for passengers. Despite its longer response time when compared to other methods, even in high-speed scenarios, the proposed method still exhibits reliable collision avoidance performance. Additionally, the proposed method addresses the issue of wheel slip, a phenomenon that typically occurs during sudden braking, and effectively mitigates its effects. By doing so, it ensures a more stable and controlled deceleration, enhancing overall safety during crit-

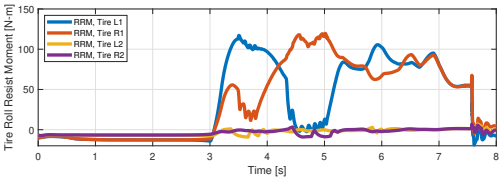


Figure 3.34: Rolling resist moment of four tires from the APF without LR-based planner: L1 is the left front tire; R1 is the right front tire; L2 is the left rear tire; R2 is the right rear tire

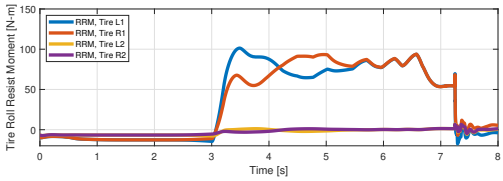


Figure 3.35: Rolling resist moment of four tires from the ESPP-based planner: L1 is the left front tire; R1 is the right front tire; L2 is the left rear tire; R2 is the right rear tire

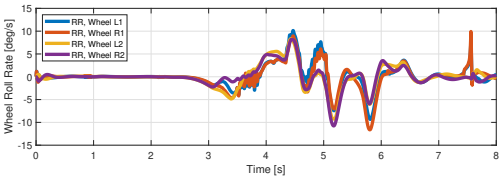


Figure 3.36: Roll rate of four wheels from the APF without LR-based planner

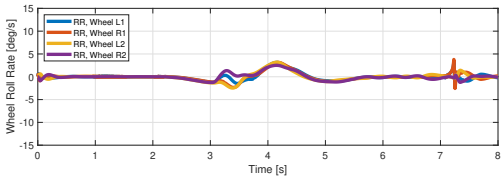


Figure 3.37: Roll rate of four wheels from the ESPP-based planner

ical braking maneuvers. Furthermore, the benefits of the proposed method extend beyond safety considerations, as it also generates a more comfortable lateral acceleration. This improvement in lateral dynamics contributes to a smoother and more pleasant ride experience for vehicle occupants. Taken together, the simulation results demonstrate the effectiveness and versatility of the proposed method, making it a promising solution for enhancing both safety and ride quality in emergency scenarios.

3.4 Planning in connected vehicles

3.4.1 Risk assessment index

Current PF targets mainly NAVs by evaluating their relative position and velocity. In addition, the risk energy of the PF is usually assigned an infinite value along the z-axis. Therefore, this subsection presents an enhanced adaptive PF based on Eq. (3.18) with a novel risk assessment index (RAI)

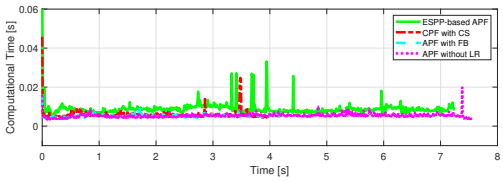


Figure 3.38: Computational time of the planners.

for CAVs, which has been presented in [4]. Valuable information (heading angle, steering wheel angle, etc.) other than relative position and velocity is supplemented to the adaptive PF. Furthermore, we separate the proposed adaptive PF from the cost function of the MPC to compute the desired reference signals directly, saving more computation time. Recently, [WHK+20] built an ethical decision-making platform in autonomous vehicles by solving a so-called lexicographic optimization, but the PF is pre-assigned with an infinite risk value, and a time-consuming problem appears. Therefore, we propose an adaptive PF with the RAI for CAVs with V2V communication, which is also combined with a specific MPC controller. We briefly summarize the contribution of this paper as follows.

- We present a modified system framework by separating the PF from the MPC controller's cost function for time-saving, shown in Fig. 3.39.
- We introduce an improved adaptive PF. Valuable information is supplemented into the potential functions to consider the motions of surrounding vehicles, providing better ride comfort.

Compared to the light-of-sight (LOS) sensors (radar, camera, lidar, etc.), V2V communication enables the ego-vehicle to perceive more information about the surrounding objects, including the speed, heading angle, etc. In this paper, the relative speed between the ego-vehicle and obstacle vehicle is considered as a referential RAI [GHCG13]:

$$R_{\Delta V} = \frac{v - v_o}{\sqrt{(X - X_o)^2 + (Y - Y_o)^2}}, \tag{3.28}$$

From the crash severity study [RD94], the relative heading angle between the ego-vehicle and obstacle vehicle is also an important judgement of potential collision. In this study, we divide the relative heading angle into three categories with pre-assigned penalty scores:

$$R_{\Delta\theta} = \begin{cases} 5 & \Delta\theta = 0^\circ \sim 45^\circ \mid 135^0 \sim 180^0, \\ 3 & \Delta\theta = 45^\circ \sim 90^\circ \mid 90^\circ \sim 135^0, \\ 1 & \Delta\theta = 0^\circ \mid 180^\circ. \end{cases} \tag{3.29}$$

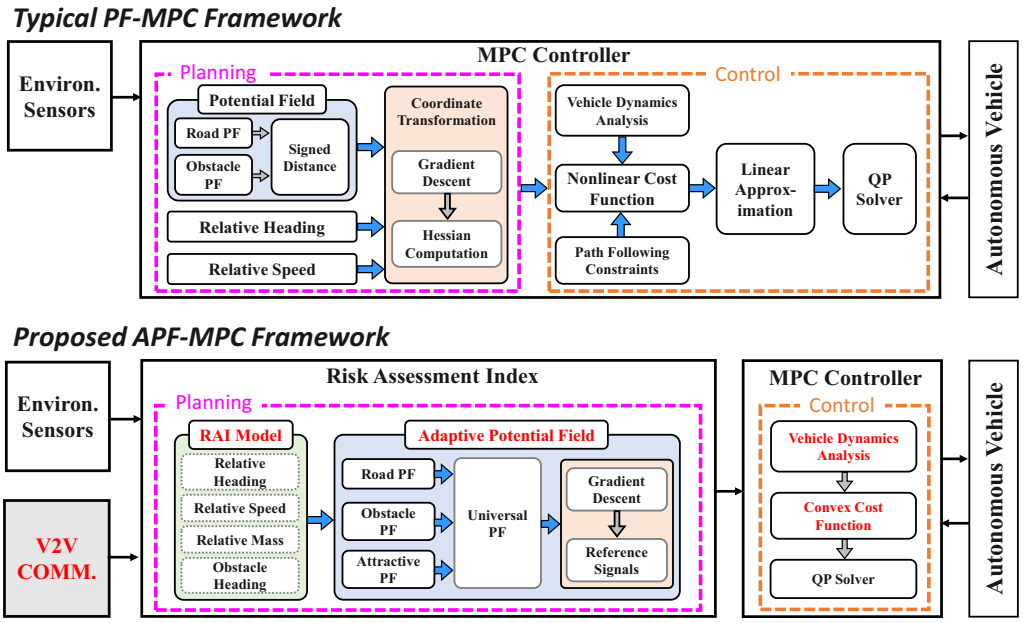


Figure 3.39: Differences between the typical PF-MPC framework and proposed APF-MPC framework (zoom in to see the details).

Furthermore, the relative mass between the ego-vehicle and obstacle vehicle also accounts for risk assessment. Similar to human drivers, it will be safer to stay away from heavy vehicles (e.g., truck and bus) [AKR+04]. Therefore, we simply take the mass ratio as the RAI:

$$R_{\Delta M} = \frac{M_o}{M}. \tag{3.30}$$

Then, we can sum up the above RAI to get the total collision risk:

$$\xi_{rai} = k_{\Delta v} R_{\Delta V} + k_{\Delta \theta} R_{\Delta \theta} + k_{\Delta M} R_{\Delta M} + \xi_o, \tag{3.31}$$

where $k_{\Delta v}$, $k_{\Delta \theta}$, and $k_{\Delta M}$ are the weighting parameters of the RAI in terms of ΔV, $\Delta \theta$, and ΔM, ξ_o denotes the initial collision risk. Therefore, we can replace A_{obs} in Eq. (3.3) with ξ_{rai}:

$$P_o(X, Y) = \xi_{rai} \exp\left\{ [-\frac{C_1}{2}(\frac{(X - X_o)^2}{\sigma_x} + \frac{(Y - Y_o)^2}{\sigma_y} - C_2)] \right\}, \tag{3.32}$$

The significant advantage of an MPC controller is that it incorporates vehicle kinematics and dynamics, constraining the motion states in accordance with the actual mechanical structure of the vehicle, which will be introduced in the next chapter with a detailed explanation.

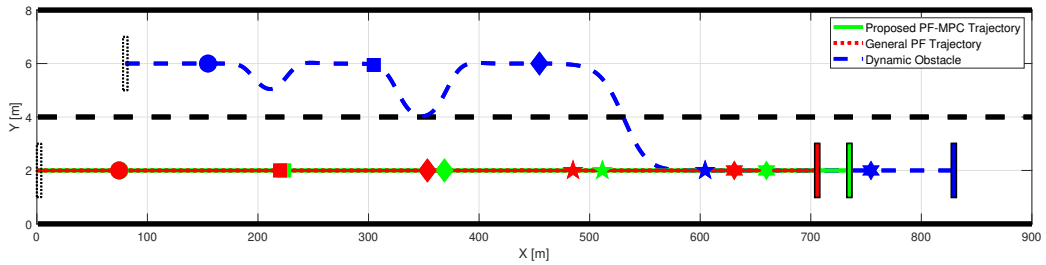


Figure 3.40: Trajectories of the obstacle vehicle, PF-MPC, and APF-MPC

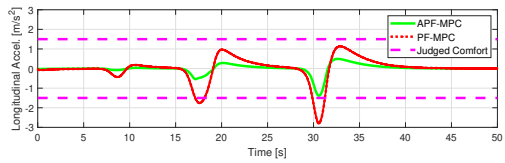
Simulation results and analysis

To evaluate the performance of the APF-MPC framework, we have conducted a comparative simulation study under the co-simulation of MATLAB/Simulink and CarSim (Mechanical Simulation). The overall simulation was conducted in a personal laptop with Intel(R) Core(TM) i5-9300H CPU@2.40GHz and RAM 8GB.

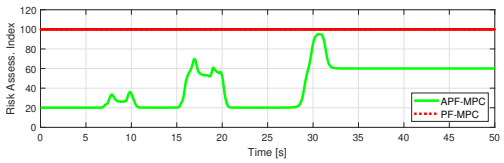
Simulation settings We assume that a human driver drives the front obstacle vehicle with the V2V communication device in the scenario setting. The initial position of the obstacle vehicle is set at ($X_o = 80,\ Y_o = 6$), and the obstacle vehicle speed is the same as the ego vehicle with 15 [m/s]. And the V2V communication range is set at around 300 [m] and the time delay is assumed to be at 10 [ms], and the sending frequency of the V2V message is set to be 10 Hz. Besides, to evaluate the performance, the trajectory of the obstacle vehicle is predefined to deviate from its original lane centerline several times and finally change to the adjacent lane. And then, we import the predefined trajectory into the CarSim simulator to obtain the heading angle and speed.

Simulation results The vehicle trajectories are depicted in Fig. 3.40 where we can observe that the obstacle vehicle deviated several times from the upper lane center. The trajectory of PF-MPC is shorter than that of the APF-MPC, maintaining a larger distance of around 120 [m] from the obstacle vehicle. We can observe that the longitudinal deceleration of the PF-MPC reaches -1.75 [m/s^2] at 17.6 [s] and -2.8 [m/s^2] at 30.6 [s] that exceed the judged longitudinal riding comfort (1.47 [m/s^2]). On the opposite, the longitudinal deceleration of the APF-MPC varies between 0.49 [m/s^2] and -1.38 [m/s^2] is well-computed in the range of judged longitudinal comfort, as shown in Fig. 3.41(a).

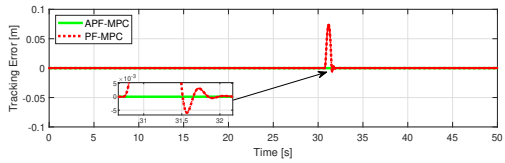
Fig. 3.41(b) describes the significant difference between the PF-MPC and



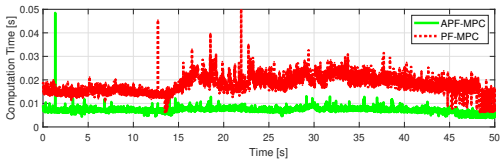
(a) Longitudinal acceleration of the vehicle



(b) Risk assessment index of APF-MPC and PF-MPC



(c) Tracking error in lateral position reference



(d) Computation time of APF-MPC and PF-MPC

Figure 3.41: Longitudinal motion states, RAI, tracking error, and computation time of the comparative simulation results

the APF-MPC. The PF-MPC framework assigns a fixed or infinite risky energy along the Z-axis (100 in this scenario) to calculate the collision risk between the ego-vehicle and surrounding obstacle vehicles. Instead, the APF-MPC framework initializes a lower value (20 in this scenario) for the obstacle vehicle in the lane-keeping mode. The motion states factor varies in real-time by assessing the motion state information of the obstacle vehicle synthetically. We can see there exist two humps in 9 [s] and 16 [s] when the adjacent vehicle deviates from its lane. The reason for the two humps is that the obstacle vehicle's heading angle and steering wheel angle change toward positive at the corresponding positions, which indicates that the steering wheel turns counterclockwise to return to the upper lane center. Therefore, the IAF of the APF-MPC decreases in the middle of the two humps. In Fig. 3.41(c), the tracking error of the PF-MPC framework is up to nearly 0.07 [m] when the obstacle vehicle changes its lane. In comparison, the tracking error of the APF-MPC varies around 0 [m] to have a better tracking performance.

From Fig. 3.41(d), we can observe that the computation time of the PF-MPC exceeds 0.04 [s] several times from 10 [s] to 25 [s], and the average computation time is 0.018 [s]. On the contrary, the computation time of the APF-MPC is generally below 0.015 [s] through the overall simulation; the average computation time is 0.007 [s], which is 0.011 [s] faster than the PF-MPC method.

Conclusions

We have presented a unique combination of potential field and V2V communication to estimate the surrounding vehicles' driving intentions for connected autonomous vehicles. To reflect the motion states, we have updated the potential function of the obstacle vehicle by adding more motion information, including heading angle, steering wheel angle, relative vehicle mass, etc. Then, we introduced a risk assessment based on the improved PF to plan the reference signals. Besides, an MPC-based tracking controller has been presented with a specific vehicle kinematic model, including motion prediction, constraints analysis, and optimization design.

3.4.2 Event-based hybrid planning

The existing inherent limitations of the PF make it vulnerable in some specific traffic scenarios, such as local minimum, oscillations in close obstacles, etc. Therefore, a hybrid path planning with the sigmoid curve is recently presented to generate better trajectories than the PF in collision avoidance; but it is time-consuming and less applicable in complex dynamic environments, especially in traffic emergencies. To solve the above deficiencies, we present a cooperative hybrid path planning (CHPP) collaborative with adjacent vehicles for emergency collision avoidance via V2V communication. In addition, the RSS model is used to enhance the PF and sigmoid curve for safe-critical and time-saving requirements. This subsection gives the descriptions published in [5].

Safe-critical sigmoid curve

To solve the local minima problem existing in the PF, the sigmoid curve is proposed for generating a smoother and shorter path [LHY+20]. However, as stated before, the computation time increases and collision avoidance is not guaranteed in handling rear-coming obstacles. Therefore, we propose a safe-critical sigmoid curve combined with the RSS-based PF:

$$f_{sig}(X) = \frac{W}{1 + e^{-k(X-P_c)}} + b, \tag{3.33}$$

where W is the lateral width from the current position to the center of the target lane, k denotes the slope at the centrosymmetric point of the sigmoid curve and P_c is the longitudinal position of the centrosymmetric point, b means the bias. Unlike [LHY+20] defines the parameters of the sigmoid curve manually, we use the RSS to generate the sigmoid curve. As shown in

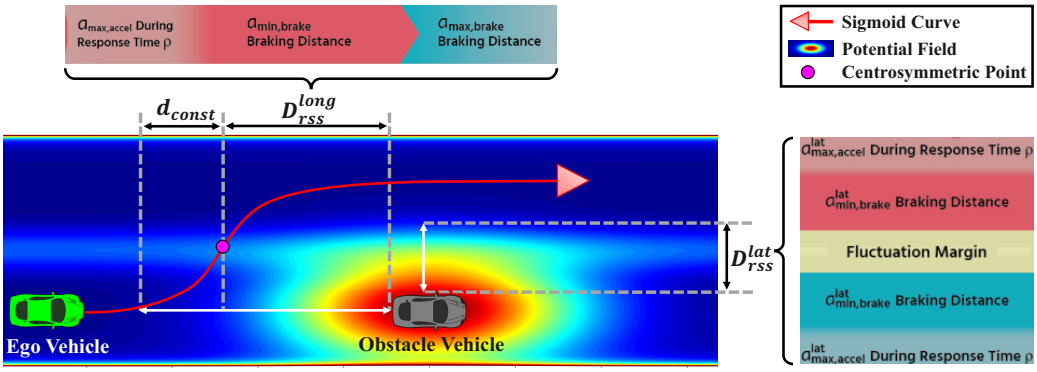


Figure 3.42: RSS-based potential field and sigmoid curve.

Fig. 3.42, the centrosymmetric point is defined according to the longitudinal RSS:

$$P_c = X_{obs}^i - D_{rss}^{long}. \tag{3.34}$$

And W should satisfy the safe constraint with the lateral RSS and road borderline:

$$Y_{obs}^i + D_{rss}^{lat} \leq W < Y_u - \frac{l_w}{2}. \tag{3.35}$$

In addition, the slope at the centrosymmetric point is determined by the ratio of the longitudinal RSS to the relative distance between the ego-vehicle and the obstacle but should be constrained to consider the vehicle dynamics, as depicted in Fig. 3.43:

$$k = \max\left(\frac{D_{rss}^{long}}{X_{obs}^i - X}, k_{con}\right), \tag{3.36}$$

where k_{con} is the slope constraint. In this way, the sigmoid curve is safer to track and saves more computation time compared with [LHY+20].

Speed planning with RSS

For real applications, the assumption of constant speed is impractical, especially when dealing with closely spaced obstacles. To compute the safe speed profile, we use the longitudinal RSS to calculate the desired target speed. In Fig. 3.44, we monitor the D_{rss}^{long} to determine whether deceleration is required for driving safety. In this study, we consider it safe to overtake multi-obstacles when D_{rss}^{long} is less than half of the relative distance between obstacles.

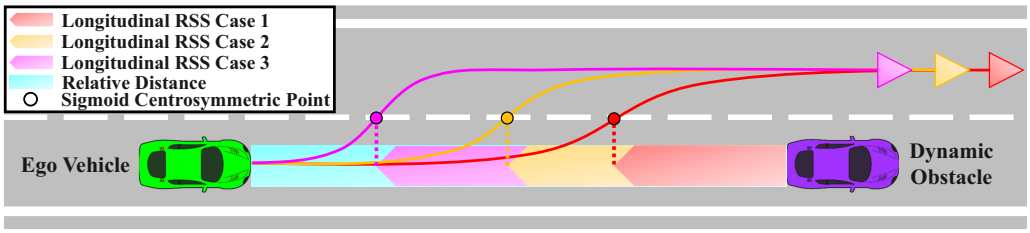


Figure 3.43: The slope at the centrosymmetric point of the sigmoid curve.

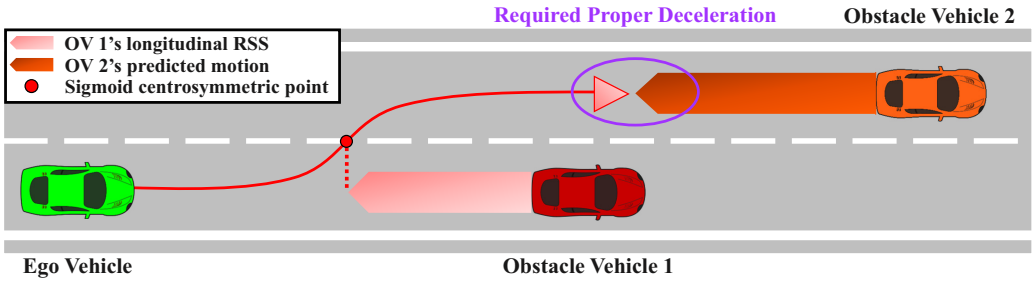


Figure 3.44: Scene description of a required proper deceleration in overtaking multi-obstacles.

Cooperative driving in emergency scenarios

Cooperative driving is reported to be an important technology for solving traffic emergency scenarios [ECP+16]. As mentioned before, current PF-based hybrid path planning methods are primarily focused on NAVs that are non-cooperative with other road users. Therefore, we propose a novel emergency cooperation method to calculate the desired cooperative speed for adjacent vehicles based on the longitudinal RSS and the safe-critical sigmoid curve. We added a supplementary rule to the longitudinal proper response in [SSSS17] for cooperative driving.

Definition 1 (**Longitudinal Proper Response**). *Let t be a longitudinally dangerous time for cars c_1, c_2 and t_b^{long} be the corresponding longitudinally blame time. Cars c_1 and c_2 are driving at different lanes. Assume that c_1 is the rear car. If at the longitudinal danger threshold time, the longitudinal proper response of the two cars is to comply with the following constraints on the longitudinal speed:*

1. c_2 determines a lane-changing behavior owing to emergencies. Subsequently, the acceleration of c_2 must be at most a_{accel}^{max} during $[t_b^{long}, t_b^{long} + \rho]$. Afterwards, c_2 must send c_1 a desired cooperative speed V_{coop}.

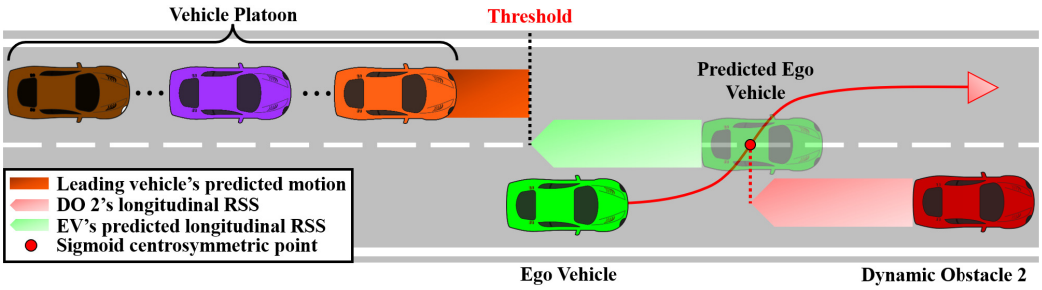


Figure 3.45: Cooperative planning for the adjacent dynamic vehicle if it is willing to cooperate.

2. The acceleration of c_1 *must be at most* a_{accel}^{max} *during the time interval* $[t_b^{long}, t_b^{long} + \rho]$*. Afterwards,* c_1 *must be at least* a_{brake}^{max} *until it reaches* V_{coop}*. Subsequently, any non-negative acceleration is allowed.*

Let us consider a driving scenario depicted in Fig. 3.45. The ego vehicle is driving on the lower lane of the road. Suddenly, the front dynamic obstacle 2 brakes because of emergencies (e.g., unexpected entity), and a vehicle platoon is driving in the upper lane. In this scenario, the ego-vehicle has two options: change its lane and/or brake for a safe stop.

Lane change for collision avoidance Suppose the ego-vehicle is unable to stop on the highway considering a high probability of secondary accidents occurring [SY19]. In that case, it is necessary to perform cooperative driving behavior with the adjacent vehicle platoon in case of a potential lane-change collision. According to Definition 1, the ego-vehicle requiring emergency cooperation should send the desired coordinated speed information to the cooperative objects. Therefore, based on the safe-critical sigmoid curve, we can obtain the position of the sigmoid centrosymmetric point based on the longitudinal RSS with dynamic obstacle 2. Subsequently, the time T_{reach} arriving at the centrosymmetric point can be calculated:

$$T_{reach} = \frac{X_{obs}^2 - D_{rss}^{long} - X}{V}. \tag{3.37}$$

Hence, for the leading vehicle of the platoon, we can calculate the predicted longitudinal motion with Eq. (3.37), as shown in Fig. 3.45. The predicted motion for the leading vehicle of the platoon during the time interval $[t, t + T_{reach}]$ can be calculated as follows.

$$X_{obs}^{lead,pred} = X_{obs}^{lead} + V_{obs2} T_{reach} + \frac{a_{obs}^{lead} T_{reach}}{2}, \tag{3.38}$$

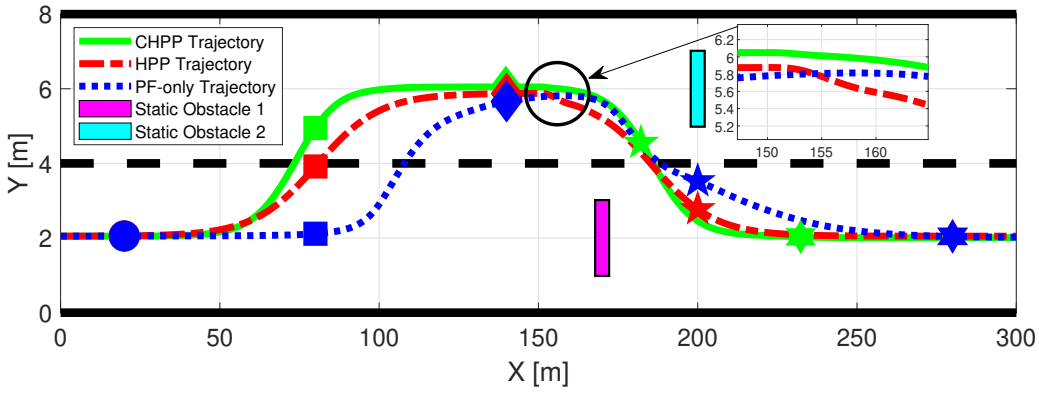


Figure 3.46: Vehicle trajectories in static scenario.

with a_{obs}^{lead} denotes the current acceleration of the leading vehicle. We can then obtain the predicted longitudinal RSS $D_{rss}^{long,\,pred}$ at the centrosymmetric point. Finally, we have the following threshold for longitudinal safety during the lane-changing phase.

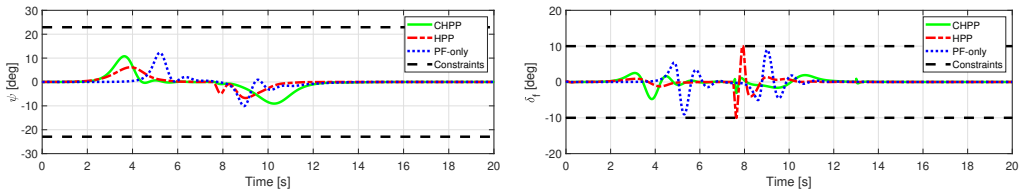
$$X_{obs}^{lead,pred} \leq P_c - D_{rss}^{long,pred} \tag{3.39}$$

By solving the above inequality, we can obtain the desired coordinated speed V_{coop} for the leading vehicle of the platoon.

Braking for safe stop In a case where the adjacent vehicle platoon is non-cooperative or non-response, a braking maneuver is required for a safe stop to prevent the longitudinal collision. As introduced before, the RSS-based PF includes the minimal safe longitudinal distance that reserves sufficient space for the ego-vehicle with a comfort deceleration at a_{brake}^{min}. Therefore, when the adjacent vehicle platoon is non-cooperative or non-responsive, the ego-vehicle can conduct a braking deceleration with a_{brake}^{min} to process a safe and comfortable stopping maneuver.

Simulation results and analysis

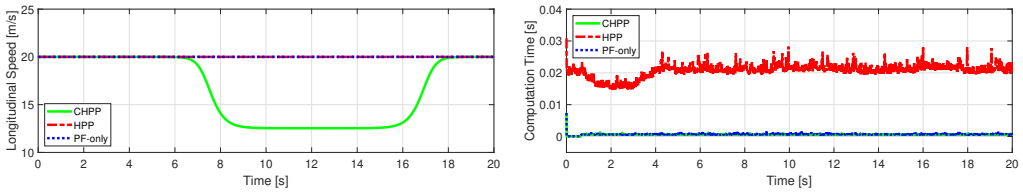
This subsection will describe the simulation settings and results in detail. Two traffic scenarios, including static and dynamic environments, were set to evaluate the performance of the proposed method via MATLAB/Simulink and CarSim. The overall simulation was conducted on a laboratory laptop with Intel(R) Core(TM) i9-10980HK CPU@2.40GHz and RAM 32GB. Three comparative path planning methods were computed: i) Proposed



(a) Yaw angles of the ego-vehicle in the static scenario.

(b) Front tire steering angles of the ego-vehicle in the static scenario.

Figure 3.47: Yaw and front tire steering angles of the ego-vehicle in the static scenario.



(a) Longitudinal speed of the ego-vehicle in the static scenario.

(b) Computation time of CHPP, HPP, and PF-only in static scenario.

Figure 3.48: Longitudinal speed and computation time in the static scenario.

CHPP method; ii) Latest HPP method [LHY+20]; and iii) PF-only method [JKMH17].

Static scenario In this scenario, two closely spaced obstacle vehicles were set to be static at different lanes. Obstacle 1 was set at $(170, 2)$ and obstacle 2 stayed at $(200, 6)$. The ego-vehicle was driving at 20 m/s constantly in HPP and PF-only as described in [LHY+20, JKMH17].

From Fig. 3.46, it can be observed that all three path-planning methods passed the closely spaced static obstacles. However, both the HPP and PF-only had obvious-tortuous trajectories from 150 m to 200 m, while the trajectory of the proposed CHPP was constantly smooth. Furthermore, the front tire steering angles of the HPP and PF-only had some oscillations and nearly reached the preset constraint (10 deg) around the time interval [4.6 s, 9.5 s], while that of the CHPP varied more gently, as depicted in Fig. 3.47(b). A similar phenomenon can be observed in the yaw angles of the HPP and PF-only in Fig. 3.47(a); however, the yaw angle of the CHPP changed smoothly with a maximum value at 10 deg. In Fig. 3.48(a), we can observe that the longitudinal speed of the CHPP reduced to 12.53 m/s and increased again to 20 m/s after collision avoidance.

Dynamic scenario In the dynamic scenario, a three-vehicle platoon (denoted as Platoon Car 1,2,3) was set at the road upper lane (leading car: (0,6)) with an initial speed at 30.56 m/s. Other settings were described in [WN15]. Moreover, a dynamic obstacle (denoted as Obstacle Car 4) was set to (300,2) driving at 19.44 m/s in the beginning and suddenly braking after 12 s owing to emergencies. The ego-vehicle was set at (100,2) with a given speed at 25 m/s.

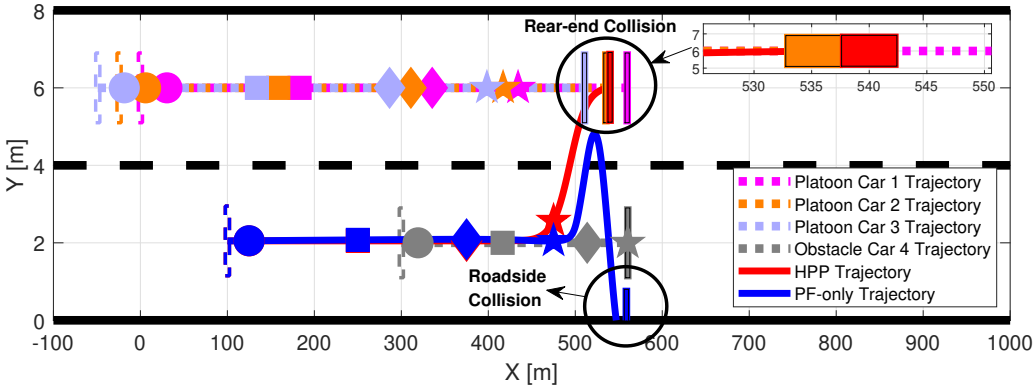


Figure 3.49: Vehicle trajectories of HPP and PF-only.

The vehicle trajectories of the HPP and PF-only are depicted in Fig. 3.49. We can observe that when Obstacle Car 4 braked suddenly, the HPP had a rear-end collision with Platoon Car 2 at 537 m, while the PF-only had a roadside collision at approximately 560 m. In Fig. 3.50, it can be observed that the CHPP does not collide with the platoon cars and the obstacle car (owing to its ability to compute the desired coordinated speed) and is subsequently sent to the vehicle platoon. As shown in Fig. 3.51(a), the desired coordinated speed started to decrease at 12.02 s, while receiving signals from the ego-vehicle until it reached 17.8 m/s after the ego-vehicle changed lanes. Subsequently, its speed increased to approximately 25 m/s to follow the ego-vehicle. Furthermore, we can observe that the vehicle platoon (car 1,2,3) can easily track the desired coordinated speed when the average tracking error is approximately 0.0945 m/s.

From Fig. 3.51(b) to Fig. 3.52(a), it can be observed that the yaw angle and front tire steering angle reached the preset constraint several times when Obstacle Car 4 suddenly brakes. On the contrary, both the CHPP and HPP had a smooth yaw angle and front tire steering angle. However, the HPP was oblivious of the rear-coming Platoon Car 2. As shown in Fig. 3.52(b), the computation time of the HPP constantly increased as the simulation began.

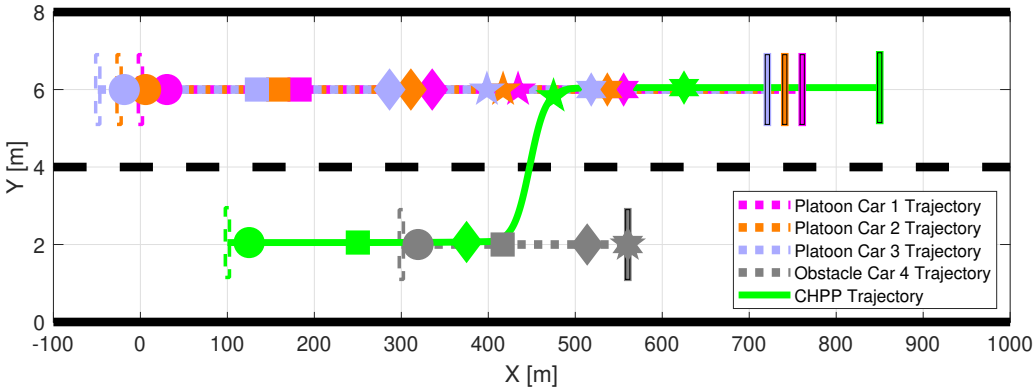
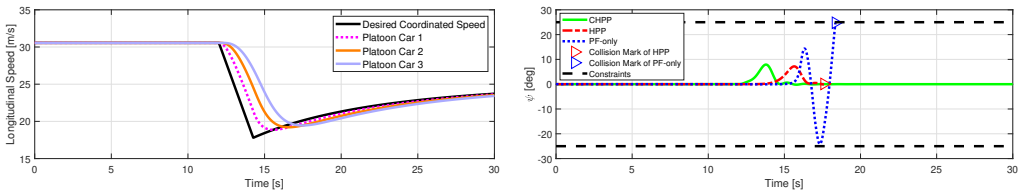


Figure 3.50: Vehicle trajectories of proposed CHPP.



(a) Desired coordinated speed for vehicle platoon.

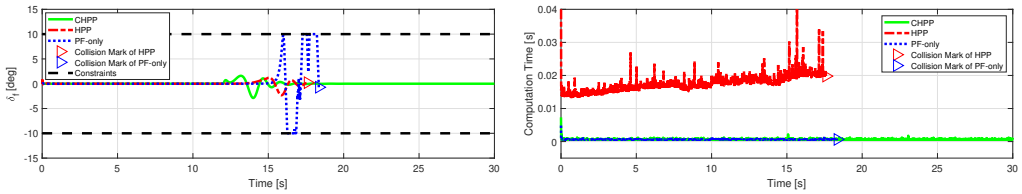
(b) Yaw angles of ego vehicle in dynamic scenario.

Figure 3.51: Desired coordinated speed and yaw angles in the dynamic scenario.

It exceeded 0.04 s at the beginning and subsequently remained at $t = 15.68$ s. Contrastingly, the computation time of the CHPP was approximately 5.7786×10^{-4} s on average, while that of the PF-only was approximately 5.7324×10^{-4} s, which varied to nearly zero.

Conclusions

We presented a cooperative hybrid path planning method that combines the PF with the sigmoid curve. In addition, to improve driving safety in emergency scenarios, we introduced the responsibility-sensitive safety model to enhance the performance of the hybrid path planning, which includes RSS-based speed planning. Furthermore, we proposed cooperative driving to calculate the desired coordinated speed for the cooperative adjacent vehicles when the traffic situation becomes urgent.



(a) Front tire steering angles of ego vehicle in dynamic scenario.

(b) Computation time of EHSPF-MPC, HSPF-MPC, and PF-MPC.

Figure 3.52: Front tire steering angles and computation time in the dynamic scenario.

3.4.3 Interactive speed optimization

Another concern is that the PFs used in autonomous vehicles focus solely on the path generation of the ego vehicle while assuming that the surrounding obstacle vehicles drive at a preset behavior without the PF-based path planner, which ignores the fact that the ego vehicle's PF could also impact the path generation of the obstacle vehicles. Therefore, in this subsection, we propose a unique interactive speed optimization (ISO), which has been published in [8], for PF-based path planning among connected autonomous vehicles equipped with V2V communication, as depicted in Fig. 3.53. The major contributions are concluded as follows.

- Introduce a piece-wise road potential function for the merging road where two lanes merge into one lane.
- Propose an interactive speed optimization (ISO) by solving a constrained objective function that considers driving safety, ride comfort, and the shared local path (SLP) from other connected autonomous vehicles.

Road potential function for merge roads

To accommodate merge roads, we adapted the potential function for the road edges using the following expression:

$$U_{RE} = \frac{1}{2}\xi(\frac{1}{Y - Y_{l,u} - l_w/2})^2, \tag{3.40}$$

where

$$Y_l = \begin{cases} Y_{bottom}, & if\ X < X_{merge}^{start} \\ k_{sl}X_{merge} + b, & if\ X_{merge}^{start} \leq X \leq X_{merge}^{end} \\ Y_{lane}, & if\ X > X_{merge}^{end} \end{cases}$$

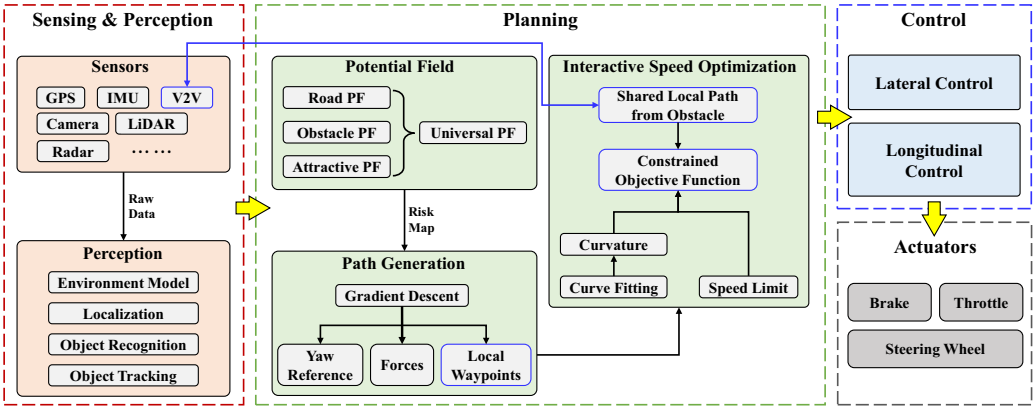


Figure 3.53: Overall system framework (Sensing & Perception, Communication, Planning, Control, and Actuators): Planning layer extracts the shared local path from V2V communication and then formulates a constrained objective function with proper analysis

with ξ denoting the scaling coefficient and $Y_{l,u}$ representing the lateral positions of the road edges, respectively. l_w is the vehicle's width, and Y_{bottom} denotes the lateral position of the first section of the road edge. k_{sl} is the slope, and b is the bias, which we assume the edge of the merge section can be approximated by the linear function. $X_{merge}^{start,\,end}$ means the longitudinal start and end of the merge part.

Interactive speed optimization

As mentioned, previous works assume that only the ego vehicle has the PF-based path planner while other autonomous vehicles drive along a preset path. While the path generation of the ego vehicle may meet expectations, the impact of the ego vehicle on other autonomous vehicles is often ignored or not discussed, depicted in Fig. 3.54. To consider the impact of other autonomous vehicles' PF, we propose an interactive speed optimization with the shared local path via V2V communication for cooperative driving. We have formulated an objective function with reasonable constraints to obtain the optimal speed. The proposed objective function consists of three terms,

which are shown below:

$$\min_{v_1,\cdots,v_h} w_1 \sum_{i=1}^{N} \frac{X_{pf}^{i+1} - X_{pf}^{i}}{v_i} + w_2 \sum_{i=1}^{N} \frac{1}{2}(v_i - V_{target})^2 + w_3 \sum_{i=1}^{N} \ln U_{SLP}^{i} \tag{3.41}$$

$$s.t.\ v_i \in [0,\ V_i^{max}], \tag{10a}$$

where

$$V_i^{max} = \min(V_{limit},\ \sqrt{\mu g/\kappa}),$$
$$\kappa = 6a_3 s + 2a_2 \approx 2a_2$$

with V_{target} denoting the preset target speed and V_{limit} indicating the speed limit on the highway. μ is the friction coefficient and g is the gravitational acceleration. κ is the path curvature, and s is the arc length. U_{SLP} represents the accumulative PF of the shared local path (SLP) from other autonomous vehicles via V2V communication. The calculation of U_{SLP} is slightly different from Eq. (3.3) that we use $(X_{pf}^{ego,i},\ Y_{pf}^{ego,i})$ and $(X_{pf}^{obs,i},\ Y_{pf}^{obs,i})$ from Eq. (2.13) instead of $(X,\ Y)$ and $(X_o,\ Y_o)$. Note that the number $i = 1, \cdots, N$ of the SLP depends on the preset number of iterations. Additionally, the first term of the objective function (10) evaluates the driving efficiency while tracking the local waypoints. The second term indicates the deviation from the target (reference) speed, while the last term ensures that the AV is aware of the intentions of surrounding vehicles by computing the PF of the SLP. Therefore, we can diminish the oscillations caused by the interactive effect of other autonomous vehicles' PFs. Regarding the communication network, we have designed the maneuver coordination (MC) protocol [MTE21] and established a systematic message broadcasting module to facilitate the exchange of anticipated paths among the vehicles [HTO+21] in our previous works. Therefore, in this study, we utilize the previous communication network, concentrating more on path generation and speed computation for connected autonomous vehicles.

Simulation results and analysis

We compared our proposed method with other PF-based path-planning algorithms in a merging scenario using MATLAB/Simulink. To simulate interaction, we assumed that all autonomous vehicles utilized the PF for local path planning. As shown in Fig. 3.55, there are two autonomous vehicles

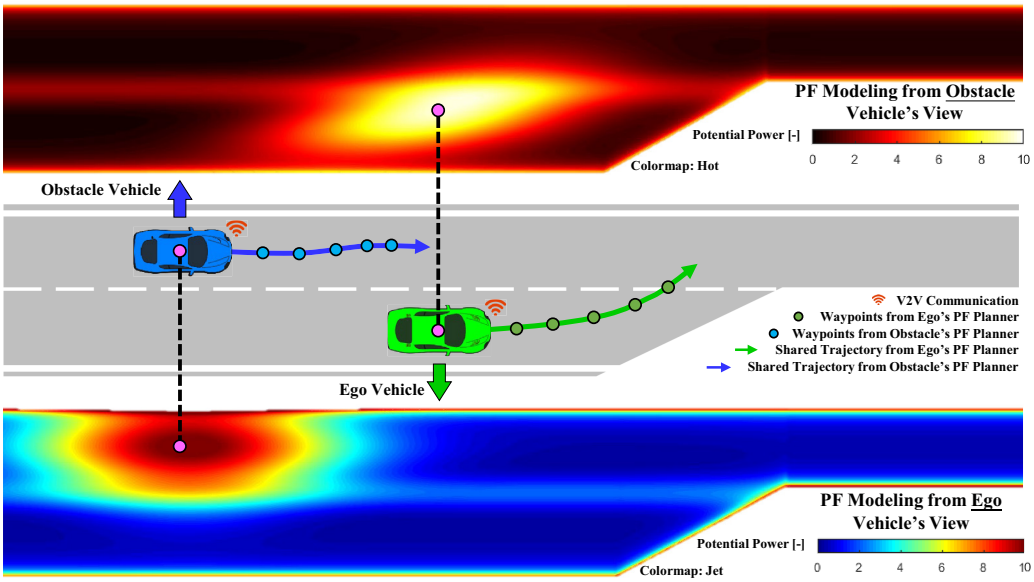


Figure 3.54: Merging scenario where the obstacle (blue) vehicle and the ego (green) vehicle apply the PF independently (Colormap: Hot for the blue vehicle and Colormap: Jet for the green vehicle). The paths depicted on the colormap are generated by the PF-only planner, while the paths denoted in the middle part are produced by the PF-ISO planner; the distance between the waypoints varies with speed

on a merging road. An obstacle vehicle drives at an initial speed of 15 m/s in the upper lane, while the ego vehicle with an initial speed of 20 m/s drives in the lower lane and needs to perform a merging maneuver. Note that we intentionally positioned the obstacle vehicle slightly ahead of the ego vehicle to simulate an urgent merging situation, which provides better observation of the paths of both vehicles. In addition, we denoted the following path planners for comparative study: i) PF-based planner with longitudinally constant speed (denoted as PF-CS) [WYZ+22]; ii) PF-based planner with speed planning (denoted as PF-SP) [WGL22]; ii) Proposed PF-based planner with interactive speed optimization (denoted as PF-ISO).

In Fig. 3.55, we can observe the generated paths of both the obstacle and ego vehicles from the three PF-based path planners. In the first subfigure of Fig. 3.55, we can see that the red path (obstacle vehicle) has a winding part from 167 m to 272 m with the PF-CS method, as circled in the ellipse when entering the merging zone (orange area). The winding part can also be observed in the ego vehicle's path (brown-purple dash line). Hence, we can

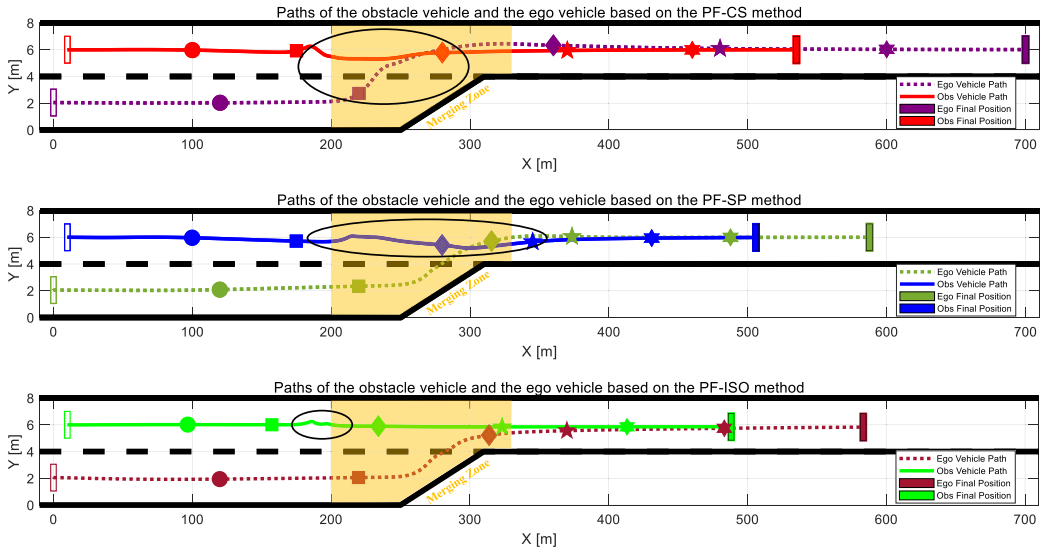
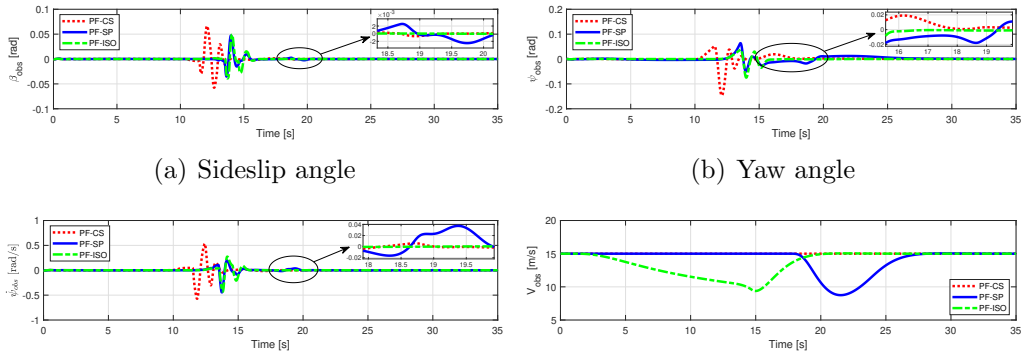


Figure 3.55: Paths of the obstacle and ego vehicles based on PF-CS, PF-SP, and PF-ISO, respectively

see that the sideslip angle, yaw angle, and yaw rate of the PF-CS planner have larger values than the other two planners, shown as the red dashed line in Figs. 3.56(a) to 3.56(c) (with a maximum of 0.07 rad in sideslip angle, -0.15° in yaw angle, and -0.57 rad/s in yaw rate). Conversely, the winding part is slightly decreased with the PF-SP planner for both the obstacle and ego vehicles' paths, as depicted in the second subfigure of Fig. 3.55 (blue solid and green dashed lines). However, it is still obvious that the obstacle vehicle has a serpentine part after the ego vehicle finishes the merging maneuver from 279 m to 345 m. Therefore, we can see a certain vibration in the sideslip angle, yaw angle, and yaw rate (blue solid line) from 18 s to 20 s in Figs. 3.56(a) to 3.56(c). In Fig. 3.56(d), we can also see the PF-SP planner reduces the speed by around 17.5 s which corresponds to the merging part at 255 m in the second subfigure of Fig. 3.55. In contrast, the PF-ISO planner starts to slow down gradually from 3.1 s to 14.9 s (from 15 m/s to 9.4 m/s) in Fig. 3.56(d) and then accelerates until reaching the target longitudinal speed. Furthermore, the motion states of the PF-ISO planner vary around zero, which indicates it is less affected by the interaction between the PFs during the merging procedure, as denoted in the partial magnifications of Figs. 3.56(a), 3.56(b), and 3.56(c). In addition, we can still observe a slight oscillation in the obstacle vehicle's path (solid green line) from 180 m to 196 m in the third subfigure of Fig. 3.55, which implicitly states the ego vehicle's



(a) Sideslip angle

(b) Yaw angle

(c) Yaw rate

(d) Longitudinal speed

Figure 3.56: Motion states of the obstacle vehicle based on PF-CS, PF-SP, and PF-ISO, respectively

PF continuously influences the obstacle vehicle's path generation. However, the influence is significantly reduced because the obstacle vehicle generally decelerates before closing to the merging part. It is worth noting that the path length of the PF-ISO is relatively shorter than that of the other two planners, which implies the PF-ISO method performs a pre-brake maneuver like human drivers.

Conclusions

In this subsection, we have introduced a unique PF-based path planning approach with the SLP path from other autonomous vehicles via V2V communication. We consider the interaction between the PFs of the autonomous vehicles on the road instead of assuming that only the ego AV uses the PF-based path planner. By formulating an objective function, we compute the optimal speed that implements the SLP as an optimized term, which also imposes reasonable constraints. The simulation results indicate that the proposed PF-ISO method can reduce the oscillations of the autonomous vehicles' sideslip and heading angles and produce a smoother path for both the obstacle and the ego vehicles under the interaction of other autonomous vehicles' PFs.

3.5 Summary

This chapter provides a comprehensive overview of path-planning strategies for both non-cooperative and cooperative autonomous vehicles (NAVs and

CAVs). In the realm of non-cooperative approaches, the Time-to-Collision-Aware Lane Change strategy employs the time-to-collision metric to ensure safe lane changes, while the Occlusion-Aware Collision Avoidance method focuses on preventing collisions with objects that are not visible due to occlusions. Additionally, the clothoid curve-based emergency stopping technique utilizes clothoid curves to facilitate efficient emergency stops. On the cooperative front, the Risk Assessment Index for Adaptive Potential Field dynamically adjusts path planning in response to environmental risks. The Event-Based Hybrid Planning with Sigmoid Curve approach integrates event detection into path planning, ensuring smooth transitions between segments. Lastly, the Interactive Speed Optimization for Lane Merge strategically controls vehicle speed to enable safer and more efficient lane merging, taking into account the movements of surrounding vehicles.

Chapter 4

Safety Tunnel-based Model Predictive Controller for Emergency Navigation

4.1 Introduction

Model Predictive Control (MPC) is a vital technique in autonomous driving for path tracking, offering a forward-looking strategy that ensures vehicles adhere to their intended paths [SMT+23]. Central to MPC is its ability to predict future vehicle states using a model of the vehicle's dynamics and kinematics. It constantly recalculates optimal control actions over a finite time horizon, taking into account current states, upcoming path requirements, and various constraints like vehicle capabilities and safety regulations. This process, known as the receding horizon approach, involves solving an optimization problem at each control step to minimize path deviation while considering factors like energy efficiency and passenger comfort. The MPC's adaptability to dynamic environments and its capacity to balance multiple objectives make it particularly effective, albeit computationally intensive, for navigating complex driving scenarios in real-time. This blend of predictive accuracy and responsiveness positions MPC as a cornerstone in the development of advanced autonomous vehicle control systems.

Primarily, MPC is computationally intensive, requiring substantial processing power for real-time decision-making, which can be challenging in the fast-paced driving environment. This computational demand limits its applicability in lower-end vehicles or systems where resources are constrained. Additionally, the effectiveness of MPC relies heavily on the accuracy of the vehicle and environment models it uses; inaccuracies in these models can

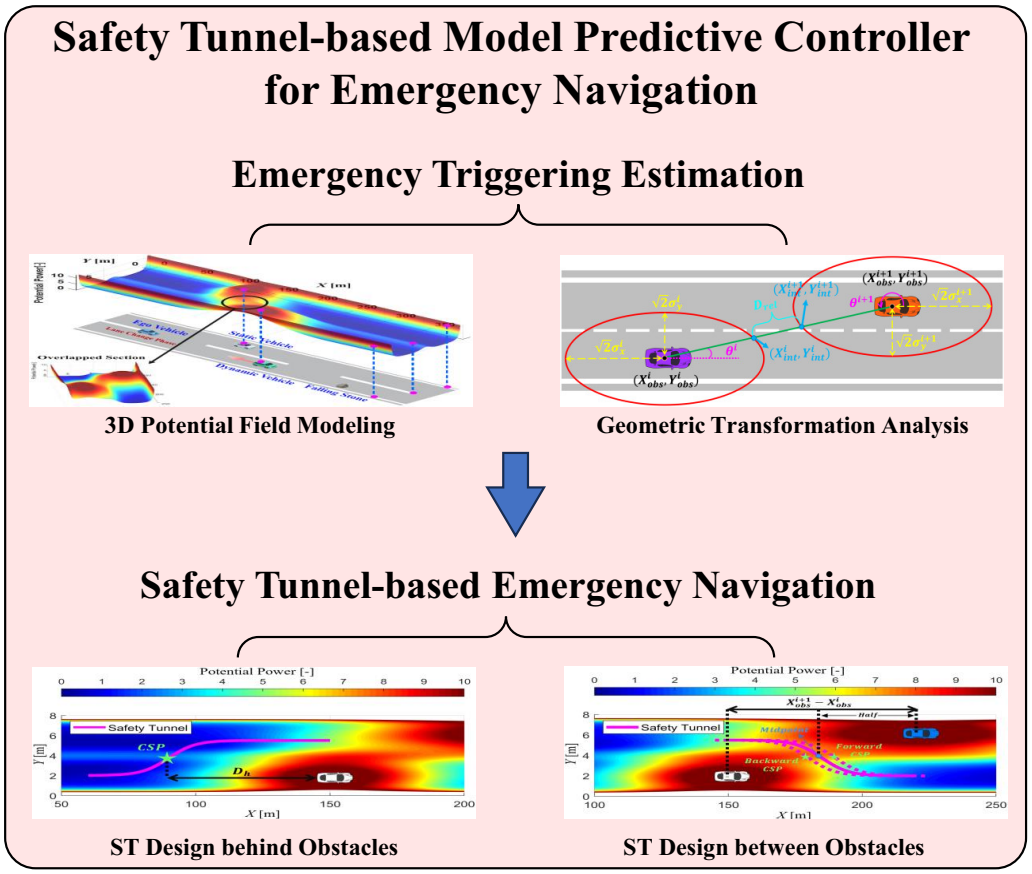


Figure 4.1: Overview of the safety tunnel-based model predictive controller

lead to suboptimal or unsafe driving decisions. Another challenge is the integration of MPC with rapidly changing, unpredictable real-world scenarios, where the dynamic nature of road conditions, traffic, and pedestrian behavior might exceed the predictive capability of the control model. Furthermore, the complexity of MPC algorithms can pose difficulties in terms of validation and verification, which are critical for ensuring safety in automotive applications. Thus, while MPC offers a forward-thinking approach to vehicle control, these challenges must be addressed to fully realize its potential in the autonomous driving landscape.

4.2 Overview

Fig. 4.1 illustrates the conceptual framework of a Safety Tunnel-based Model Predictive Controller (STMPC) for emergency navigation in autonomous vehicles. It outlines a two-tiered approach beginning with the estimation of emergency triggers that necessitate immediate vehicular response. This estimation integrates 3D potential field modeling to assess environmental risks and geometric transformation analysis to understand vehicle orientation and positioning.

The core of the system is the Safety Tunnel concept, which guides the vehicle through hazardous situations by creating a virtual safe passage. The upper part of the figure visualizes the safety tunnel's design process: behind and between obstacles, indicating the vehicle's strategic planning to maneuver safely. The lower part of the figure showcases two distinct applications of the safety tunnel—behind obstacles, where the vehicle must follow a safe path, and between obstacles, where it must navigate through narrow spaces.

The downward arrow emphasizes the flow from theoretical estimation to practical application, signifying the transition from high-level planning to detailed navigational tactics ensuring the vehicle's safe passage through imminent threats. This strategic framework is key for enhancing the autonomous vehicle's ability to make rapid and safe decisions in dynamic environments.

4.3 Vehicle motion modeling

The vehicle dynamics model is essential for accurately predicting future states and calculating optimal control inputs. These models range from simple kinematic models suitable for low-speed maneuvers to complex dynamic models that incorporate forces and inertia for high-speed precision. The MPC uses these models to simulate future vehicle behavior over a prediction horizon and optimizes control inputs to adhere to the desired path while respecting vehicle limitations and ensuring passenger comfort. The chosen model must strike a balance between accuracy and computational efficiency to enable real-time control adjustments in response to the driving environment.

The vehicle bicycle model is favored in the MPC for its optimal balance between simplicity and fidelity, offering a computationally efficient representation of vehicle dynamics suitable for real-time autonomous driving applications. It simplifies the four-wheel dynamics into two wheels, which is sufficient for capturing critical behaviors for a range of common maneuvers, thereby enabling faster optimization and control. This model's relative ease of implementation and calibration, coupled with its ability to provide an in-

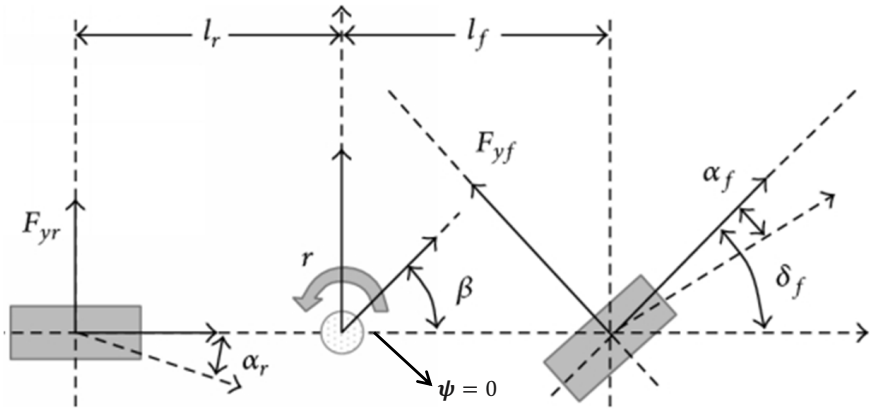


Figure 4.2: Vehicle lateral dynamics model [STJP06, FZM15]

tuitive understanding of vehicle handling, makes it a practical and versatile choice for MPC in autonomous vehicle systems. First, we can choose the following four variables as the vehicle motion states:

$$\mathbf{x}(k) = \begin{bmatrix} Y & \beta & \psi & \dot{\psi} \end{bmatrix}^T, \tag{4.1}$$

where Y is the lateral position of the vehicle, β denotes the vehicle sideslip angle, ψ is the yaw angle, and $\dot{\psi}$ is the yaw rate. The vehicle lateral dynamics can be summarized as follows:

$$mV(\dot{\beta} + \dot{\psi}) = F_{yf} + F_{yr}, \tag{4.2}$$

$$I_z\ddot{\psi} = l_f F_{yf} + l_r F_{yr}, \tag{4.3}$$

where m is the vehicle mass, V is the longitudinal speed, which is assumed to be constant, I_z denotes the vehicle moment of inertia, F_{yf} and F_{yr} are the front and rear tire forces, respectively, and l_f and l_r are the longitudinal distances from the center of gravity of the vehicle to its front and rear wheels, respectively. According to [Raj11, pp. 398–430], F_{xf} and F_{xr} can be approximated by the Magic Formula; then defined as:

$$F_{yf} = C_f\alpha_f = C_f(\delta_f - \beta - \frac{l_f\dot{\psi}}{V}), \tag{4.4}$$

$$F_{yr} = C_r\alpha_r = C_r(-\beta + \frac{l_r\dot{\psi}}{V}), \tag{4.5}$$

Then, upon substituting Equations (4.4) and (4.5) into Equations (4.2) and

(4.3), the lateral and yaw dynamics can be described as:

$$\dot{\beta} = \frac{-(C_r + C_f)}{mV}\beta + (\frac{C_r l_r - C_f l_f}{mV^2} - 1)\dot{\psi} + \frac{C_f}{mV}\delta_f, \tag{4.6}$$

$$\ddot{\psi} = \frac{C_r l_r - C_f l_f}{I_z}\beta + (\frac{C_r l_r^2 + C_f l_f^2}{I_z V}\dot{\psi} + \frac{C_f l_f}{I_z}\delta_f. \tag{4.7}$$

where C_f and C_r are the front and rear wheel cornering stiffness, respectively. I_z is the yaw moment of inertia and m means the total vehicle mass. With a control sampling period T, discretization using a zero-order hold (ZOH) equivalence sampling rate of $1/T$ yields the discrete-time linear vehicle model with the control input δ_f for the MPC design, which can be expressed as:

$$\mathbf{x}(k+1) = \Phi\mathbf{x}(k) + \Gamma u(k) \tag{4.8}$$

$$\mathbf{y}(k) = C\mathbf{x}(k) \tag{4.9}$$

where

$$\Phi = \begin{bmatrix} 1 & TV & TV & 0 \\ 0 & -\frac{(C_r+C_f)T}{mV} + 1 & 0 & \frac{(C_r l_r - C_f l_f)T}{mV^2} - T \\ 0 & 0 & 1 & T \\ 0 & \frac{C_r l_r - C_f l_f}{I_z}T & 0 & -\frac{C_r l_r^2 + C_f l_f^2}{I_z V}T + 1 \end{bmatrix},$$

$$\Gamma = \begin{bmatrix} 0 & \frac{C_f}{mV}T & 0 & \frac{C_f l_f}{I_z}T \end{bmatrix}^T, \quad C = \begin{bmatrix} 1 & 0 & 0 & 0 \\ 0 & 0 & 1 & 0 \end{bmatrix}.$$

4.4 Model predictive controller

The critical components of an MPC controller include a prediction model that captures the behavior of the system over a future time horizon, an optimizer that computes control inputs by solving an optimization problem at each control interval, and a set of constraints that the system must adhere to, which can encompass physical limitations and safety requirements. Additionally, MPC incorporates a cost function that seeks to minimize, reflecting goals such as energy efficiency, ride comfort, or tracking accuracy.

4.4.1 Future prediction of model outputs

First, the model described in Section 4.3 is transferred into an incremental model because the constraints on the control increment must be considered. The new state is then defined as

$$\mathbf{x}_n = \begin{bmatrix} \Delta\mathbf{x}(k) & \mathbf{y}(k) \end{bmatrix}^T \tag{4.10}$$

where $\Delta\mathbf{x}(k) = \mathbf{x}(k) - \mathbf{x}(k-1)$. Combining Eq. (4.10) with Eqs (4.8) and (4.9), the new discrete state-space model becomes

$$\mathbf{x}_n(k+1) = \Phi_n \mathbf{x}_n(k) + \Gamma_n \Delta u(k) \tag{4.11}$$

$$\mathbf{y}_n(k) = C_n \mathbf{x}_n(k) \tag{4.12}$$

where

$$\Phi_n = \begin{bmatrix} \Phi & Z_n \\ C\Phi & I_n \end{bmatrix}, \Gamma_n = \begin{bmatrix} \Gamma \\ C\Gamma \end{bmatrix}, C_n = \begin{bmatrix} Z_n \\ I_n \end{bmatrix}^T,$$
$$Z_n = \mathbf{0}_{4\times 2},\ I_n = \mathbf{1}_{2\times 2}.$$

Therefore, the future state of the vehicle can be predicted at each time step, given the current measured information $\mathbf{x}_n(k)$:

$$\mathbf{x}_n(k), \cdots, \mathbf{x}_n(k+n), \cdots, \mathbf{x}_n(k+N_p)$$

where N_p is the prediction horizon. The sequence of future control inputs is denoted by

$$\Delta U(k) = \left[\Delta u(k), \cdots, \Delta u(k+m), \cdots, \Delta u(k+N_c-1)\right]$$

where N_c is the control horizon. The derivation of the iterative prediction (shortened because of space limitations) is

$$\Xi(k) = \Theta \mathbf{x}_n(k) + \Upsilon \Delta U(k) \tag{4.13}$$

where

$$\Xi(k) = \begin{bmatrix} \mathbf{y}_n(k+1) & \mathbf{y}_n(k+2) & \cdots & \mathbf{y}_n(k+N_p) \end{bmatrix}^T_{N_p\times 1},$$
$$\Theta = \begin{bmatrix} C_n\Phi_n & C_n\Phi_n^2 & C_n\Phi_n^3 & \cdots & C_n\Phi_n^{N_p} \end{bmatrix}^T_{2N_p\times 6},$$
$$\Upsilon = \begin{bmatrix} C_n & 0 & \cdots & 0 \\ C_n\Phi_n\Gamma_n & C_n\Gamma_n & \cdots & 0 \\ \vdots & \vdots & \ddots & \vdots \\ C_n\Phi_n^{N_c-1}\Gamma_n & C_n\Phi_n^{N_c-2}\Gamma_n & \cdots & C_n\Gamma_n \\ C_n\Phi_n^{N_c}\Gamma_n & C_n\Phi_n^{N_c-1}\Gamma_n & \cdots & C_n\Phi_n\Gamma_n \\ \vdots & \vdots & \ddots & \vdots \\ C_n\Phi_n^{N_p-1}\Gamma_n & C_n\Phi_n^{N_p-2}\Gamma_n & \cdots & C_n\Phi_n^{N_p-N_c-1}\Gamma_n \end{bmatrix}_{2N_p\times N_c}.$$

Therefore, we can get the prediction about the future outputs with a given horizon N_p.

4.4.2 Constraints design

The general MPC formulation is normally observed to impose constant constraints on the motion states, control input, and control input increment, which can then be expressed as

$$-F_c\Delta u_{max} \leq \Delta U \leq F_c\Delta u_{max}, \tag{4.14}$$

$$-F_c(u_{max} + u(k-1)) \leq S_c\Delta U \leq F_c(u_{max} - u(k-1)), \tag{4.15}$$

$$T_c\Xi_{min} \leq \Xi \leq T_c\Xi_{max}, \tag{4.16}$$

where

$$F_c = \begin{bmatrix} 1 \\ 1 \\ \vdots \\ 1 \end{bmatrix}_{N_c \times 1}, \quad S_c = \begin{bmatrix} 1 & 0 & \cdots & 0 \\ 1 & 1 & \cdots & 0 \\ \vdots & \vdots & \ddots & \vdots \\ 1 & 1 & \cdots & 1 \end{bmatrix}_{N_c \times N_c},$$

$$T_c = \begin{bmatrix} 1 & 0 & 1 & 0 & \cdots & 1 & 0 & 1 & 0 \\ 0 & 1 & 0 & 1 & \cdots & 0 & 1 & 0 & 1 \end{bmatrix}_{2N_p \times 2}.$$

An important premise exists for the current constraint design that ensures that the PF-based path-planning module can only be assumed to work in standard driving cases. The constraint design must also consider traffic emergencies if the planning layer malfunctions, which will be explained in Section 4.5.

4.4.3 Objective function design

The objective function of the MPC is designed to reflect the goals of the MPC application, such as minimizing deviations from a set path, reducing fuel consumption, or ensuring passenger comfort. The function typically includes terms for tracking performance, control effort, and sometimes penalties for state and control deviations. In the context of autonomous vehicles, the objective function might combine terms for the distance to the target path, the smoothness of the steering actions, and the maintenance of a safe distance from other vehicles. The MPC optimizes this function over a future time horizon, subject to the vehicle dynamics and constraints, to determine the control inputs that will steer the system towards these goals most efficiently. Therefore, the objective function's design is tailored to prioritize certain aspects of the vehicle's performance, balancing trade-offs between competing objectives. Therefore, the cost function can be formulated as

$$J(\mathbf{x}_n(k), \Delta U(k)) = \|\Xi_{ref}(k) - \Xi(k)\|_Q^2 + \|\Delta U(k)\|_R^2 \tag{4.17}$$

where $\Xi_{ref}(k) = \begin{bmatrix}\mathbf{y}_{ref}(k+1) & \cdots & \mathbf{y}_{ref}(k+N_p)\end{bmatrix}^T_{N_p\times 1}$ and $\mathbf{y}_{ref}(k+1) = \begin{bmatrix}Y_{PF}(k+1) & \psi_{PF}(k+1)\end{bmatrix}^T$ are the reference signals obtained in Section III, and Q and R are weighting matrices. Eq. (4.17) is then transformed into a quadratic programming problem to reduce computational time while combining it with vehicle dynamics (4.11)–(4.12) and constraints (4.14)–(4.16); the resulting expression is rearranged as

$$
\begin{aligned}
min\, J \;=\; & \min_{\Delta U} \frac{1}{2}\Delta U(k)^T H \Delta U(k) + \Delta U(k)^T f && (4.18)\\
\text{s.t.}\quad & \mathbf{x}_n(k+1) = \Phi_n \mathbf{x}_n(k) + \Gamma_n \Delta u(k), && (4.18a)\\
& \mathbf{y}_n(k) = C_n \mathbf{x}_n(k), && (4.18b)\\
& -F_c \Delta u_{max} \le \Delta U \le F_c \Delta u_{max}, && (4.18c)\\
& T_c \Xi_{min} \le \Xi \le T_c \Xi_{max}, && (4.18d)\\
& -F_c(u_{max} + u(k-1)) \le S_c \Delta U \le F_c(u_{max} - u(k-1)), && (4.18e)
\end{aligned}
$$

where

$$
\begin{aligned}
& H = 2(\Upsilon^T \tilde{Q} \Upsilon + \tilde{R}), \quad f = -2(\Xi_{ref}(k) - \Xi(k))^T \Upsilon,\\
& \tilde{Q} = \text{diag}\left(\{Q_i\}_0^{N_p-1}\right), \text{ and } \tilde{R} = \text{diag}\left(\{R_i\}_0^{N_c-1}\right).
\end{aligned}
$$

With the aforementioned objective function, we can calculate a set of optimal control signals and send them to the vehicle actuators to maneuver the steering, brakes, and throttle. However, there exists an important premise for a constraint design that ensures that the PF-based path-planning module can only be assumed to work in normal driving cases.

4.5 Emergency triggering estimation

Let's consider an emergency obstacle avoidance scenario in which we assume that the collision can only be avoided by steering instead of braking. Assume that there are two obstacle vehicles on the highway: the first one in the same lane as the ego-vehicle is stopped because of an engine failure, and the other is driving at a constant speed in the adjacent lane. The ego vehicle needs to steer to avoid the first static obstacle, but the second dynamic obstacle vehicle suddenly decelerates due to an unexpected accident. This sudden deceleration will cause the obstacle's potential field to enlarge sharply in the longitudinal direction; this field would then partially overlap with the potential fields of the other vehicles. The gradient then varies abnormally, and the performance of the PFs will become unstable, as the path generated by

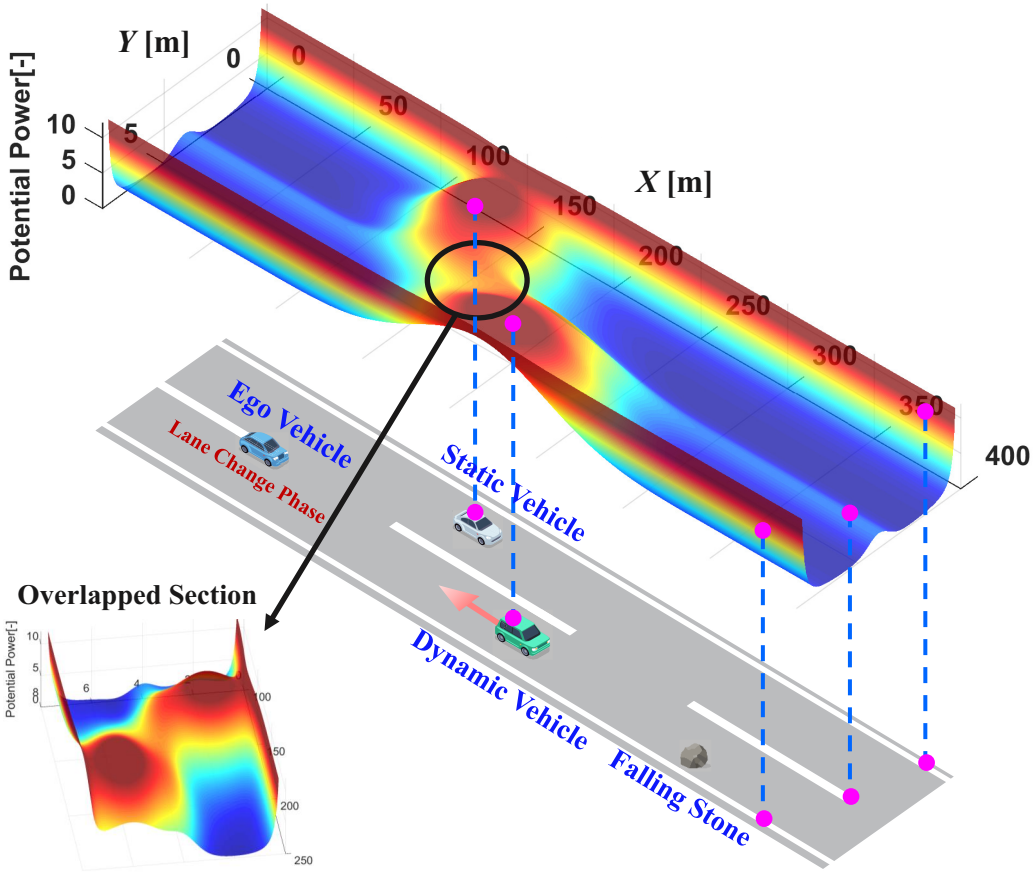


Figure 4.3: 3D figure of the road's potential field in an emergency situation. Dynamic vehicle (bright green) decelerates suddenly (denoted as the red arrow) due to the unexpected falling stone when the ego-vehicle (blue) is in lane-changing phase

PFs mainly depends on the gradient descent direction, as mentioned earlier. Besides, the sudden cut-in behavior of adjacent vehicles also sequentially leads to the overlapping problem of potential fields, causing unsatisfactory performance of the ego vehicle, as depicted in Fig.4.3.

To anticipate and monitor the above circumstances, we propose a concise algorithm called emergency triggering estimation published in [1] to judge whether there is an overlap between the potential fields of the obstacle vehicles. As shown in Fig. 4.4, we obtain a two-dimensional elliptic potential field by projecting the three-dimensional potential field of the obstacle vehicle onto the X-Y plane to simplify the analysis. From Eq. (3.32), we see that the projection of the potential field of the i^{th} obstacle vehicle (X^i_{obs}, Y^i_{obs})

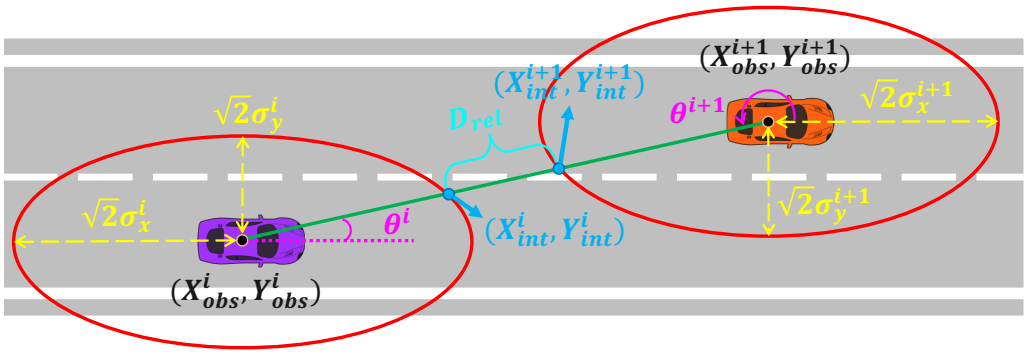


Figure 4.4: Triggering analysis of the potential fields of the obstacle vehicles to determine whether a narrow passage is produced

along the Z-axis is a quasi-standard ellipse, where the long and short half-axes are $\sqrt{2}\sigma_x^i$ and $\sqrt{2}\sigma_y^i$, respectively. The ellipse of the $(i+1)^{th}$ obstacle vehicle $(X_{obs}^{i+1}, Y_{obs}^{i+1})$ can be obtained in the same manner, with $\sqrt{2}\sigma_x^{i+1}$ and $\sqrt{2}\sigma_y^{i+1}$ as the long and short half-axes, respectively. According to [SR12], the minimum distance D_{rel} between two ellipses can be calculated using the Euclidean distance and Lagrange multiplier to obtain the approximate solution with the conditions for an extremum. However, the computational cost of this method is extremely high. [ZPM07] provides a full analysis of the distance of two arbitrary ellipses in the two-dimensional plane; it is considered that when the two ellipses are oriented in the same direction, the connecting line between the centers of the ellipses intersects with the edges of the ellipses to produce two intersection points. Then, D_{rel} can be approximated by the distance between the two intersection points, as shown in Fig. 4.4. Next, to calculate D_{rel}, it is necessary to obtain the coordinate values of the two intersection points from the two ellipses that intersect with a line connecting the centers of them, denoted as (X_{int}^i, Y_{int}^i) and $(X_{int}^{i+1}, Y_{int}^{i+1})$ in Fig. 4.4. According to the properties of the elliptic equation, we can obtain the following equations:

$$\begin{cases} \frac{(X_{int}^i - X_{obs}^i)^2}{2(\sigma_x^i)^2} + \frac{(Y_{int}^i - Y_{obs}^i)^2}{2(\sigma_y^i)^2} = 1 \\ \tan\theta^i = \frac{Y_{int}^i - Y_{obs}^i}{X_{int}^i - X_{obs}^i} \end{cases} \tag{4.19}$$

where θ^i is the angle between the intersection point (X_{int}^i, Y_{int}^i) and the long half-axis of the ellipse. The second equation can be substituted into the first

Algorithm 3 Triggering Estimation on SP Constraint

Initialization:$(X^i_{int}, Y^i_{int}), (X^{i+1}_{int}, Y^{i+1}_{int}) \leftarrow (0, 0)$
$T_{SP} \leftarrow$ **false**
repeat
  Update σ^i_x, σ^i_y based on Equation (3.32)
  Update θ^i based on Equation (4.22)
  Update X^i_{int}, Y^i_{int} based on Equation (4.21)
  $\theta^{i+1} \leftarrow \theta^i + \pi$
  Update $X^{i+1}_{int}, Y^{i+1}_{int}$ based on Equation (4.21)
  Update D_{rel} based on Equation (4.23)
  if $D_{rel} \leq D_{thold}$ **then**
    $T_{SP} \leftarrow$ **true**
    Compute safety tunnel F_{ST}
    Constraint including $F_{ST} \leftarrow$ on
    Minimize Equation (4.18)
  else
    Minimize Equation (4.18) without F_{ST}
  end if
until $\sqrt{(X - X_{goal})^2 + (Y - Y_{goal})^2} \leq d^*$

Output: triggering signals $\{T_{SP}, D_{rel}\}$

equation for the solution:

$$(X^i_{int} - X^i_{obs})^2 = \frac{2(\sigma^i_x \sigma^i_y)^2}{(\sigma^i_y)^2 + (\sigma^i_x)^2 \tan^2 \theta^i} \tag{4.20}$$

Then, considering $\theta \in (0, \frac{\pi}{2})$, we can obtain the coordinate value of (X^i_{int}, Y^i_{int}) as follows:

$$\begin{cases} X^i_{int} = \frac{\sqrt{2}\sigma^i_x \sigma^i_y}{\sqrt{\sigma^2_y + \sigma^2_x \tan^2 \theta^i}} + X^i_{obs} \\ Y^i_{int} = \frac{\sqrt{2}\sigma^i_x \sigma^i_y \tan \theta^i}{\sqrt{(\sigma^i_y)^2 + (\sigma^i_x)^2 \tan^2 \theta^i}} + Y^i_{obs} \end{cases} \tag{4.21}$$

It is important to note that $\tan \theta^i$ can be calculated using the positions of the obstacle vehicles:

$$\tan \theta^i = \frac{Y^{i+1}_{obs} - Y^i_{obs}}{X^{i+1}_{obs} - X^i_{obs}} \tag{4.22}$$

The position information of the obstacle vehicles can be accessed from on-board sensors. Therefore, we can substitute Equation (4.22) into Equation (4.21) to obtain the numerical value of (X^i_{int}, Y^i_{int}). We can use the same method to obtain the solutions of $(X^{i+1}_{int}, Y^{i+1}_{int})$. However, it must be noted

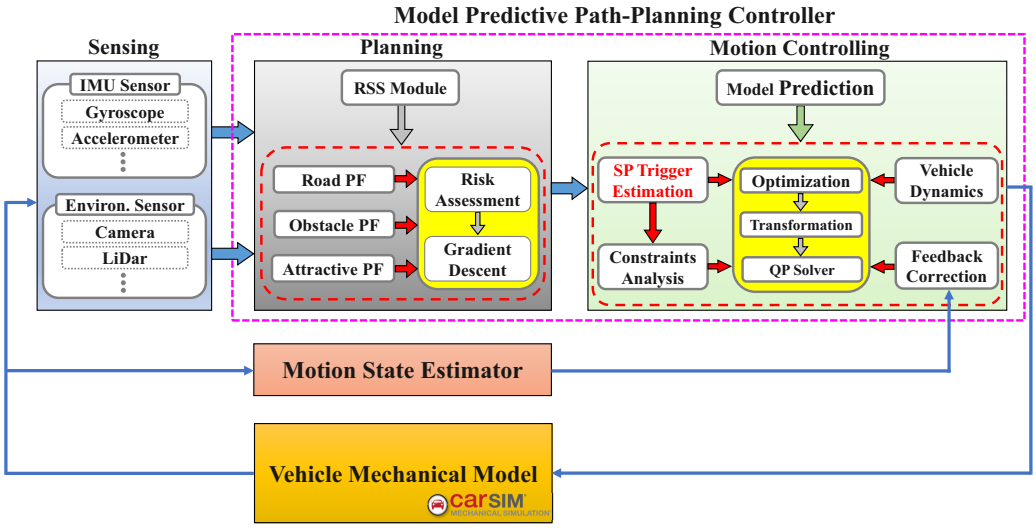


Figure 4.5: Overall framework of model predictive path-planning system with the emergency triggering estimation.

that $\theta^{i+1} \in (\pi, \frac{3\pi}{2})$, which leads to a negative value for $\tan\theta^{i+1}$. Finally, we can calculate D_{rel}:

$$D_{rel} = \sqrt{(Y_{int}^{i+1} - Y_{int}^{i})^2 + (X_{int}^{i+1} - X_{int}^{i})^2} \tag{4.23}$$

Therefore, based on Equation (4.23), we can compute an algorithm (Algorithm 3) to determine if a narrow passage exists when traffic emergencies occur, such that the safety tunnel constraint F_{ST}, which will be introduced in the next section, should be triggered to guarantee safety. In the initialization, the triggering flag T_{SP} of the SP constraint is set as false. Subsequently, we monitor D_{rel}. If D_{ref} is less than the preset safety distance threshold D_{thold}, we set T_{SP} to true and minimize Equation (4.18) under the SP constraint. Algorithm 3 stops compiling if the ego-vehicle (X, Y) reaches the goal position (X_{goal}, Y_{goal}) within a certain range of d^*. Therefore, Algorithm 3 is implemented in the safe passage (SP) trigger estimation sub-module, as shown in Fig. 4.5 that outlines the model predictive path-planning controller, comprising a sensing module for environmental data acquisition, a planning module that uses the PF for path determination, and a motion controlling module for executing the driving strategy. Integrated with a Motion State Estimator and the CarSim mechanical model, it ensures accurate real-time responses and safe navigation decisions for autonomous driving.

4.6 Safety tunnel for emergency navigation

To improve the safety of the ego vehicle in the aforementioned scenario, we have developed a novel safety tunnel (ST) using a sigmoid-like function. This function has been incorporated into the lateral position constraint design of the MPC. The work detailed in this section has been published in [2]. This function was chosen because it can calculate the upper and lower boundaries of ST relatively and smoothly with the given position information of the ego and obstacle vehicle at each time step, as expressed below:

$$F_{ST}(X) = \frac{W_S}{1 + exp[\rho(X^i_{obs} - X) - S_x]} + S_y, \tag{4.24}$$

where W_S is the width of the sigmoid function, ρ is the slope of the sigmoid function at the central symmetry point (CSP), S_x and S_y are the parameters related to the longitudinal and lateral position of the starting point of the lane change, respectively, $i = 1, \cdots, M$ is the superscript index of the i^{th} obstacle and M denotes the number of obstacles. The calculation of the ST parameters is as follows:

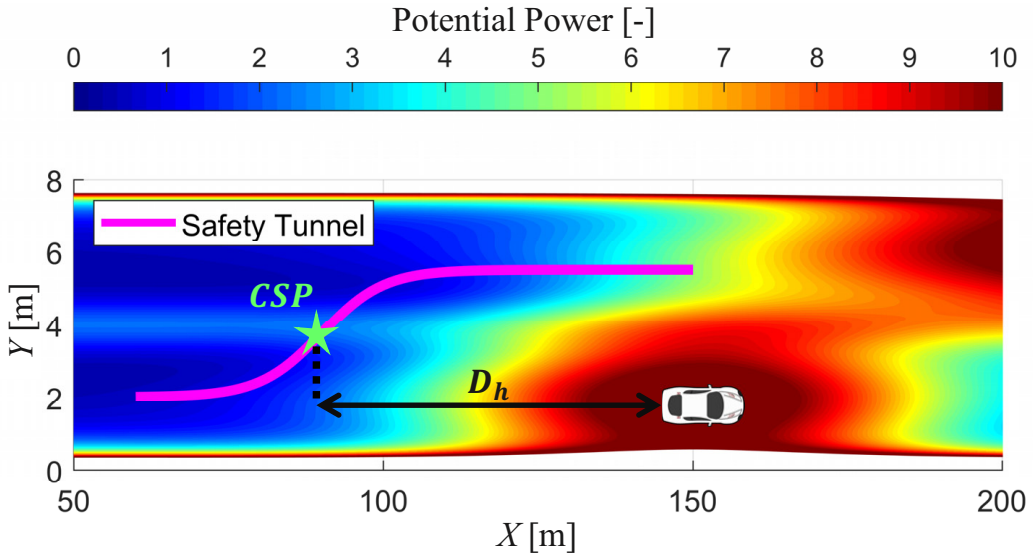
$$S_x = \begin{cases} \rho D_h & , X \notin (X^i_{obs}, X^{i+1}_{obs}) \\ \frac{\rho(X^{i+1}_{obs} - X^i_{obs})}{2} + sgn(\Lambda)|\Lambda|T_s & , X \in [X^i_{obs}, X^{i+1}_{obs}], \end{cases} \tag{4.25}$$

$$S_y = Y_c + (-1)^j \frac{W_L}{2}, \tag{4.26}$$

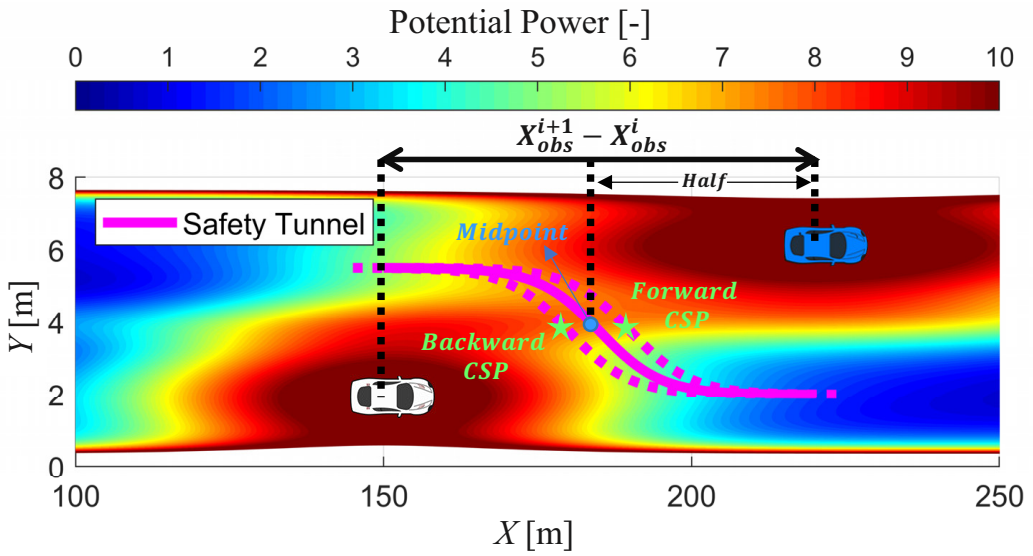
$$W_S = (-1)^{j+1}(W_L - \epsilon), \tag{4.27}$$

$$\rho = \max\left(\frac{d^{long}_{min}}{X^i_{obs} - X}, \rho_{cont}\right), \tag{4.28}$$

with $j = 1, \cdots, N$ indicates the j^{th} lane change. For example, in Fig. 5(a), we say the ego vehicle is to conduct the first lane-change behavior ($j = 1$) from the lower lane to the upper lane. So, we substitute $j = 1$ into Eqs. (21) and (22) to get a sigmoid curve that can lead the vehicle from the lower lane to the upper lane. Then, in Fig. 5(b), we say the ego vehicle is to conduct the second lane-change behavior ($j = 2$) from the upper lane to the lower lane so that we use $j = 2$ to calculate the proper sigmoid curve. Analogously, we say that the ego vehicle is to conduct the N^{th} lane-change behavior at time t ($t \neq 0$), and then we repeat the above steps. Λ denotes the longitudinal speed difference between obstacle vehicles, W_L is the lane width, and $\epsilon \in [0.1, 0.5]$ is a positive slack factor indicating the ST width, ρ_{cont} denotes the constraint of ρ. When implementing the proposed ST into the MPC constraints, the parameters can be calculated based on the sensing information from the current driving



(a) ST design when not between the surrounding obstacles



(b) ST design when between the surrounding obstacles

Figure 4.6: ST design based on emergencies: (a) The longitudinal position of CST is determined by D_h and ρ; (b) The longitudinal position of CST is determined by the obstacles' positions and relative speeds

environment, not requiring tedious manual adjustment. Eq. (4.25) represents that when there is only one obstacle around the ego-vehicle, the longitudinal position of the central symmetric point of the sigmoid function is equal to

the braking distance D_h, calculated from section III. Hence, the lane change behavior can be taken earlier, as depicted in Fig. 4.6(a). However, when the vehicle's position is between the obstacle vehicles, the longitudinal position of the central symmetric point should shift around the midpoint between the obstacle vehicles according to their relative position and speed, i.e., if V_{obs}^{i} is faster than V_{obs}^{i+1}, the CSP should shift forward based on the midpoint (Forward CSP), as illustrated in Fig. 4.6(b). The ST can then be created by shifting equation (4.24) within a certain range ϵ (depending on the urgency of the traffic situation):

$$F_{ST}^{lb} = F_{ST} - \epsilon, \quad F_{ST}^{ub} = F_{ST} + \epsilon. \tag{4.29}$$

where F_{ST}^{lb} and F_{ST}^{ub} are the lower and upper boundary of the ST, respectively. We then embed this ST into the MPC constraints shown in Eq. (3.20a) and get the final form of the objective function based on Eq. (4.18):

$$\begin{aligned}
\min_{\Delta\tilde{\mathbf{u}}} \quad & J(\Delta\tilde{\mathbf{u}}(k), \mathbf{y}_e(k)) && (4.30)\\
\text{s.t.} \quad & \mathbf{x}(k+1) = \mathbf{\Phi}\mathbf{x}(k) + \mathbf{\Gamma}u(k), && (4.30a)\\
& \mathbf{y}(k) = \mathbf{C}\mathbf{x}(k), && (4.30b)\\
& \mathbf{G}\Delta\tilde{\mathbf{u}}(k) \leq \mathbf{b}, && (4.30c)\\
& \Delta\mathbf{u}(k) = \mathbf{u}(k) - \mathbf{u}(k-1), && (4.30d)\\
& Y_{min,k} \leq Y(k) \leq Y_{max,k}, && (4.30e)
\end{aligned}$$

where

$$Y_{min,k} = F_{ST}^{lb,k}, \quad Y_{max,k} = \begin{cases} Y_c + \frac{W_L}{2} + \epsilon & , X \notin (X_{obs}^{i}, X_{obs}^{i+1}) \\ F_{ST}^{ub,\,k} & , X \in (X_{obs}^{i}, X_{obs}^{i+1}). \end{cases}$$

Note that the constraint Eq. (4.30e) is compiled only when the PFs cannot plan a safe-steady path due to an emergency, e.g., emergency braking and lane-changing obstacles.

4.7 Simulation and results

In this section, the general experimental settings are introduced in detail, and three comparative simulation scenarios are compiled to evaluate the performance of the proposed PF-STMPC method in emergency avoidance, compared with the conventional MPC from [WGW21] (denoted as PF-CMPC).

Table 4.1: Parameters of the MPC controller

$Parm.$	$Val.$	$Parm.$	$Val.$
N_p	20	N_c	5
T_s	10 ms	u_{max}	10°
Δu_{max}	0.85°	ψ_{max}	0.4 rad
V	20 m/s	ϵ	0.15 m
ρ_{cont}	0.15	W_L	4 m
Q	$\begin{bmatrix} 0.01 & 0 \\ 0 & 0.001 \end{bmatrix}$	R	0.1

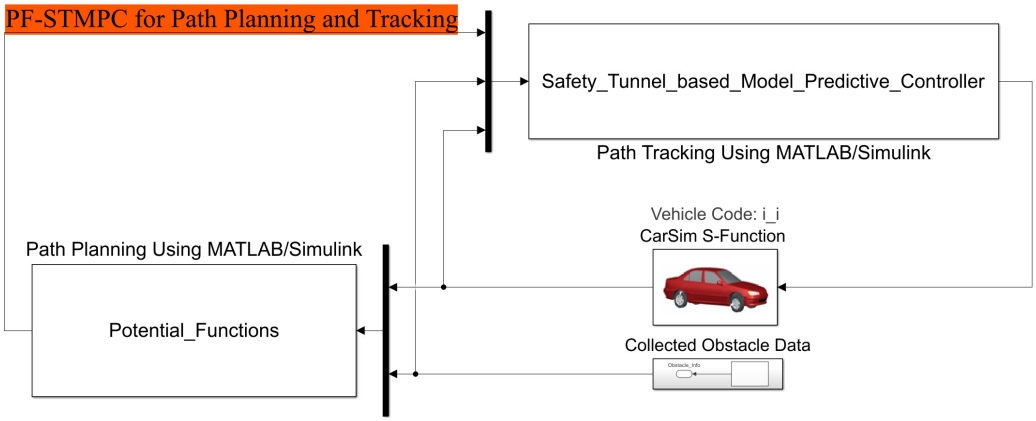


Figure 4.7: Co-simulation framework: Path planning and tracking algorithms are conducted in MATLAB/Simulink; Control signals are evaluated in CarSim Simulator

4.7.1 Settings

The setting of the relevant parameters of the MPC controller is shown in Table 4.1. The numerical values of ρ and ϵ are experimentally determined and are mainly related to the chosen vehicle model and the degree of traffic emergency. For example, at the same speed, cars are more accessible to pass through the route with large curvature than trucks. Therefore, ρ_{cont} for cars can be larger than that of trucks. ϵ mainly depends on the intersection degree of obstacles' potential fields; for example, the greater the degree of potential fields intersect, the smaller the value of ϵ. The other parameters of the vehicle bicycle model can be inferred from [FZM15]. The overall system framework has been co-simulated via MATLAB/Simulink and CarSim Simulator, which is dedicated in Fig. 4.7.

4.7.2 Emergency scenarios

For validating the performance of the proposed PF-STMPC algorithm, two relatively dangerous obstacle avoidance scenarios are simulated and compared with the PF-CMPC under the assumption that collision can only be avoided by steering instead of braking. Note that β is a vital index considering vehicle body stability and is derived empirically to calculate the suggested range of β for driving at different types of roads [Raj11].

$$\beta_{bound} = \arctan(0.02\mu g), \tag{4.31}$$

where μ is the friction coefficient, and g is the gravitational acceleration.

The first emergency scenario considers a single dynamic obstacle in the same lane as the ego-vehicle with the initial position set to $(X_{obs}, Y_{obs}) = (130, 2)$. The obstacle moves at 12 m/s in the first 10 s of simulation and then suddenly decelerates to 4 m/s^2 because of the emergency. The obstacle is set to decelerate after 10 s from the simulation start because the ego-vehicle is in the process of lane change at this time. In addition, this is the period when crashes are most likely to happen if the surrounding vehicles have abnormal acceleration/deceleration or steering [Wan94]. The general settings are depicted in Fig. 4.8.

The third traffic emergency considers a three-lane road where the first dynamic obstacle is set in the first lane with an initial position $(X^1_{obs}, Y^1_{obs}) = (50, 2)$ and the second dynamic obstacle is in the third lane with an initial position $(X^1_{obs}, Y^1_{obs}) = (50, 10)$. The ego-vehicle stays in the mid-lane. The first obstacle moves at 12 m/s and maintains lane-keeping behavior at all times. The second obstacle moves at 15 m/s in the beginning 6 s and then suddenly changes its lane to the mid lane without an early warning to avoid an unexpected falling stone.

4.7.3 Results and analysis

Scenario I

The simulation results of scenario I are presented from Fig. 4.8 to Fig. 4.10(d). Fig. 4.8 shows that both the PF-STMPC (depicted by the solid green line) and PF-CMPC (red dot-solid line) could avoid the dynamic obstacle successfully. However, the trajectory of PF-CMPC computed without the ST constraints (magenta dash line) is steeper than that of PF-STMPC when the front obstacle decelerates suddenly. The variation of the obstacle's potential field during deceleration is depicted in Fig. 4.9 where the range of the potential field expands rapidly in a short time of approximately 2 s.

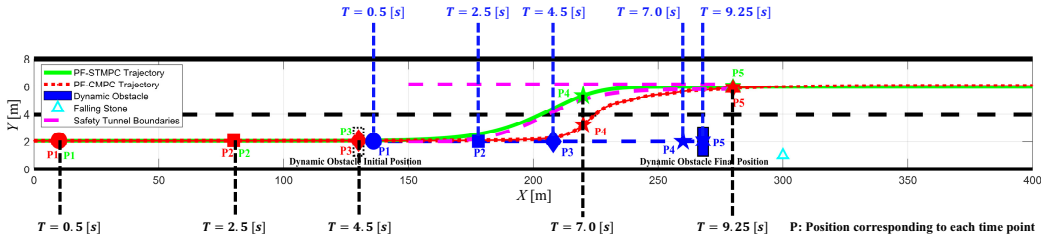


Figure 4.8: Comparative study of vehicle trajectories: front dynamic obstacle decelerates during the lane-change phase (blue dotted line) due to the falling stones (cyan triangle); PF-STMPC trajectory (solid green line) under safety tunnel boundaries (dotted magenta line) is smoother than that of PF-CMPC (dotted-solid red line)

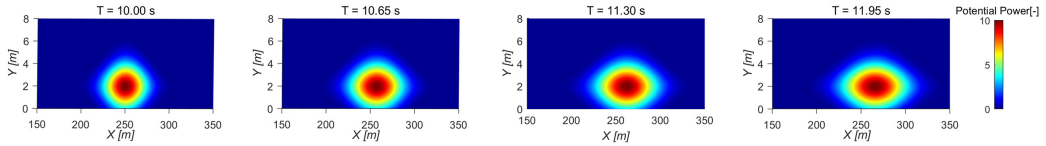
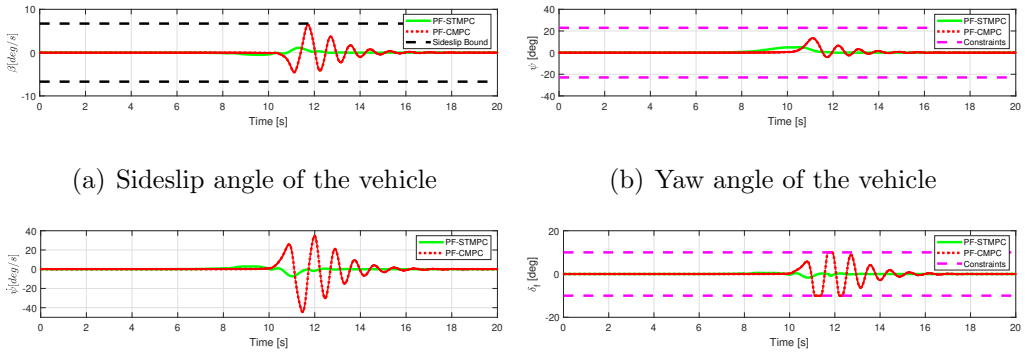


Figure 4.9: Variations in the front obstacle's potential field (3D to 2D projection X-Y plane) when the obstacle vehicle decelerates: From 10.00 s to 11.95 s, the PF expands rapidly around 255 m; the higher potential power means the higher collision risk

Comparative analysis of the ego vehicle's sideslip angle is described in Fig. 4.10(a). There exists a noticeable oscillation in PF-CMPC with a maximum of 6.5° and a minimum of approximately -4.5°, which is closer to the sideslip angle bound computed from Eq. (4.31) (depicted as a black dotted line). Conversely, the sideslip angle of PF-STMPC varies at a smaller range between -0.5° and 1.1°, which signifies the improved stability of the vehicle body. The conspicuous oscillation can be observed in PF-CMPC from Fig. 4.10(c) with -44.4 °/s at 11.47 s, which is the time when the obstacle decelerates abruptly, suddenly expanding the potential field. Consequently, there exists a visible yawing from 10.86 s to 16.40 s in the trajectory of PF-CMPC, as shown in Fig. 4.10(b). In contrast, the yaw rate of PF-STMPC changes gently between -7.3 °/s and 2.9 °/s, leading to a smoother variation in the vehicle's yaw angle at around 5.0° at the maximum. From Fig. 4.10(d), the front tire steering angle of PF-CMPC meets the constraints from 10 s to 15 s during collision avoidance. However, PF-STMPC vibrates in a smaller range and does not meet the constraint.



(a) Sideslip angle of the vehicle

(b) Yaw angle of the vehicle

(c) Yaw rate of the vehicle

(d) Front tire steering angle of the vehicle

Figure 4.10: Motion states of the vehicle: black dotted line means the empirical bound of the sideslip angle; magenta dotted line denoted the imposed hard constraints

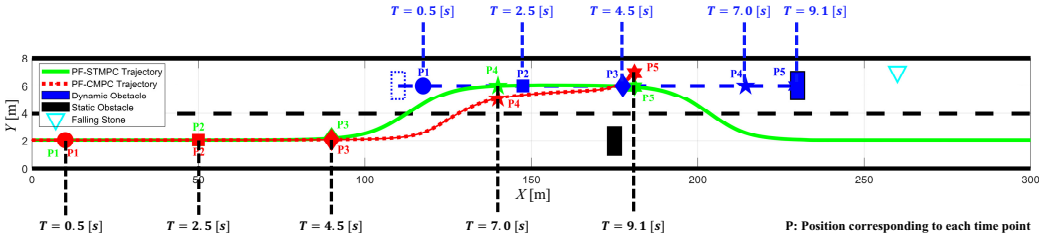


Figure 4.11: Comparative study of vehicle trajectories: static obstacle (black rectangle) parks at (175,2); dynamic obstacle (blue rectangle) decelerates (dotted blue line) due to the falling stone (cyan triangle); PF-STMPC trajectory (solid green line) safely goes through the closely spaced obstacles while PF-CMPC (dotted-solid red line) fails

Scenario II

The comparative results of the vehicle's trajectories, in Fig. 4.11, show that the PF-CMPC fails to plan a safe path when obstacle vehicles are closed due to emergency braking behavior. In Fig. 4.12, the potential field is rapidly enlarged due to the sudden deceleration of the dynamic obstacle leading to a partial overlap with the potential field of the static obstacle from 130 m to 200 m, causing an abnormal gradient change during path generation. Besides, the magenta dash line computed by the ST constraints of PF-STMPC indicates that the vehicle will be less affected by the sharp-increase potential field while driving within the designed ST for emergency navigation.

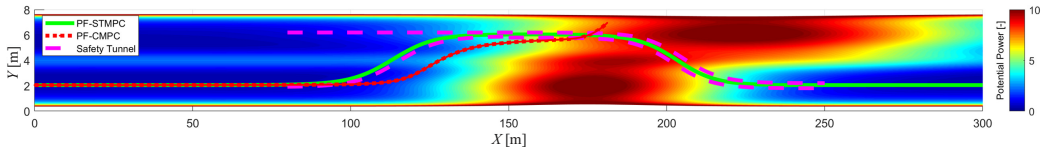
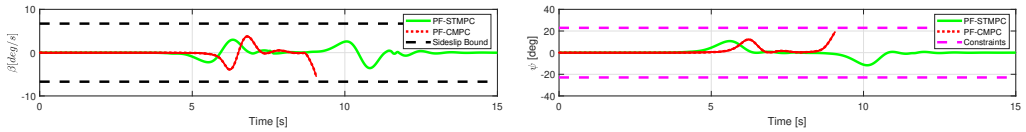
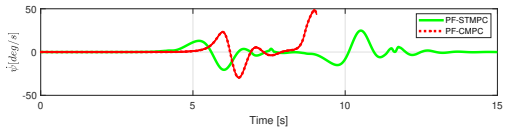


Figure 4.12: Potential power analysis and vehicle trajectories: the potential field was built on T=8 s; from 175 m to 220 m, there has a severe overlapping part in the two obstacles' potential fields that PF-CMPC moves toward the road boundary while PF-STMPC safely avoids the obstacles and stays within the road

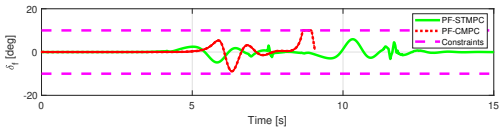


(a) Sideslip angle of the vehicle

(b) Yaw angle of the vehicle



(c) Yaw rate of the vehicle



(d) Front tire steering angle of the vehicle

Figure 4.13: Motion states of the vehicle: black dotted line means the empirical bound of the sideslip angle; magenta dotted line denoted the imposed hard constraints

The motion states of the vehicle are depicted in Figs. 4.13(a) to 4.13(c). The sideslip angle of PF-CMPC rises abruptly from 8.78 s to 9.27 s with a maximum value at 6.3° during the emergency avoidance and reaches the maximum sideslip bound, as shown in Fig. 4.13(a). In contrast, the sideslip angle of PF-STMPC varies in a smaller range between 2.9° and -3.5°. Besides, the yaw angle of PF-CMPC has local poorly-damped oscillations between 11.4° and 0.1° and the yaw rate reaches 42.8 °/s when the dynamic obstacle starts to decelerate. In contrast, the yaw angle of PF-STMPC changes between -10.0° and 10.0° and tends to be flat from 5 s to 8 s. The same phenomenon can be observed in Fig. 4.13(d), where the front tire steering angle of the PF-CMPC fluctuates from 8.5 s when the vehicle steers to avoid the front obstacle vehicles and reaches the predefined saturation between -10.0° and 10.0°. In contrast, the tire steering angle of the PF-STMPC is well computed

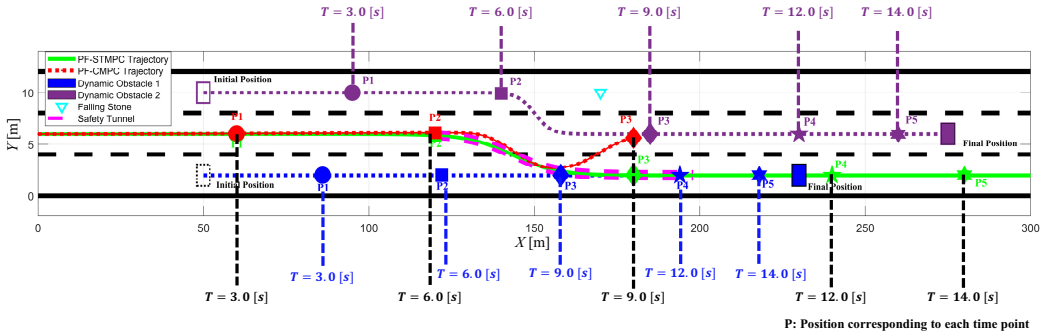


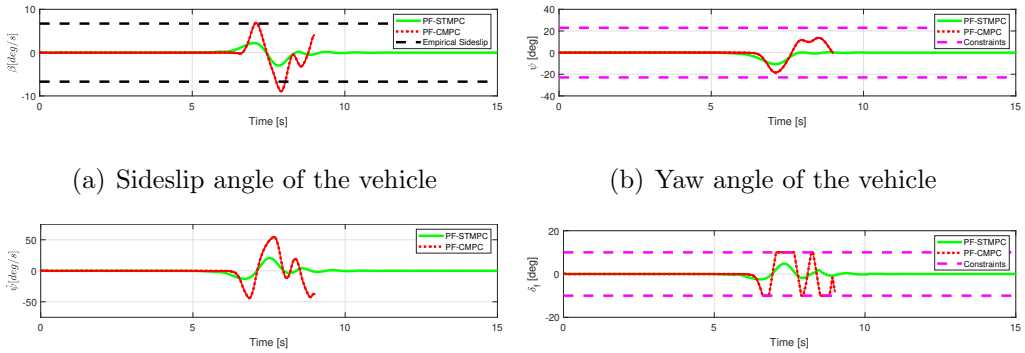
Figure 4.14: Comparative study of vehicle trajectories: dynamic obstacle 1 drives constantly at 12 [m/s] (dotted blue line); dynamic obstacle 2 moves at 15 [m/s] and suddenly changes its lane (dotted purple-brown line) due to the falling stone (cyan triangle); PF-CMPC trajectory (dotted-solid red line) collides with dynamic obstacle 2; PF-STMPC trajectory safely avoids the two obstacles under safety tunnel constraints (dotted magenta line)

and does not reach the limitation. Moreover, the STMPC's δ_f varies gently and the number of times to reach the constraint is significantly less than that of PF-CMPC in the later process of emergency avoidance from 7 s to 10 s.

Scenario III

The results of vehicle trajectories are depicted in Fig. 4.14. It is obvious to observe a severe yawing in the trajectory of PF-CMPC when dynamic obstacle 2 suddenly changes its lane due to an emergency. Fig. 4.15(a) shows that the sideslip angle of PF-CMPC exceeds the empirical sideslip value while that of PF-STMPC is changes within the empirical value. Besides, the yaw angle of PF-CMPC nearly reaches the lower bound around 18.4°, and its yaw rate exceeds 50.0 °/s, as shown in Figs. 4.15(b) and 4.15(c).

In contrast, the trajectory of PF-STMPC is smoother and more stable due to the ST constraints, and its yaw angle varies gently between -10.7° and 0.4°, leading to a small variation in the yaw rate of the vehicle ([-12.8, 20.5] °/s). Besides, the front tire steering angle of PF-CMPC arrives at the preset limitation and has a conspicuous vibration from 6.5 s to 8 s, as depicted in Fig. 4.15(d). In contrast, the front tire steering angle of PF-STMPC varies in a smaller range, within -2.5° and 4.8°.



(a) Sideslip angle of the vehicle

(b) Yaw angle of the vehicle

(c) Yaw rate of the vehicle

(d) Front tire steering angle of the vehicle

Figure 4.15: Motion states of the vehicle: black dotted line means the empirical bound of the sideslip angle; magenta dotted line denoted the imposed hard constraints

4.8 Summary

A specific STMPC integrated with PFs is presented for the emergency navigation of autonomous vehicles. PFs are combined with the longitudinal RSS model to account for the movements of surrounding obstacle vehicles, including acceleration and deceleration. Moreover, a novel sigmoid-like function is utilized to design the Safety Tunnel (ST) with fewer tuning parameters, especially when PFs fail to plan a safe and steady path due to unexpected events. Additionally, when the potential fields of vehicles partially overlap, the ST, embedded into the MPC constraints, aids in vehicle navigation.

To verify the performance of the STMPC approach, three comparative traffic emergency scenarios were conducted using MATLAB/Simulink and the CarSim Simulator. The simulation results demonstrate that the proposed STMPC can safely navigate the vehicle to avoid suddenly decelerating obstacles, whereas the Conventional MPC (CMPC) fails, particularly in instances where PFs are unable to perform navigation functions effectively.

Chapter 5

Conclusions

5.1 Summary and discussion

This thesis showcases a comprehensive autonomous vehicle navigation framework, dividing the approaches into non-cooperative and cooperative methods. Non-cooperative strategies, including "Time-To-Collision-Aware Lane-Change Strategy", "Occlusion-Aware Path Planning", and "Clothoid Curve-based Emergency Stopping", focus on individual vehicle actions to avoid collisions without relying on external communication. The cooperative strategies, including the "Risk Assessment Index", "Event-based Hybrid Planning", and "Interactive Speed Optimization for Lane Merging," leverage vehicle-to-vehicle communication to optimize path planning and enhance safety through shared information.

The framework incorporates "Emergency Triggering Estimation" to detect immediate hazards and "Safety Tunnel-based Emergency Navigation" that utilizes model predictive path-planning controllers for dynamic collision avoidance. These techniques involve complex algorithms that predict potential emergencies and calculate safe navigation paths in real-time, enhancing autonomous vehicles' ability to respond to unforeseen events.

This integrated approach aims to take a step forward in autonomous vehicle navigation, considering both the emergency response of individual vehicles and their collective behavior within traffic scenarios. The distinction between non-cooperative and cooperative strategies highlights the importance of inter-vehicle communication for complex traffic situations and emergency handling. However, the reliance on such communication also introduces challenges related to network reliability and latency. Emergency triggering estimation and safety tunnels indicate a move towards more anticipatory navigation systems, which are essential in dynamic environments

with unpredictable elements. The success of these systems depends on their ability to process vast amounts of data from various sensors and to make split-second decisions.

Future research may delve into the interoperability of these systems across different vehicle models and brands, the robustness of the communication networks required, and the development of universal standards for AV navigation. Furthermore, ensuring these advanced navigation systems are understandable and trustable for human passengers remains a crucial aspect of AV technology adoption.

5.2 Limitation

Although our proposal outperforms previous works in terms of emergency collision avoidance and cooperative planning, there is still a lot of room for improvement.

Tuning complexity The effectiveness of the PF methods in path planning is highly dependent on the specific environment, as parameters effective in open areas may not be suitable in cluttered or dynamic environments, requiring environment-specific tuning that increases complexity. Additionally, there is often a delicate trade-off between ensuring safety and maintaining efficient path planning; overly conservative parameters can result in excessively cautious behavior that reduces efficiency, whereas more aggressive parameters may compromise safety. Furthermore, effective tuning of potential fields typically demands significant expertise in system dynamics and a considerable amount of time dedicated to testing and making adjustments.

Complex road scenes In urban streets, unlike the structured environment of highways, driving conditions are often unstructured and chaotic, characterized by poorly marked lanes, irregular traffic flow, and unexpected obstacles such as construction zones or parked vehicles. Adding to this complexity are intersections and roundabouts, particularly those without traffic signals, where multi-directional traffic flow and the need for precise timing and path planning present additional challenges.

Model uncertainty The MPC depends on a predictive model to control a system, but uncertainties in this model, arising from inaccuracies in representing the system's dynamics or external influences, can impact the accuracy of predictions about future states. This misalignment can lead to sub-optimal control decisions. Furthermore, such model uncertainty poses challenges to

the robustness of MPC. Ideally, a robust control system should maintain consistent performance despite uncertainties and disturbances. However, if the model fails to accurately represent the system's behavior, the resulting control actions may not achieve the intended outcomes, particularly when the system or its environment undergoes unexpected changes.

Decision-making vulnerability In semi-autonomous vehicles, the transition between human-driven and autonomous modes presents significant decision-making challenges due to misaligned expectations between the system's capabilities and the human driver's understanding, potentially leading to accidents. Additionally, autonomous vehicles frequently face the challenge of making decisions with incomplete information, as they must navigate uncertainty and ambiguity in sensor data and human behavior prediction, further complicating the decision-making process.

Communication issues Reliable and low-latency communication is crucial for autonomous vehicles (autonomous vehicles), particularly for real-time data sharing and decision-making, as any delay or disruption can significantly impact the vehicle's ability to respond to dynamic road conditions. Furthermore, the need for standardization in communication protocols and technologies across various manufacturers and infrastructure systems is paramount to enable effective communication between autonomous vehicles from different companies and with traffic infrastructure. Additionally, with the increasing number of connected vehicles, the challenge of ensuring sufficient bandwidth to manage the extensive data exchange between autonomous vehicles and infrastructure systems becomes more pronounced.

Road experiments Continuous testing of autonomous vehicles in real environments is crucial for validating the performance of various subsystems such as perception, decision-making, and control, and it plays a key role in identifying areas for improvement to ensure the technology is reliable and ready for broader deployment. However, one of the biggest challenges faced during real road testing is dealing with unpredictable scenarios not previously encountered in simulations or controlled tests, like unique road incidents or complex interactions with pedestrians. Additionally, real road testing is instrumental in understanding the scalability of autonomous technology when deployed across diverse geographical and demographical areas.

Large-scale traffic Ensuring the scalability and reliability of autonomous systems to manage large-scale traffic poses a significant challenge, which

involves maintaining consistent performance during peak traffic times and under varied traffic conditions. Furthermore, adapting to large-scale traffic management with autonomous vehicles necessitates substantial adaptations and upgrades to existing road infrastructure, including the installation of smart traffic signals, sensors, and communication systems that can effectively interact with autonomous vehicles to optimize traffic flow and enhance safety.

5.3 Ethical issues

Ethical issues in the development and deployment of autonomous vehicles are complex and multifaceted, reflecting the profound impact these technologies have on society. Some of the key ethical considerations include:

Decision-making in critical situations One of the most debated ethical issues is how autonomous vehicles should make decisions in life-threatening scenarios, often referred to as "trolley problem" situations. For example, if an accident is unavoidable, should the autonomous vehicle prioritize the safety of its passengers, pedestrians, or other road users? Programming these moral decisions into machines raises profound ethical questions.

Privacy concerns Autonomous vehicles collect and process large amounts of data, including the location and travel patterns of passengers, which can lead to privacy concerns. How this data is used, stored, and shared raises important ethical considerations about privacy rights and data security.

Liability and accountability Determining liability in the event of a crash involving an AV is a significant ethical and legal challenge. The question of who is responsible—the manufacturer, the software developer, the vehicle owner, or the passenger—needs clear ethical guidelines and legal frameworks.

Equity and accessibility There are concerns about whether autonomous vehicles will be accessible and affordable to all segments of society. There is a risk that these technologies could exacerbate social inequalities if they are only available to certain economic or demographic groups.

Security risks The possibility of hacking and other cybersecurity threats pose ethical concerns regarding the safety of passengers and other road users.

Ensuring the security of autonomous vehicles is crucial to protect individuals from malicious activities.

Public trust and transparency Gaining public trust in autonomous vehicles requires transparency about how these vehicles operate, their safety features, and their decision-making processes. Ethically, the public has a right to understand the technologies that are increasingly shaping their environment and daily lives.

Addressing these ethical issues requires a collaborative approach involving policymakers, manufacturers, technologists, ethicists, and the public to develop frameworks and guidelines that ensure the responsible development and deployment of autonomous vehicles.

5.4 Future perspective

The future development of potential field-based path planning in autonomous vehicles is heavily intertwined with the advancement of ethical and fair decision-making. As autonomous vehicles become more integral to our transportation systems, ensuring their decision-making aligns with ethical guidelines and traffic laws is paramount. This will likely see potential field methods being combined with rule-based systems, designed to adhere to these ethical standards, while also incorporating learning-based approaches for adaptability in morally ambiguous situations. Advancements in machine learning and AI, especially in reinforcement learning, will be pivotal in enhancing the ability of autonomous vehicles to navigate through diverse scenarios. These advancements will enable autonomous vehicles to learn from a wide array of experiences, improving their navigation strategies in complex environments.

Handling more diverse and large-scale traffic scenarios is another key area of focus. Future potential field methods need to scale effectively to manage high-density urban environments and interact seamlessly with various traffic participants. The ability of these systems to adapt to randomized and dynamic obstacles will be crucial, requiring real-time adjustments to potential fields based on sensor inputs and predictive models. Furthermore, the integration of potential field methods with other systems, like V2X communication and advanced sensor technologies, will play a critical role in managing complex driving scenarios more effectively.

Lastly, the alignment of potential field-based path planning with emerging ethical frameworks and public policies focused on autonomous vehicles is crucial. Addressing public concerns around liability, safety standards, and acceptance will require these systems to be not only effective but also trans-

parent and explainable. Customization of potential field methods for specific geographical regions will also be necessary to account for local traffic conditions and regulations. As these systems evolve, striving for human-like decision-making will improve interactions between autonomous vehicles and human drivers, leading to a more natural and safer traffic intelligence.

Bibliography

[AHZY+18] Umar Zakir Abdul Hamid, Hairi Zamzuri, Tsuyoshi Yamada, Mohd Azizi Abdul Rahman, Yuichi Saito, and Pongsathorn Raksincharoensak. Modular design of artificial potential field and nonlinear model predictive control for a vehicle collision avoidance system with move blocking strategy. *Proceedings of the Institution of Mechanical Engineers, Part D: Journal of Automobile Engineering*, 232(10):1353–1373, September 2018.

[AKR+04] S Acierno, R Kaufman, F P Rivara, D C Grossman, and C Mock. Vehicle mismatch: injury patterns and severity. *Accident; analysis and prevention*, 36(5):761–772, September 2004.

[APH21] H Ataelmanan, O C Puan, and S A Hassan. Examination of lane changing duration time on expressway. *IOP Conference Series: Materials Science and Engineering*, 1144(1):012078, May 2021.

[Ara22] Szilard Aradi. Survey of deep reinforcement learning for motion planning of autonomous vehicles. *IEEE Transactions on Intelligent Transportation Systems*, 23(2):740–759, February 2022.

[CHM21] Sally C Curtin, Holly Hedegaard, and Pedro Martinez. Death rates for motor-vehicle-traffic injuries, suicide, and homicide among adolescents and young adults aged 15-24 years-united states, 1999-2019. *Morb. Mortal. Wkly. Rep.*, 70(5):184–184, February 2021.

[CLZZ22] Duanfeng Chu, Haoran Li, Chenyang Zhao, and Tuqiang Zhou. Trajectory tracking of autonomous vehicle based on model predictive control with PID feedback. *IEEE Trans. Intell. Transp. Syst.*, 24(2):1–12, 2022.

[CYHZ20] Liu Cao, Hao Yin, Jie Hu, and Lyutianyang Zhang. Performance analysis and improvement on DSRC application for V2V communication. In *2020 IEEE 92nd Vehicular Technology Conference (VTC2020-Fall)*, pages 1–6. ieeexplore.ieee.org, November 2020. doi:10.1109/VTC2020-Fall49728.2020.9348743.

[Dav15] Alex Davies. Turns out the hardware in self-driving cars is pretty cheap. *Medium*, April 2015. Accessed: Sep. 2022. [Online.] Available: https://www.wired.com/2015/04/cost-of-sensors-autonomous-cars/.

[DBK+14] František Duchoň, Andrej Babinec, Martin Kajan, Peter Beňo, Martin Florek, Tomáš Fico, and Ladislav Jurišica. Path planning with modified a star algorithm for a mobile robot. *Procedia Engineering*, 96:59–69, January 2014.

[DCN16] Vinayak V Dixit, Sai Chand, and Divya J Nair. Autonomous vehicles: Disengagements, accidents and reaction times. *PloS One*, 11(12):e0168054, December 2016. doi:10.1371/journal.pone.0168054.

[Dij72] Edsger W Dijkstra. The humble programmer. *Communications of the ACM*, 15(10):859–866, October 1972.

[DMD+20] Shilp Dixit, Umberto Montanaro, Mehrdad Dianati, David Oxtoby, Tom Mizutani, Alexandros Mouzakitis, and Saber Fallah. Trajectory planning for autonomous High-Speed overtaking in structured environments using robust MPC. *IEEE Transactions on Intelligent Transportation Systems*, 21(6):2310–2323, June 2020.

[DTMD08] Dmitri Dolgov, Sebastian Thrun, Michael Montemerlo, and James Diebel. Practical search techniques in path planning for autonomous driving. https://cdn.aaai.org/Workshops/2008/WS-08-10/WS08-10-006.pdf, 2008. Accessed: 2023-11-10.

[DZZ+23] Guodong Du, Yuan Zou, Xudong Zhang, Zirui Li, and Qi Liu. Hierarchical motion planning and tracking for autonomous vehicles using global heuristic based potential field and reinforcement learning based predictive control. *IEEE Trans. Intell. Transp. Syst.*, April 2023. early access. doi: 10.1109/TITS.2023.3266195.

[ECP+16] Cristofer Englund, Lei Chen, Jeroen Ploeg, Elham Semsar-Kazerooni, Alexey Voronov, Hoai Hoang Bengtsson, and Jonas Didoff. The grand cooperative driving challenge 2016: boosting the introduction of cooperative automated vehicles. *IEEE Wireless Communications*, 23(4):146–152, August 2016.

[Edm22] Tewari Edmonson. Connected-autonomous vehicle (cav) program. *Miami-Dade Transportation Planning Organization*, December 2022. Accessed: Sep. 2022. [Online.] Available: https://www.miamidadetpo.org/connected-autonomous-vehicle-program.asp.

[EHSo11] Eckert, Hartmann, Sevenich, and others. Emergency steer & brake assist: a systematic approach for system integration of two complementary driver assistance systems. In *22nd International Technical Conference on the Enhanced Safety of Vehicles (ESV)*, 2011.

[Eri04] Christer Ericson. *Real-Time Collision Detection*. CRC Press, December 2004.

[FZM15] Sheikh Muhammad Hafiz Fahami, Hairi Zamzuri, and Saiful Amri Mazlan. Development of estimation force feedback torque control algorithm for driver steering feel in vehicle steer by wire system: Hardware in the loop. *International Journal of Vehicular Technology*, 2015, 2015.

[GHCG13] Romain Gallen, Nicolas Hautière, Aurélien Cord, and Sébastien Glaser. Supporting drivers in keeping safe speed in adverse weather conditions by mitigating the risk level. *IEEE Transactions on Intelligent Transportation Systems*, 14(4):1558–1571, December 2013.

[HCWH19] Zichao Huang, Duanfeng Chu, Chaozhong Wu, and Yi He. Path planning and cooperative control for automated vehicle platoon using hybrid automata. *IEEE Transactions on Intelligent Transportation Systems*, 20(3):959–974, March 2019.

[HDZ+20] Yanjun Huang, Haitao Ding, Yubiao Zhang, Hong Wang, Dongpu Cao, Nan Xu, and Chuan Hu. A motion planning and tracking framework for autonomous vehicles based on artificial potential field elaborated resistance network approach. *IEEE Transactions on Industrial Electronics*, 67(2):1376–1386, February 2020.

[HHH+21] Peng Hang, Chao Huang, Zhongxu Hu, Yang Xing, and Chen Lv. Decision making of connected automated vehicles at an unsignalized roundabout considering personalized driving behaviours. *IEEE Transactions on Vehicular Technology*, 70(5):4051–4064, May 2021.

[HHHL22] Peng Hang, Chao Huang, Zhongxu Hu, and Chen Lv. Driving conflict resolution of autonomous vehicles at unsignalized intersections: A differential game approach. *IEEE/ASME Transactions on Mechatronics*, 27(6):5136–5146, December 2022.

[HLH+20] Peng Hang, Chen Lv, Chao Huang, Jiacheng Cai, Zhongxu Hu, and Yang Xing. An integrated framework of decision making and motion planning for autonomous vehicles considering social behaviors. *IEEE Transactions on Vehicular Technology*, 69(12):14458–14469, December 2020.

[HNR68] Peter E Hart, Nils J Nilsson, and Bertram Raphael. A formal basis for the heuristic determination of minimum cost paths. *IEEE Transactions on Systems Science and Cybernetics*, 4(2):100–107, July 1968.

[HTO+21] Mai Hirata, Manabu Tsukada, Keisuke Okumura, Yasumasa Tamura, Hideya Ochiai, and Xavier Défago. Roadside-Assisted cooperative planning using future path sharing for autonomous driving. In *2021 IEEE 94th Vehicular Technology Conference (VTC2021-Fall)*, pages 1–7, September 2021.

[HWK+20] Yanjun Huang, Hong Wang, Amir Khajepour, Haitao Ding, Kang Yuan, and Yechen Qin. A novel local motion planning framework for autonomous vehicles based on resistance network and model predictive control. *IEEE Transactions on Vehicular Technology*, 69(1):55–66, January 2020.

[HZZ+17] Umar Zakir Abdul Hamid, Fakhrul Razi Ahmad Zakuan, Khairul Akmal Zulkepli, Muhammad Zulfaqar Azmi, Hairi Zamzuri, Mohd Azizi Abdul Rahman, and Muhammad Aizzat Zakaria. Autonomous emergency braking system with potential field risk assessment for frontal collision mitigation. In *2017 IEEE Conference on Systems, Process and Control (ICSPC)*, pages 71–76, December 2017.

[Int18] SAE International. Taxonomy and definitions for terms related to driving automation systems for on-road motor vehicles. *SAE International*, 4970(724):1–5, 2018.

[JKLC15] Soo Jung Jeon, Chang Mook Kang, Seung-Hi Lee, and Chung Choo Chung. GPS waypoint fitting and tracking using model predictive control. In *2015 IEEE Intelligent Vehicles Symposium (IV)*, pages 298–303, June 2015.

[JKMH17] Jie Ji, Amir Khajepour, Wael William Melek, and Yanjun Huang. Path planning and tracking for vehicle collision avoidance based on model predictive control with multiconstraints.

IEEE Transactions on Vehicular Technology, 66(2):952–964, February 2017.

[JNZ+23] Yuxiong Ji, Lantao Ni, Cong Zhao, Cailin Lei, Yuchuan Du, and Wenshuo Wang. TriPField: A 3D potential field model and its applications to local path planning of autonomous vehicles. *IEEE Trans. Intell. Transp. Syst.*, 24(3):3541–3554, March 2023.

[KB91] Y Koren and J Borenstein. Potential field methods and their inherent limitations for mobile robot navigation. In *Proceedings. 1991 IEEE International Conference on Robotics and Automation*, pages 1398–1404 vol.2, April 1991.

[Kha85] O Khatib. Real-time obstacle avoidance for manipulators and mobile robots. In *Proceedings. 1985 IEEE International Conference on Robotics and Automation*, volume 2, pages 500–505, March 1985.

[KKL98] L E Kavraki, M N Kolountzakis, and J-C Latombe. Analysis of probabilistic roadmaps for path planning. *IEEE transactions on robotics and automation: a publication of the IEEE Robotics and Automation Society*, 14(1):166–171, February 1998.

[KLC17] Chang Mook Kang, Seung-Hi Lee, and Chung Choo Chung. On-road path generation and control for waypoints tracking. *IEEE Intell. Transp. Syst. Mag.*, 9(3):36–45, July 2017.

[KS80] J Kenneth Salisbury. Active stiffness control of a manipulator in cartesian coordinates. In *1980 19th IEEE Conference on Decision and Control including the Symposium on Adaptive Processes*, pages 95–100. IEEE, December 1980.

[KSLO96] L E Kavraki, P Svestka, J-C Latombe, and M H Overmars. Probabilistic roadmaps for path planning in high-dimensional configuration spaces. *IEEE transactions on robotics and automation: a publication of the IEEE Robotics and Automation Society*, 12(4):566–580, August 1996.

[KWP+11] Sertac Karaman, Matthew R Walter, Alejandro Perez, Emilio Frazzoli, and Seth Teller. Anytime motion planning using the RRT. In *2011 IEEE international conference on robotics and automation*, pages 1478–1483. ieeexplore.ieee.org, 2011.

[LBAT20] Sara Luciani, Angelo Bonfitto, Nicola Amati, and Andrea Tonoli. Model predictive control for comfort optimization in assisted and driverless vehicles. *Advances in Mechanical Engineering*, 12(11):1687814020974532, November 2020.

[LCC20a] Pengfei Lin, Woo Young Choi, and Chung Choo Chung. Intelligent vehicle for collision avoidance using artificial potential field with speed variation. *Korean Society of Automotive Engineers (KSAE)*, pages 348–352, 2020.

[LCC20b] Pengfei Lin, Woo Young Choi, and Chung Choo Chung. Local path planning using artificial potential field for waypoint tracking with collision avoidance. In *2020 IEEE 23rd International Conference on Intelligent Transportation Systems (ITSC)*, pages 1–7, September 2020.

[LCLC20] P Lin, W Y Choi, S-H Lee, and C C Chung. Model predictive path planning based on artificial potential field and its application to autonomous lane change. In *2020 20th International Conference on Control, Automation and Systems (ICCAS)*, pages 731–736, October 2020.

[LCYC20] Pengfei Lin, Woo Young Choi, Jin Ho Yang, and Chung Choo Chung. Waypoint tracking for collision avoidance using artificial potential field. In *2020 39th Chinese Control Conference (CCC)*, pages 5455–5460. IEEE, July 2020.

[Lee76] D N Lee. A theory of visual control of braking based on information about time-to-collision. *Perception*, 5(4):437–459, 1976.

[LHY+20] Bing Lu, Hongwen He, Huilong Yu, Hong Wang, Guofa Li, Man Shi, and Dongpu Cao. Hybrid path planning combining potential field with sigmoid curve for autonomous driving. *Sensors*, 20(24), December 2020.

[LK19] Kibeom Lee and Dongsuk Kum. Collision Avoidance/Mitigation system: Motion planning of autonomous vehicle via predictive occupancy map. *IEEE Access*, 7:52846–52857, 2019.

[LKDO01] Steven M LaValle, James J Kuffner, B R Donald, and Others. Rapidly-exploring random trees: Progress and prospects. *Algorithmic and computational robotics: new directions*, 5:293–308, 2001.

[LLY+20] Bing Lu, Guofa Li, Huilong Yu, Hong Wang, Jinquan Guo, Dongpu Cao, and Hongwen He. Adaptive potential Field-Based path planning for complex autonomous driving scenarios. *IEEE Access*, 8:225294–225305, 2020.

[LLY+22] Hongcai Li, Wenjie Liu, Chao Yang, Weida Wang, Tianqi Qie, and Changle Xiang. An Optimization-Based path planning approach for autonomous vehicles using the DynEFWA-Artificial potential field. *IEEE Transactions on Intelligent Vehicles*, 7(2):263–272, June 2022.

[LWC+21] Haoran Li, Chaozhong Wu, Duanfeng Chu, Liping Lu, and Ken Cheng. Combined trajectory planning and tracking for autonomous vehicle considering driving styles. *IEEE Access*, 9:9453–9463, 2021.

[LYQC22] Pengfei Lin, Jin Ho Yang, Ying Shuai Quan, and Chung Choo Chung. Potential field-based path planning for emergency collision avoidance with a clothoid curve in waypoint tracking. *Asian journal of control*, 24(3):1074–1087, May 2022.

[Lyu11] D Lyubenov. Research of the stopping distance for different road conditions. *Transp. Probl.*, T. 6, z. 4(4):119–126, 2011.

[Mil22] Justin Milner. A visual guide to the software architecture of autonomous vehicles. *Medium*, September 2022. Accessed: Sep. 2022. [Online.] Available: https://medium.com/@justinmilner/a-visual-guide-to-the-software-architecture-of-autonomous-vehicles-390b1744cbd6.

[Mob22] Mobileye. Forward collision warning. *Technology Reports*, January 2022.

[MTE21] Masaya Mizutani, Manabu Tsukada, and Hiroshi Esaki. AutoMCM: Maneuver coordination service with abstracted functions for autonomous driving. In *2021 IEEE International Intelligent Transportation Systems Conference (ITSC)*, pages 1069–1076, September 2021.

[MUDL11] Matthew McNaughton, Chris Urmson, John M Dolan, and Jin-Woo Lee. Motion planning for autonomous driving with a conformal spatiotemporal lattice. In *2011 IEEE International Conference on Robotics and Automation*, pages 4889–4895. IEEE, May 2011.

[NK01] Bryan Nagy and Alonzo Kelly. Trajectory generation for car-like robots using cubic curvature polynomials. *Field and Service Robots*, 11:479–490, 2001.

[NKLS19] Maximilian Naumann, Hendrik Konigshof, Martin Lauer, and Christoph Stiller. Safe but not overcautious motion planning under occlusions and limited sensor range. In *2019 IEEE Intelligent Vehicles Symposium (IV)*, pages 140–145, June 2019.

[NS22] Maximilian Naumann and Christoph Stiller. AIB-MDP: Continuous probabilistic motion planning for automated vehicles by leveraging action independent belief spaces. In *2022 IEEE/RSJ International Conference on Intelligent Robots and Systems (IROS)*, pages 6373–6380, October 2022.

[oC21] Soka Gakkai International Association of Canada. Saskatchewan driver's handbook. *Saskatchewan Driver's Handbook*, June 2021. [Online]. Available: https://sgi.sk.ca/handbook/-/knowledge_base/drivers/emergency-driving.

[oMV21] Department of Motor Vehicles. Autonomous vehicle collision reports. *DMV.ca.gov*, 2021. Accessed: Aug. 2022. [Online.] Available: https://www.dmv.ca.gov/portal/vehicle-industry-services/autonomous-vehicles/autonomous-vehicle-collision-reports/.

[Org22] World Health Organization. Road traffic injuries. *News Rep.*, January 2022. [Online]. Available: https://www.who.int/news-room/fact-sheets/detail/road-traffic-injuries.

[PCS+20] Yunpeng Pan, Ching-An Cheng, Kamil Saigol, Keuntaek Lee, Xinyan Yan, Evangelos A Theodorou, and Byron Boots. Imitation learning for agile autonomous driving. *The International journal of robotics research*, 39(2-3):286–302, March 2020.

[PJL01] Min Gyu Park, Jae Hyun Jeon, and Min Cheol Lee. Obstacle avoidance for mobile robots using artificial potential field approach with simulated annealing. In *ISIE 2001. 2001 IEEE International Symposium on Industrial Electronics Proceedings*, volume 3, pages 1530–1535 vol.3. IEEE, 2001.

[PRMS95] Dianne Parker, James T Reason, Antony S R Manstead, and Stephen G Stradling. Driving errors, driving violations and accident involvement. *Ergonomics*, 38(5):1036–1048, May 1995.

[PTP+09] Claudiu Pozna, Fritz Troester, Radu-Emil Precup, József K Tar, and Stefan Preitl. On the design of an obstacle avoiding trajectory: Method and simulation. *Mathematics and computers in simulation*, 79(7):2211–2226, March 2009.

[PVBN20] Renaud Poncelet, Anne Verroust-Blondet, and Fawzi Nashashibi. Safe geometric speed planning approach for autonomous driving through occluded intersections. In *2020 16th International Conference on Control, Automation, Robotics and Vision (ICARCV)*, pages 393–399, December 2020.

[Raj11] Rajesh Rajamani. *Vehicle Dynamics and Control*. Springer Science & Business Media, December 2011.

[RD94] Carl Ragland and Gayle Dalrymple. Overlap car-to-car tests compared to car-to-half barrier and car-to-full barrier tests. *AUTO & TRAFFIC SAFETY*, 1(2), 1994.

[Ren23] Jianfeng Ren. *Autonomous driving algorithms and Its IC Design*. Springer Verlag, Singapore, August 2023. pp. 1–23.

[RHo16] P Raksincharoensak, T Hasegawa, and others. Motion planning and control of autonomous driving intelligence system based on risk potential optimization framework. *International Journal of*, 2016.

[RKCL17] Yadollah Rasekhipour, Amir Khajepour, Shih-Ken Chen, and Bakhtiar Litkouhi. A potential field-based model predictive path-planning controller for autonomous road vehicles. *IEEE Trans. Intell. Transp. Syst.*, 18(5):1255–1267, May 2017.

[Rud16] Sebastian Ruder. An overview of gradient descent optimization algorithms. September 2016.

[SE23] Xu Shang and Azim Eskandarian. Emergency collision avoidance and mitigation using model predictive control and artificial potential function. *IEEE Transactions on Intelligent Vehicles*, 8(5):3458–3472, May 2023.

[SF97] A Scheuer and Th Fraichard. Continuous-curvature path planning for car-like vehicles. In *Proc. IEEE Int. Conf. Intell. Robots Syst.*, volume 2, pages 997–1003, September 1997.

[SMT+23] P Stano, U Montanaro, D Tavernini, M Tufo, G Fiengo, L Novella, and A Sorniotti. Model predictive path tracking control for automated road vehicles: A review. *Annual reviews in control*, 55:194–236, January 2023.

[Sna18] E Snapper. Model-based path planning and control for autonomous vehicles using artificial potential fields. *M.S. Thesis, Dept. Mech. Eng., TU Delft, Delft, Netherlands*, 2018. [Online]. Available: https://repository.tudelft.nl/islandora/object/uuid:453a26ea-8556-4927-8d9f-2058f7dcda15.

[Soc22] IEEE Vehicular Technology Society. Ieee standard for assumptions in safety-related models for automated driving systems. *IEEE Std 2846-2022*, pages 1–59, April 2022. doi:10.1109/IEEESTD.2022.9761121.

[SR12] Igor R Shafarevich and Alexey O Remizov. *Linear Algebra and Geometry*. Springer Science & Business Media, August 2012.

[SSSS17] Shai Shalev-Shwartz, Shaked Shammah, and Amnon Shashua. On a formal model of safe and scalable self-driving cars. August 2017.

[SSSS18] A Shashua, S Shalev-Shwartz, and S Shammah. Implementing the rss model on nhtsa pre-crash scenarios. *Tech. Rep.*, 2018. [Online]. Available: https://www.mobileye.com/technology/responsibility-sensitive-safety/.

[Sta22] Statista. Number of road traffic accidents in japan from 2010 to 2022. *Japan Road Traffic Accidents*, January 2022. [Online]. Available: https://www.statista.com/statistics/661958/japan-road-traffic-accidents/.

[STJP06] C Sierra, E Tseng, A Jain, and H Peng. Cornering stiffness estimation based on vehicle lateral dynamics. *Vehicle System Dynamics*, 44(sup1):24–38, January 2006.

[SY19] Keitaro Sato and Wonseok Yang. Design development of the support tool to prevent secondary accidents on highway. In Constantine Stephanidis, editor, *HCI International 2019 - Posters*, pages 381–388, Cham, 2019. Springer International Publishing.

[TLL22] Haitian Tan, Guangquan Lu, and Miaomiao Liu. Risk field model of driving and its application in modeling Car-Following behavior. *IEEE Transactions on Intelligent Transportation Systems*, 23(8):11605–11620, August 2022.

[TLZ+18] Sarah M Thornton, Francis E Lewis, Vivian Zhang, Mykel J Kochenderfer, and J Christian Gerdes. Value sensitive design for autonomous vehicle motion planning. In *2018 IEEE Intelligent Vehicles Symposium (IV)*, pages 1157–1162, June 2018.

[TS18] Ömer Şahin Taş and Christoph Stiller. Limited visibility and uncertainty aware motion planning for automated driving. In *2018 IEEE Intelligent Vehicles Symposium (IV)*, pages 1171–1178, June 2018.

[US03] C Urmson and R Simmons. Approaches for heuristically biasing RRT growth. In *Proceedings 2003 IEEE/RSJ International Conference on Intelligent Robots and Systems (IROS 2003)*, volume 2, pages 1178–1183 vol.2. IEEE, 2003.

[VK90] R Volpe and P Khosla. Manipulator control with superquadric artificial potential functions: theory and experiments. *IEEE transactions on systems, man, and cybernetics*, 20(6):1423–1436, November 1990.

[VTML00] P Vadakkepat, Kay Chen Tan, and Wang Ming-Liang. Evolutionary artificial potential fields and their application in real time robot path planning. In *Proceedings of the 2000 Congress on Evolutionary Computation*, volume 1, pages 256–263 vol.1. IEEE, 2000.

[Wan94] Jing-Shiarn Wang. *Lane Change/merge Crashes: Problem Size Assessment and Statistical Description.* U.S. Department of Transportation, National Highway Traffic Safety Administration, 1994.

[WB08] Michael T Wolf and Joel W Burdick. Artificial potential functions for highway driving with collision avoidance. In *2008 IEEE International Conference on Robotics and Automation*, pages 3731–3736, May 2008.

[WFZS23] Denggui Wang, Weiping Fu, Jincao Zhou, and Qingyuan Song. Occlusion-Aware motion planning for autonomous driving. *IEEE Access*, 11:42809–42823, 2023.

[WG22] Qiannan Wang and Matthias Gerdts. Risk-based path planning for autonomous vehicles. March 2022.

[WGL+19] Pengwei Wang, Song Gao, Liang Li, Binbin Sun, and Shuo Cheng. Obstacle avoidance path planning design for autonomous driving vehicles based on an improved artificial potential field algorithm. *Energies*, 12(12):2342, June 2019.

[WGL22] Ping Wu, Feng Gao, and Keqiang Li. Humanlike decision and motion planning for expressway lane changing based on artificial potential field. *IEEE Access*, 10(3):4359–4373, January 2022.

[WGW21] Yue Wang, Yafeng Guo, and Jun Wang. A hierarchical planning framework of the intersection with blind zone and uncertainty. In *2021 IEEE International Intelligent Transportation Systems Conference (ITSC)*, pages 687–692, September 2021.

[WHK+18] Hong Wang, Yanjun Huang, Amir Khajepour, Teng Liu, Yechen Qin, and Yubiao Zhang. Local path planning for autonomous vehicles: Crash mitigation. In *2018 IEEE Intelligent Vehicles Symposium (IV)*, pages 1602–1606. IEEE, June 2018.

[WHK+19] Hong Wang, Yanjun Huang, Amir Khajepour, Yubiao Zhang, Yadollah Rasekhipour, and Dongpu Cao. Crash mitigation in motion planning for autonomous vehicles. *IEEE Transactions on Intelligent Transportation Systems*, 20(9):3313–3323, September 2019.

[WHK+20] Hong Wang, Yanjun Huang, Amir Khajepour, Dongpu Cao, and Chen Lv. Ethical Decision-Making platform in autonomous vehicles with lexicographic optimization based model predictive controller. *IEEE Transactions on Vehicular Technology*, 69(8):8164–8175, August 2020.

[WN15] Cong Wang and Henk Nijmeijer. String stable heterogeneous vehicle platoon using cooperative adaptive cruise control. In *2015 IEEE 18th International Conference on Intelligent Transportation Systems*, pages 1977–1982, September 2015.

[WWL15] Jianqiang Wang, Jian Wu, and Yang Li. The driving safety field based on Driver–Vehicle–Road interactions. *IEEE Transactions on Intelligent Transportation Systems*, 16(4):2203–2214, August 2015.

[WWLL14] Jianqiang Wang, Jian Wu, Yang Li, and Keqiang Li. The concept and modeling of driving safety field based on driver-vehicle-road interactions. In *17th International IEEE Conference on Intelligent Transportation Systems (ITSC)*, pages 974–981, October 2014.

[WYY11] Huijuan Wang, Yuan Yu, and Quanbo Yuan. Application of dijkstra algorithm in robot path-planning. In *2011 Second International Conference on Mechanic Automation and Control Engineering*, pages 1067–1069. IEEE, July 2011.

[WYZ+22] Jinxiang Wang, Yongjun Yan, Kuoran Zhang, Yimin Chen, Mingcong Cao, and Guodong Yin. Path planning on large curvature roads using Driver-Vehicle-Road system based on the kinematic vehicle model. *IEEE Transactions on Vehicular Technology*, 71(1):311–325, January 2022.

[WZKT10] Moritz Werling, Julius Ziegler, Sören Kammel, and Sebastian Thrun. Optimal trajectory generation for dynamic street scenarios in a frenet frame. In *Proc. IEEE Int. Conf. Robot. Autom.*, pages 987–993, July 2010.

[XHB+22] Songtao Xie, Junyan Hu, Parijat Bhowmick, Zhengtao Ding, and Farshad Arvin. Distributed motion planning for safe autonomous vehicle overtaking via artificial potential field. *IEEE Trans. Intell. Transp. Syst.*, 23(11):21531–21547, November 2022.

[YHZ22] Zhengcai Yang, Yunzhong Hu, and Youbing Zhang. Path-Planning strategy for lane changing based on Adaptive-Grid Risk-Fields of autonomous vehicles. *World Electric Vehicle Journal*, 13(10):175, September 2022.

[YLQ+20] Ziwei Yi, Linheng Li, Xu Qu, Yang Hong, Peipei Mao, and Bin Ran. Using artificial potential field theory for a cooperative control model in a connected and automated vehicles environment. *Transportation research record*, 2674(9):1005–1018, September 2020.

[YWSH20] Yanna Yin, Huiying Wen, Lu Sun, and Wei Hou. The influence of road geometry on vehicle rollover and skidding. *Int. J. Environ. Res. Public Health*, 17(5):1648–1664, March 2020.

[YWZ+22] Yongjun Yan, Jinxiang Wang, Kuoran Zhang, Yulong Liu, Yahui Liu, and Guodong Yin. Driver's individual risk Perception-Based trajectory planning: A Human-Like method. *IEEE Transactions on Intelligent Transportation Systems*, 23(11):20413–20428, November 2022.

[ZPM07] Xiaoyu Zheng and Peter Palffy-Muhoray. Distance of closest approach of two arbitrary hard ellipses in two dimensions. *Physical review. E, Statistical, nonlinear, and soft matter physics*, 75(6 Pt 1):061709, June 2007.

[ZS09] Julius Ziegler and Christoph Stiller. Spatiotemporal state lattices for fast trajectory planning in dynamic on-road driving scenarios. In *2009 IEEE/RSJ International Conference on Intelligent Robots and Systems*, pages 1879–1884. IEEE, October 2009.

Publications

Publications as First Author

International Journal

[1] **Pengfei Lin** and Manabu Tsukada, "Model Predictive Path-Planning Controller with Potential Function for Emergency Collision Avoidance on Highway Driving," *IEEE Robotics and Automation Letters*, vol. 7, no. 2, pp. 4662–4669, Apr. 2022.

[2] **Pengfei Lin**, Ying Shuai Quan, Jin Ho Yang, Chung Choo Chung, and Manabu Tsukada, "Safety Tunnel-Based Model Predictive Path-Planning Controller with Potential Functions for Emergency Navigation," *IEEE Transactions on Intelligent Transportation Systems*, vol. 24, no. 4, pp. 3974–3985, Apr. 2023.

[3] **Pengfei Lin**, Ehsan Javanmardi, and Manabu Tsukada, "Clothoid Curve-based Emergency-Stopping Path Planning with Adaptive Potential Field for Autonomous Vehicles," Major Revision in *IEEE Transactions on Vehicular Technology*.

International Conferences

[4] **Pengfei Lin** and Manabu Tsukada, "Adaptive Potential Field with Collision Avoidance for Connected Autonomous Vehicles," in *Proceedings of the 2022 13th Asian Control Conference (ASCC)*, pp. 2251–2256, May 2022.

[5] **Pengfei Lin** and Manabu Tsukada, "Cooperative Path Planning Using Responsibility-Sensitive Safety (RSS)-based Potential Field with Sig-

moid Curve," in *2022 IEEE 95th Vehicular Technology Conference: (VTC2022-Spring)*, pp. 1–7, Jun. 2022.

[6] **Pengfei Lin**, Ehsan Javanmardi, Ye Tao, Vishal Chauhan, Jin Nakazato, and Manabu Tsukada, "Time-to-Collision-Aware Lane-Change Strategy Based on Potential Field and Cubic Polynomial for Autonomous Vehicles," in *Proceedings of the 2023 IEEE Intelligent Vehicles Symposium (IV)*, pp. 1-6, Jul. 2023.

[7] **Pengfei Lin**, Ehsan Javanmardi, Jin Nakazato, and Manabu Tsukada, "Occlusion-Aware Path Planning for Collision Avoidance: Leveraging Potential Field Method with Responsibility-Sensitive Safety," Accepted in *Proceedings of the 2023 IEEE International Conference on Intelligent Transportation Systems (ITSC)*, Sep. 2023.

[8] **Pengfei Lin**, Ehsan Javanmardi, Jin Nakazato, and Manabu Tsukada, "Potential Field-Based Path Planning with Interactive Speed Optimization for Autonomous Vehicles," in *Proceedings of the 2023 49th Annual Conference of the IEEE Industrial Electronics Society (IECON)*, pp. 1-6, Oct. 2023.

Publications as Non-first Author

International Journal

[1] Ye Tao, Ehsan Javanmardi, **Pengfei Lin**, Yuze Jiang, Jin Nakazato, Manabu Tsukada, and Hiroshi Esaki, "Zero-Knowledge Proof of Traffic: A Deterministic and Privacy-Preserving Cross Verification Scheme for Cooperative Perception Data," Under Review in *IEEE Access*.

[2] Vishal Chauhan, Chia-Ming Chang, Ehsan Javanmardi, Jin Nakazato, **Pengfei Lin**, Takeo Igarashi, and Manabu Tsukada, "Fostering Fuzzy Logic in Enhancing Pedestrian Safety: Harnessing Smart Pole Interaction Unit for Autonomous Vehicle-to-Pedestrian Communication and Decision Optimization," *Electronics*, vol. 12, no. 20, pp. 4207, Oct. 2023.

International Conferences

[3] Ye Tao, Yuze Jiang, **Pengfei Lin**, Manabu Tsukada, and Hiroshi Esaki, "zk-PoT: Zero-Knowledge Proof of Traffic for Privacy Enabled Cooperative Perception," in *Proceedings of the 2023 IEEE 20th Consumer Communications & Networking Conference (CCNC)*, pp. 261–268, Jan. 2023.

[4] Vishal Chauhan, Chia-Ming Chang, Ehsan Javanmardi, Jin Nakazato, Koki Toda, **Pengfei Lin**, Takeo Igarashi, and Manabu Tsukada, "Keep Calm and Cross: Smart Pole Interaction Unit for Easing Pedestrian Cognitive Load," in *Proceedings of the 2023 IEEE 9th World Forum on Internet of Things (WF-IoT 2023)*, Oct. 2023.